Volumetric and Planar Electrical Capacitance Tomography

Ye, Zhuoyi

Award date:
2015

Awarding institution:
University of Bath

Volumetric and Planar Electrical Capacitance Tomography

A thesis submitted to University of Bath
For the degree of Doctor of Philosophy
In Faculty of Engineering & Design

Zhuoyi Raymond Ye

Department of Electronic & Electrical Engineering

University of Bath

October 2014

COPYRIGHT

_____

Zhuoyi Raymond Ye

Acknowledgements

First of all, I would like to express my heartfelt gratitude to my parents, Mr Xiangyuan Ye and Mrs Yuxia Chen and all my family members for their never-ending support to my work for such a long time.

Secondly, I would like to thank my supervisor Dr. Manuchehr Soleimani sincerely, for all his time, help, dedication and encouragement. It would not be possible to accomplish the work without his selfless supervising. Furthermore, I wish to thank my Co-supervisor Prof. Chris Bowen for all his help to my PhD study.

I would also give my sincerely grateful appreciation to all my colleagues Chuanli Yang, Dr. HY. Wei, Dr. Lu Ma and friends, Dr. Junhong Yang, Dr. Situ Luo from National University of Defence Technology, China, Dr. Yaoyuan Xu from Tianjin University, China, and Dr. Jiangtao Sun from University of Manchester for their kind helps.

Abstract

Electrical capacitance tomography (ECT) is a low cost and fast imaging technique able to obtain cross sectional images of dielectric permittivity distribution. ECT has been successfully used in industrial process tomography mainly for 2D imaging. One of the key challenges in 3D ECT imaging is a large scale forward problem arising with a large number of elements in the meshed ECT sensor model. Notably a complete sensor model will provide the most appropriate solution to the forward problem. A complete sensor model requires modelling a shielded area behind electrodes, which leads to increase in density of the finite element mesh. In this thesis, an approximation error model (AEM) has been applied to the ECT modelling for the first time. In addition to 3D AEM modelling and to further evaluate the effectiveness of the proposed AEM algorithm, it was implemented to compensate for uncertainty in electrode size and mesh density in 2D ECT. The results achieved using AEM are promising. In terms of application area, this thesis focuses on fundamental development for possible use of ECT in non-destructive evaluation (NDE) application. In more traditional industrial process application the object is surrounded by a number of electrodes on its boundary. In NDE applications a planar array ECT and volumetric imaging is needed. This thesis presents a 3D planar array ECT sensor using a 3D reconstruction algorithm. The results are validated with a number of experimental tests. 3D planar array ECT imaging was further extended to image both dielectric and metallic samples. To quantify the limitations of planar array ECT, a 3D ECT sensor and 3D ECT software have been implemented and used to evaluate the performance of the 3D ECT imaging with missing sides, with planar array ECT being the most extreme case of missing sides. The underlying inverse problem was analysed using singular value decomposition of the sensitivity matrix for the first time. This thesis introduces the use of a resolution matrix to analyse the performance of a 3D ECT reconstruction algorithm. These analysis methods, which enabled an in depth analysis of imaging performance with missing sides, are able to quantify the performance of planar array ECT.

Table of Contents

List of Figures

List of Symbols

u	Electrical potential
E	Electrical field
Q	Electrical charge
ε	Dielectric permittivity
C	Capacitance
N	Number of electrodes
M	Number of measurement
J	Jacobian Matrix
R	Regularisation identity matrix
α	Regularisation parameter
β	Relaxation factor in Landweber algorithm
P	Matrix rank
d	Diagonal value of the matrix
λ	Normalised capacitance
Δ	Delta - Change
σ	Singular value of a matrix
∇	Differential operator
U,V	Unitary matrix (used in SVD method)
y	Array of boundary measurements
n	Number of pixels in reconstructed image
x	Reconstruction inclusion
Γ	General error in ECT
Ψ	Discretization error
h	Size of element in finite element method
e	Noise error
RES	Resolution
R_m	Resolution matrix
A	Jacobian matrix (used in SVD form)
D	Pre-condition in Landweber method

CHAPTER 1 Introduction to NDE Methods

This thesis studies the fundamental development that could lead to a potential non-destructive evaluation (NDE) application of capacitive measurement. This chapter aims to provide a general overview of states of existing NDE methods. The thesis will focus on the electrical capacitance tomography (ECT). In this chapter, several existing NDE methods are introduced.

ECT has been widely used in industry since the late 1980s and early 1990s due to its low cost, fast response and some other specific requirements such as contactless test and constraint of testing time. ECT can be used to sense an objective by detecting the electrical field change inside the measurement range after applying a constant electrical potential between each combination of two electrodes. By applying an electrical potential to excitation electrodes, an electrostatic field is produced inside an ECT sensor to detect the permittivity changes of an object. It is proposed as a method for industrial process monitoring [1, 2, 3, 50]. However, it has not currently been used widely. There are many potential applications of ECT, such as real-time monitoring of a flow of liquids within pipes, separation of fluids, and potentially non-destructive testing (NDT) of dielectric materials, and even non-destructive crack detection in dielectric materials. Generally speaking, the principle of ECT can be used to investigate and

observe any process where both materials have low electric conductivity and have different permittivity.

To solve the ECT inverse problems, there are currently several commonly used algorithms. Linear Back Projection (LBP) [1, 2, 7] is a basic and most commonly used image reconstruction algorithm and will be introduced in the following chapter. LBP is able to achieve a very fast response, but it does not provide a very accurate result [4]. Landweber iteration method [1, 2, 13, 16] is a more advanced reconstruction algorithm but much more complicated than LBP. While learning different reconstruction methods, some solutions achieved by solving ECT ill-posed problem have been found. One involves the commonly used regularisation method named Tikhonov regularisation [1, 2, 5, 8]. This regularisation method minimizes the negative effect caused by those estimated components which have small singular values by adding a parameter term (depending to the value of regularisation parameter). Together with the regularisation technique, a powerful mathematical technique dealing with singular sets of equations called singular value decomposition (SVD) is used to analyse the ill-posedness of the inverse problem [3, 7, 8, 35].

1.1 NDE for non-conductive material

According to information provided by UK Research Centre in Non-destructive Evaluation (RCNE), NDE has become a crucial tool in industry due to the increasingly challenging requirements to achieve greater integrity and safety performance. NDE is the definition for inspection techniques, which are non-invasive and non-intrusive [1].

Due to this advantage, there is continuously focus in using NDE, and there will be considerable improvement of manufacturing processes through automation, improving efficiency and reducing the number of faulty products out of the production line. There are many conventional types of non-destructive inspection methods that are being currently widely used in industry for dielectric materials. Amongst the most common NDE methods, are ultrasound, X-rays, dye penetrant and eddy current inspection.

Ultrasound technique is one of the most widely used techniques in civil, aerospace and medical applications due to its high accuracy and other characteristics. However, this technique has proven to be slow. To process ultrasonic testing, contacting medium (i.e. water, gel) is always required [109]. Therefore, ultrasound technique sometimes is not considered as non-destructive. Radiography is another common used technique for difficult materials. However, the use of radiography not only requires proper screening to protect the users but also is comparatively expensive. [145] Dye penetrant technique can only work with surface damage. In following sections, several common used NDE methods are introduced.

1.1.1 *Liquid dye penetrant inspection*

Liquid dye penetrant inspection is a widely applied and low-cost inspection method used to locate surface-breaking defects in all non-porous materials (metals, plastics, or ceramics). The penetrant may be applied to all non-ferrous materials and ferrous materials, although for ferrous components magnetic-particle inspection is often used instead for its subsurface detection capability. Liquid Dye Penetrant Inspection method is used to detect casting, forging and welding surface defects such as hairline cracks,

surface porosity, leaks in new products, and fatigue cracks on in-service components. As shown in Figure 1-1, after pre-cleaning the test object with cloth and dampening with solvent (a), penetrant is able to be applied on the surface by spraying or brushing (b). After proper dwell time, excess penetrant is removed (c). By applying the developer on the surface of test object (d), the surface damage can be decorated (e).

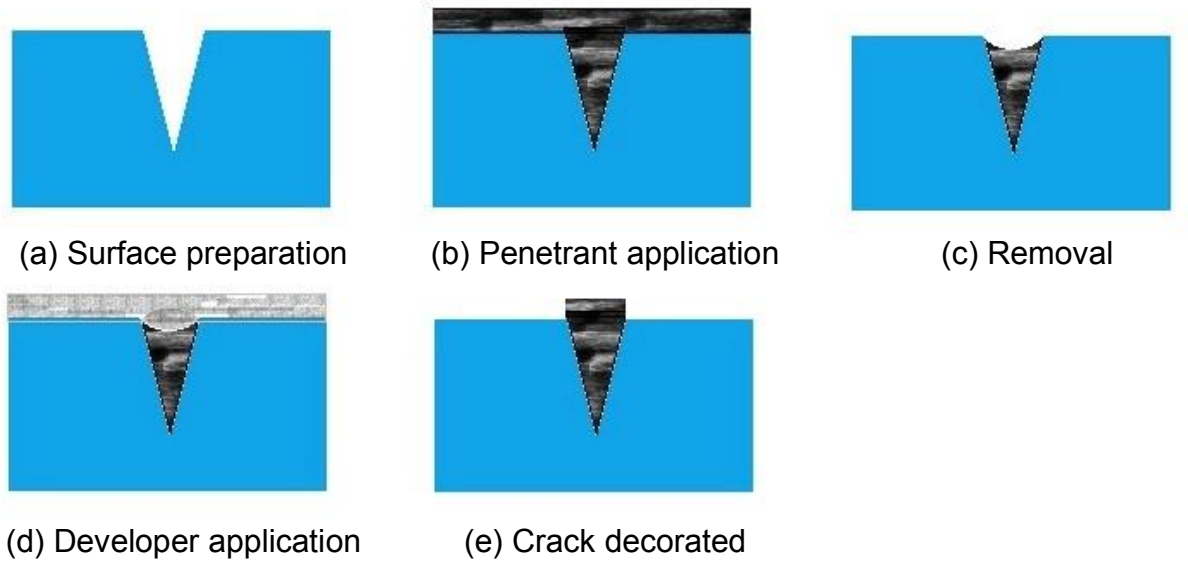

Figure 1-1: Procedures of NDE-liquid dye penetrant

1.1.2 *Radiography*

The human body is difficult to model as a complete transfer function. Elements of the body, however, such as bones or molecules, have a known response to certain radiographic inputs, such as x-rays or magnetic resonance [75,106]. Coupled with the controlled introduction of a known element, such as digested barium, radiography can be used to image parts or functions of the body by measuring and interpreting the response to the radiographic input (as shown in Figure 1-2). The principle of radiography as a NDE method, is by using change of energy (energy lost) while x-ray travels through both the perfect part and damaged part of the material to image the test

object. In this manner, many bone fractures and diseases can be detected and localised in preparation for treatment. For these reasons, this method has also been used to examine the interior of mechanical systems in manufacturing as NDT techniques, as well [106]. As shown in Figure 1-2, x-rays are emitted to the testing object to image the internal condition.

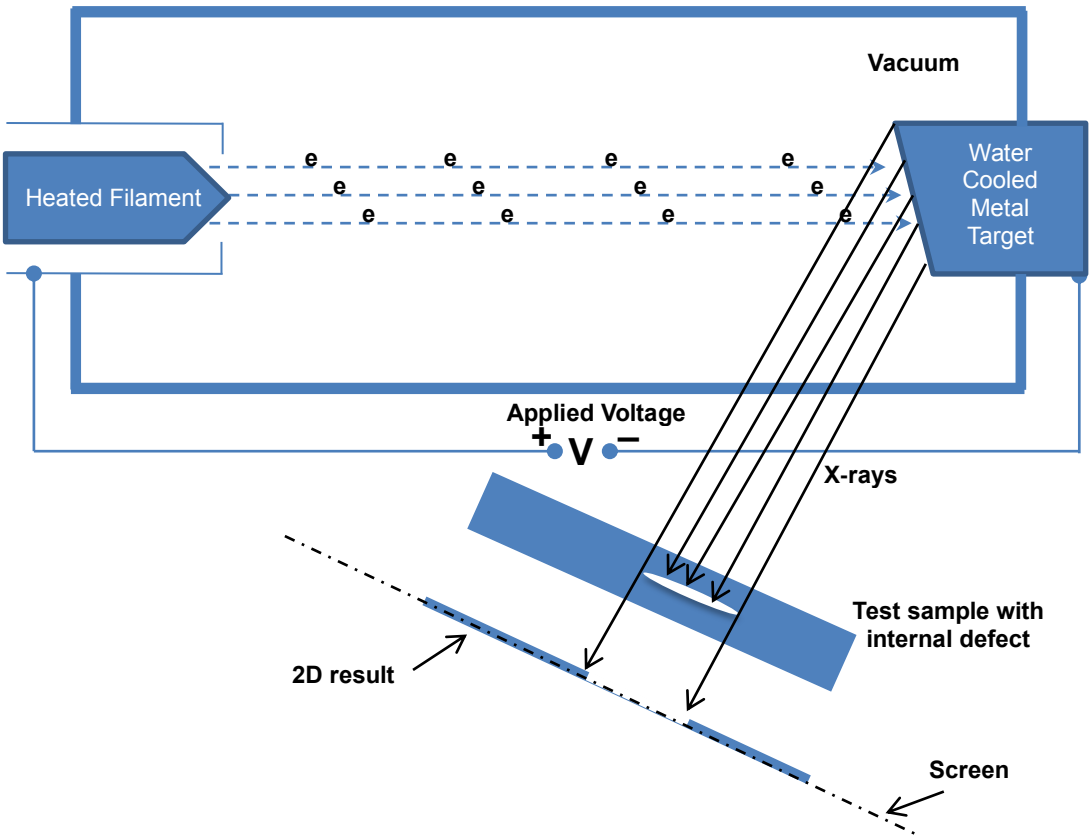

Figure 1-2: X-ray inspection process

X-ray is the electromagnetic radiation with wavelengths in the range around 10 nm while the visible light has the wavelength from 0.4 to 0.8 μm. The energy of photon can be expressed as $E = hv$, where h is the Plank's constant and v is the frequency. Meanwhile the maximum possible energy of X-ray can be expressed as $E = eV$, where

e is the electron charge and V is the applied voltage. The electron energy is transferred into X-ray energy in the collision process.

By imaging the X-ray absorption energy through the test sample, a NDT process can be achieved. X-ray absorption depends on the sample thickness, properties of material (such as density) [107,108], and X-ray photon energy. A radiography method is sensitive to defects. The defects are determined from the difference in amount of the energy absorption that X-ray travel through the sample and the defects. This technique works with both non-conductive and conductive materials.

Recent work has looked into 3D examination of impact damage in composite material by using a radiography method [107, 126].

1.1.3 *Thermography*

Strictly, thermography is not an NDE technique as it requires the structure to be heated to display differences in the thermal properties. A thermal camera is used to detect the surface temperature of the test sample [41]. By using the difference of thermal conductivity between air (always exists with defects) and the testing sample, to image the internal condition, thermography has become a new type NDT method. Thermography has not been used widely yet. In this NDE process, the object in question is heated up and exposed to the air while using a thermal cameral to image the sample as shown in Figure 1-3. Because air has very small thermal conductivity, the cooling rate among the perfect part and defected part of the sample is significantly different. Due to the different thermal conductivity, a thermal camera is able to capture the hot spot and locate the defect. [99-101, 149]

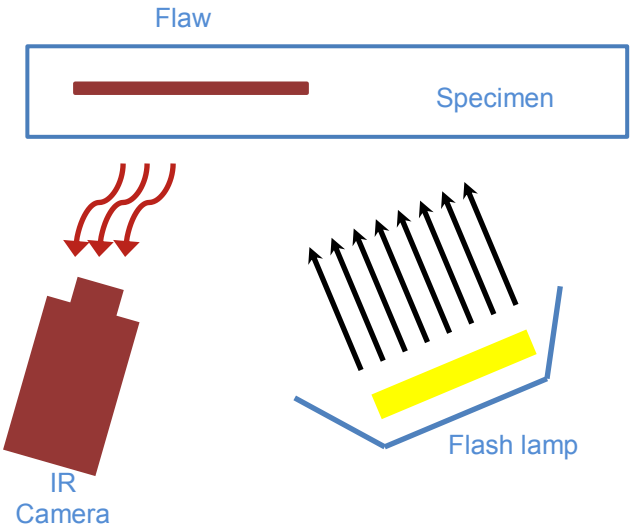

Figure 1-3: Thermography for NDT applications

1.1.4 *Ultrasonic inspection*

Ultrasonic testing is the most widely used non-destructive inspection method for the examination of composites and other material [96, 97]. With microscopically homogenous materials, it is commonly used in the frequency range 20 kHz to 20 MHz. However, with composite materials, the testing range is significantly reduced because of the increased attenuation. The operating frequency limit is usually 5 MHZ or less in this case [104]. A traditional ultrasonic sensor includes piezoelectric transducer, mechanical damping and focus lens as shown in Figure 1-4.

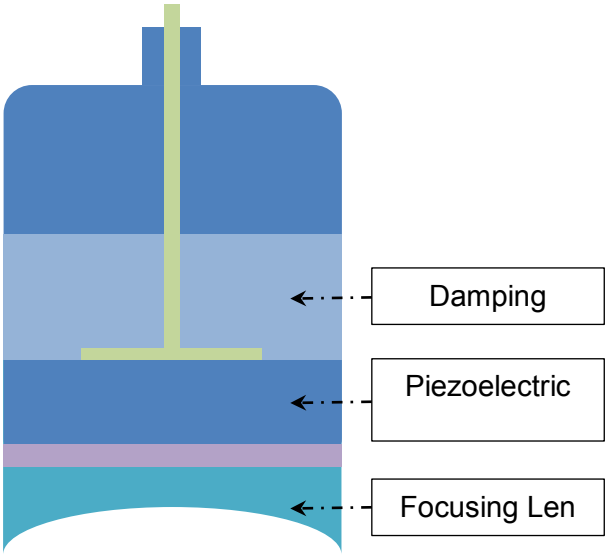

Figure 1-4: Ultrasonic sensor

Being one of the most well-known NDT applications, ultrasound imaging employs high frequency acoustic waves to probe the interior of a sample. As the acoustic wave penetrates through the sample it is attenuated and reflected by any change in the density of the material. The reflected signal at the transceiver can be used to form an image. The development of the ultrasonic technique for plastic pipes spans across the use of pulse echo. A common application is the thickness measurement such as to measure pipework corrosion [106].

A pulse of ultrasonic energy, typically a few microseconds, is transmitted into the specimen in a direction normal to the surface. The pulse is reflected by perfect (undamaged) matrix-reinforcement boundaries and also from the boundaries associated with flaws as shown in Figure 1-5.

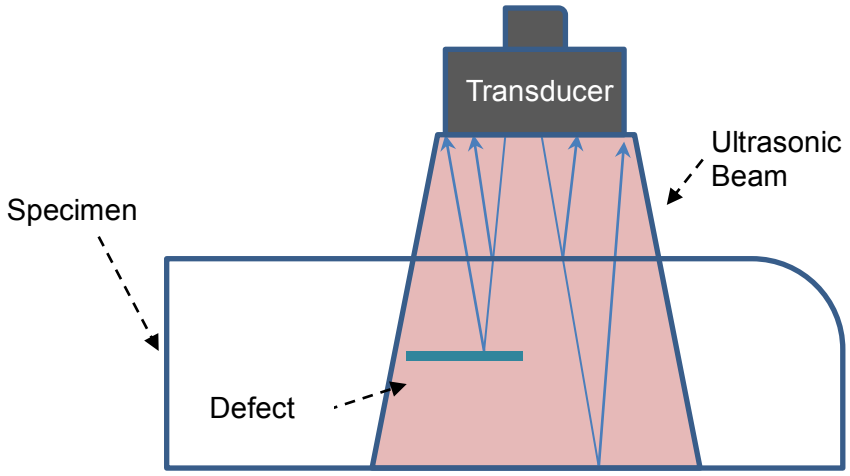

Figure 1-5: Immersion pulse-echo test with submerged specimen

Those signals, which travel back towards the probe, are detected and the position and size of a flaw is determined from the total pulse travel time and detected amplitude respectively. This is called A-scan display and it consists of a series of peaks, the position of which along the horizontal axis can be calibrated in terms of the depth in the composite. The amplitude of each echo will give some indication of the size and nature of the reflector, which might be a flaw or a specimen boundary.

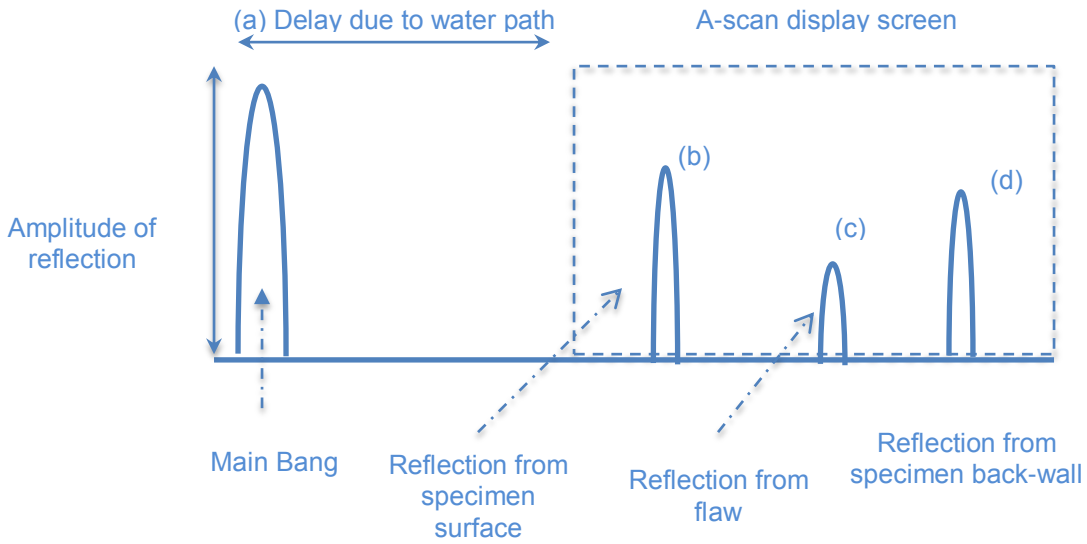

Figure 1-6: A-scan display for a typical pulse-echo immersion test

In this testing method, there are four types of scan, named A-scan, B-scan, C-scan, and D-scan. Figure 1-6 demonstrates a typical A-scan display from a pulse-echo immersion test. In this figure, the echoes with different features within the composite do not merge (they are well resolved) because the pulse duration is short to prevent it from interacting with others at the same time. The first peak (a) is due to the electrical pulse used to excite the transducer (as known as the 'main bang') and is a convenient reference for the following peaks. These are the front surface of the component (b), a flaw (c) and the rear surface of the component also known as the back-wall (d).

In ultrasonic testing, B-scan displays a 2D 'slice' through the specimen is produced by scanning the probe along the surface and capturing an A-scan at each point along the scanning direction. Therefore, B-scan is always considered as a large number of A-scans. The resulting echoes are used to achieve the internal condition of a cross section inside the component. C-scan is the most relevant scan method of ultrasonic scanning. As shown in Figure 1-7, in C-scan, a large number of A-scans are located at each point on scan while defect echoes are displayed as an XY imaging of the part. C-scan is a very slow process as it scans a very small area but the component could possibly be very big. D-scan is also a slice through the specimen taken at a fixed scanning point in each of a set of parallel B-scans as shown in Figure 1-7.

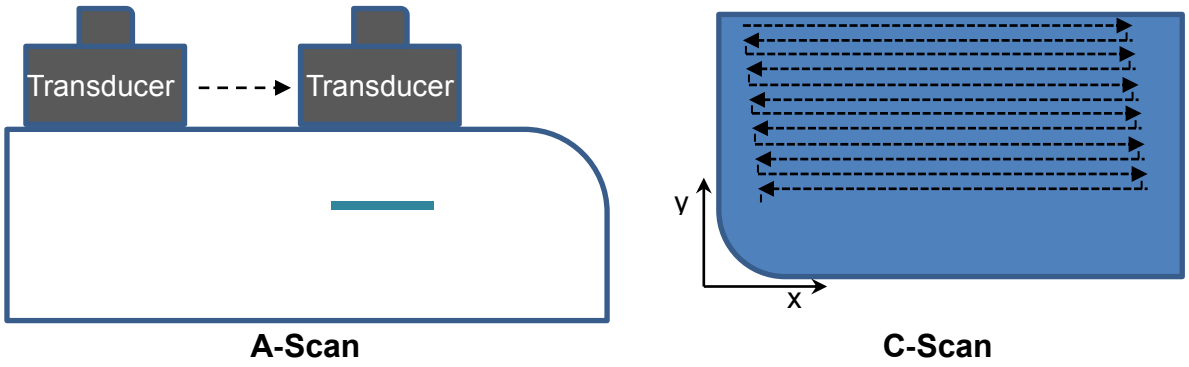

Figure 1-7: Ultrasonic scanning

To summarise, ultrasonic inspection is able to detect both the location and the size of internal defects accurately [97,104,106]. Ultrasonic scanning does not require the full access to the component, but only one side is needed. There is no radiation hazard in ultrasonic testing, and the most important factor is that planar defects are able to be detected, irrespective of their orientation.

Ultrasound is non-invasive. However for some applications, it requires a medium gel to be applied between the sensor and the object, which makes it intrusive [97,104]. Furthermore, ultrasonic testing is terribly slow. In certain materials, like austenitic steel, the large grain size found in welds can cause attenuation and this may mask defects. Furthermore, spurious indications, and the misreading of signals, can potentially result in unnecessary cost to repair.

1.2 Capacitive imaging method for NDE

To find a method of non-destructive dielectric material inspection, there has been a new approach developed at University of Warwick in 2006 [14], which is capable of imaging a wide range of materials and structures, ranging from insulators to metallic conductors. The approach, which has the potential to image the internal structure of different materials, known as capacitive imaging, uses electrode arrays to produce an AC electric field distribution within the material. By scanning the field over the material causes a change in the field distribution, and hence changes in output voltage. Capacitive coupling allows the technique to work on a wide variety of material properties, without requirement of contact and transmission medium.

A pair of capacitive electrodes was used to generate an electric field distribution within the material. The test sample was placed between the electrodes as shown in Figure 1-8. This experiment took a set of two metal plates as electrodes, which are placed above the surface of the test sample to be scanned by a certain distance and parallel to the surface of the sample. By applying excitation voltage to electrodes as the input, a charge signal is then able to be captured as the output as shown in Figure 1-8. This technique has been extended to arrays for emergency imaging scanning because this technique is fast and contactless.

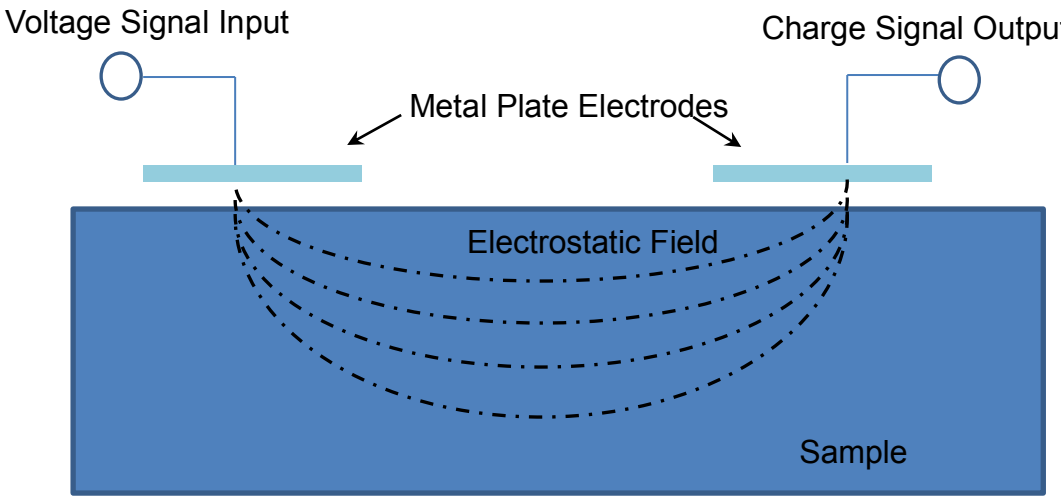

Figure 1-8: Experiment structure of capacitivie imaging

In this case, the excitation voltage is in sinusoidal form with a fixed frequency. An alternative electrostatic field is established, with field lines passing through the object, whereby charge is induced on the surface of the second electrode. This coupled charge can be detected via a number of standard techniques such as charge amplifiers, processed and outputted as a DC voltage level.

Research group from University of Warwick has carried out a series of test using this technique on concrete and some other dielectric material in 2D capacitive imaging and the results were promising as shown in Figure 1-9 [14].

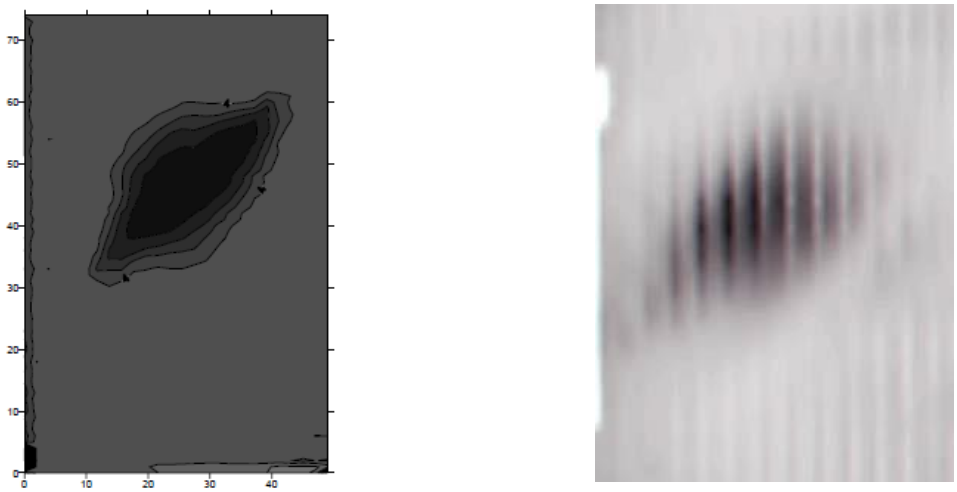

(a) Air-coupled ultrasound in through-transmission (b) Single-sided capacitive imaging

Figure 1-9:Results achieved using capacitive imaging by University of Warwick [14]

In 2011, a similar approach was developed at University of Warwick and Thapaer University in India described the application of capacitive sensing to the inspection of defects in fibre reinforced polymer (FRP) composites and reinforced concrete structures by carrying out series of 2D experiments [10]. In their work, a 2D finite element modelling method was proposed to detect the air and water voids in FRP wrapped concrete structure, by capturing the change in electric field images due to presence of certain defect. [10]

Their proof-of-concept results indicate that the capacitive sensing technique could be used to detect cracks on the surface of FRP composites, as well as sub-surface air voids and water voids in RC structures.

1.3 Aims and Objectives

The aim of this thesis is to evaluate the NDE application of ECT. There are many techniques that lend themselves to the use of an NDE application. Each of them has its own advantages and disadvantages. Among these, ECT has good potential (i.e. contactless inspection, fast response) but is very challenging due to the performance limitation to be used towards NDE applications.

In reality, the test object cannot be scanned in full access (due to the size of the object). Hence limited-access-ECT such as planar array ECT has become necessary. This thesis is primarily focusing on in-depth analysis of limited-access-ECT and planar array ECT for potential NDE application due to its advantage of geometrical flexibility. Therefore, one of the main objectives in this thesis is to extend the image software for different geometries.

The planar array ECT is suitable for NDE application, hence to evaluate the feasibility of this technique to provide volumetric sub-surface image, is the most important objective of this thesis. The planar array sensor is potentially able to provide more depth compared to the traditional capacitive imaging method for NDE. To understand the challenges with planar array ECT in NDE application, the thesis aims to evaluate the effect of missing data. This aim is done using a full 3D ECT sensor.

To evaluate the NDE application of ECT, the following tasks were carried out:

- ECT forward modelling for various geometries in 2D and 3D;

- Approximation error modelling for forward and inverse ECT problem;
- Planar array ECT in 3D;
- Evaluation of planar array technique
- Relationship between image quality and amount of missing information (Full 3D technique).

To tackle these tasks, the fundamental skills and knowledge of the whole process of ECT reconstruction using various algorithms were gained, and several different types of ECT sensors have been built (both in 2D and 3D), which are used for evaluations.

1.4 Thesis Structure

This thesis is about the evaluation of ECT. It is divided into several chapters to lead readers to a clear understanding of the technique and improvements that have been made to this technique. In the very beginning, various commonly used algorithms for ECT and different ECT sensors are demonstrated. Sections include various geometries of sensor design, and forward and inverse problems of ECT. In the linear reconstruction sections, the basic and commonly used method named linear back projection (LBP) is mentioned so as several other different algorithms. An iterative reconstruction algorithm (Landweber iteration method) is described, which is able to provide more accurate results. Both algorithms have been used in 2D and 3D image reconstruction. Non-linear reconstruction algorithm is found to be able to improve the results. However, this method is challenging for 3D ECT. Following this, the approximate error method is introduced in Chapter 3. This method is able to provide a

good result, which normally requires a very dense model, by using a coarse meshed model.

Planar array ECT is one of the extreme cases in a limited access ECT technique. This type of ECT test has been performed and analysed in 3D (Chapter 4), while full 3D ECT and imaging quality varying with different amounts of missing data are analysed in Chapter 5 to provide a clear understanding of the 3D planar array ECT technique compared to a traditional ECT system. The validation of image quality and amount of missing data was analysed by using a full 3D ECT system in this chapter.

Finally, conclusions and future work will be provided at the end of this thesis.

CHAPTER 2 Electrical Capacitance Tomography

This chapter aims to provide a brief of ECT system and methods. The image reconstruction of ECT can be divided into two parts, the forward problem and the inverse problem. The inverse problem of ECT is always ill-posed. Hence, different algorithms have been developed to solve the ECT inverse problem. To evaluate the performance of these well-known algorithms, experiments are carried out, but only some meshed models for forward modelling are shown in this chapter.

2.1 Electrical capacitance tomography system

The hardware of a traditional ECT system includes three parts as shown in Figure 2-1, namely a capacitance sensor, a capacitance measurement unit and a computer [2].

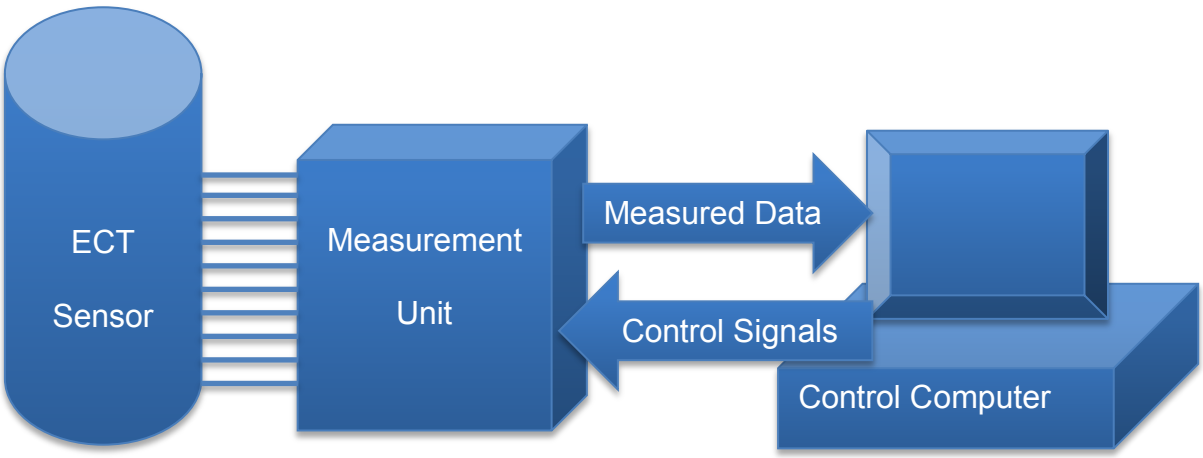

Figure 2-1: A schematic drawing of ECT system

2.1.1 *Capacitance sensor design*

An ECT sensor is comprised of an array of conducting plate electrodes (copper tape is used in the ECT sensors for electrodes) as shown in Figure 2-2. The outer grounded shield is not shown in this Figure so that the electrodes can been seen.

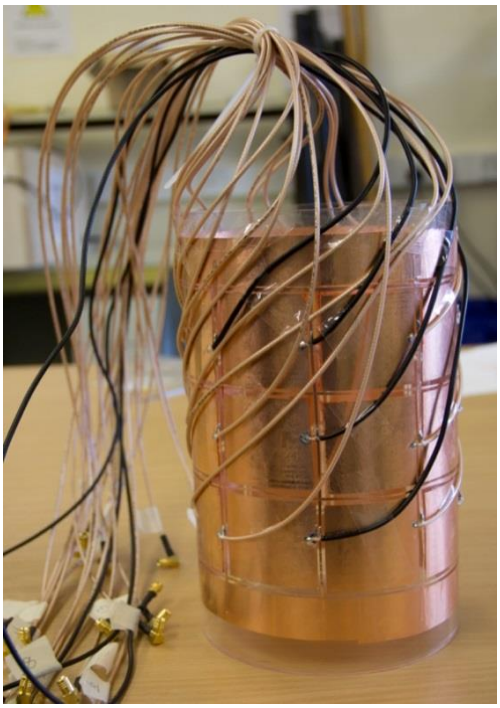

Figure 2-2: 3D circular ECT sensor

There are several parameters of the sensor design that could affect the measurement significantly and they should be considered carefully to achieve the best performance for the sensor [2]. There are parameters which are able to influence the image quality such as number of electrodes. It is commonly known that by using more electrodes, more measurements are able to be achieved potentially. But this doesn't necessarily improve the quality of image reconstruction. Because, with a constant sensor area, using more electrodes can result in decreasing in electrode surface area. Therefore,

signals captured on electrodes could be small in this case. There are other parameters to be considered include:

A. The gap between the overall screen and the electrodes;

B. The permittivity of the insulating pipe;

C. The thickness of the insulating pipe;

D. The size of the grounded layer of the electrodes.

2.1.2 *Capacitance measurement unit*

The capacitance measurement unit plays a very important role in measuring and conditioning the signals that are achieved from the capacitance sensor. The measuring unit has four parts, which are shown in Figure 2-3.

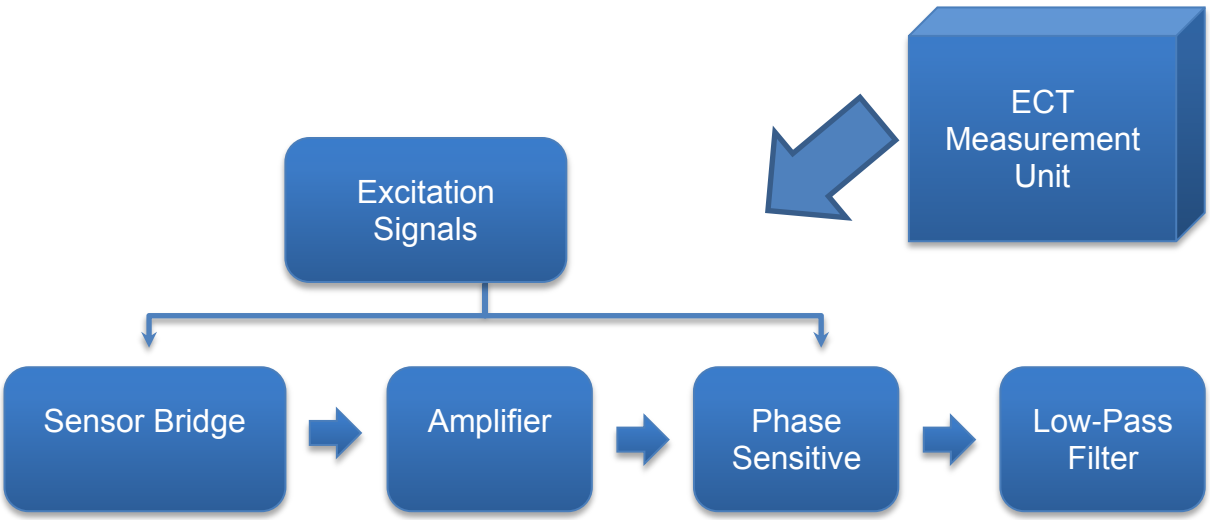

Figure 2-3: A schematic drawing of a capacitance measuring unit

The capacitance measuring bridge is an alternating current AC bridge, which is used for measuring the inter-electrode capacitances of the sensor. Shielded SMB cables are

used to connect the sensor and measurement unit in this thesis as shown in Figure 2-2 and the measuring unit is provided by Process Tomography Ltd (PTL). The measuring unit, which is used in the laboratory, is able to amplify the signals received that are normally weak and corrupted with noise. By using the measuring unit provided, normalised capacitance data can be obtained.

2.1.3 *Control computer*

Since computers can only process digital signals, an analogue-to-digital converter (ADC) is required before the computer can process the capacitance data. The converter is usually available as a plug and play card, which can be fixed into a computer. Hence, the digitisation of an analogue signal can be handled by a computer [1, 3, 7, 35]. The main function of the computer is to process the collected data and implement image reconstruction. In this thesis, MatLab is used for image reconstruction and the computer acts as a display unit.

2.2 ECT forward problem

The ECT image reconstruction process includes two steps, forward problems and inverse problems [1, 3, 6]. The forward problems will be explained in detail in the following parts of this chapter, while the inverse problems will be dealt with in the following sections.

For ECT, the forward problem is a simulative process to calculate the electric potential and the capacitance matrix by providing the geometry of an ECT sensor, the potential applied on the exciting electrodes, and the geometry of the object inside the sensor. In a typical ECT process, a fixed voltage is applied to each of the electrodes in turn, while all the other electrodes are grounded. The total potential is measured on each of the remaining electrodes. For this reason the number of measurements has a relationship with the number of electrodes, which will be explained later.

Several assumptions are worth pointing out:

1. Negligible internal charges and wave propagation effects;

2. Assuming the electrostatic approximation $\nabla \times E = 0$, for an electric potential u

$$E = -\nabla u \tag{2.1}$$

then the mathematical model for an ECT forward problem can be written as:

$$\nabla \cdot (\varepsilon \nabla u) = 0 \; on \; \Omega \tag{2.2}$$

where ε is the dielectric permittivity and Ω indicates the region inside the cylindrical screen, excluding the electrodes and radial screens.

The electric potential is fixed on each electrode and the boundary conditions can be defined as:

$$u = v_k \; on \; E_k \tag{2.3}$$

where E_k indicates the k[th] electrode, and v_k is the voltage, that is applied on the recitative electrode and is zero on all other sensing electrodes. Therefore, the electrical charge on the k[th] electrode can be expressed as below:

$$Q_k = \int_{E_k} \varepsilon \frac{\partial u}{\partial n} dS \tag{2.4}$$

where n is the inward normal on the k[th] electrode. FEM is used solve this problem. By using Galerkin's approximation, [3] the boundary value problem reduces to a linear system of equations.

$$K(\varepsilon)U = Q \tag{2.5}$$

In this equation, K indicates the discrete representation of $\nabla \cdot \varepsilon \nabla$, Q is the boundary condition term and U is the vector of electric potential solution.

Assuming the thickness of electrodes is negligible, then the total charge on the k[th] electrode Q_k is the sum of charges between internal Q_k^{int} and external Q_k^{ext}

$$Q_k = Q_k^{int} + Q_k^{ext} \tag{2.6}$$

$$Q_k^{int} = \int_{E_k} \varepsilon \frac{\partial u^{int}}{\partial n} dS \tag{2.7}$$

$$Q_k^{ext} = \int_{E_k} \varepsilon \frac{\partial u^{ext}}{\partial n} dS \tag{2.8}$$

where u^{int} and u^{ext} are the electric potentials on the inner and outer surfaces of the electrode respectively.

It can be seen that interference would occur between the interior and exterior of the electrode through the gap between Q_k^{int} and Q_k^{ext} , which are both affected by the change of permittivity [3]. Therefore, with a same number of electrodes, using a sensor design which has very small gaps between electrodes to maximise the surface area of electrodes, can improve the quality of image reconstruction [3].

In ECT, the capacitance data are normalised after calibration. The normalised capacitance is :

$$\lambda = \frac{C_{meas} - C_{air}}{C_{high} - C_{air}} \tag{2.9}$$

where C_{air} is the capacitance measurement for free space, C_{meas} is the absolute capacitance measurement and C_{high} is the capacitance measurement while the sensor is filled with a high permittivity object.

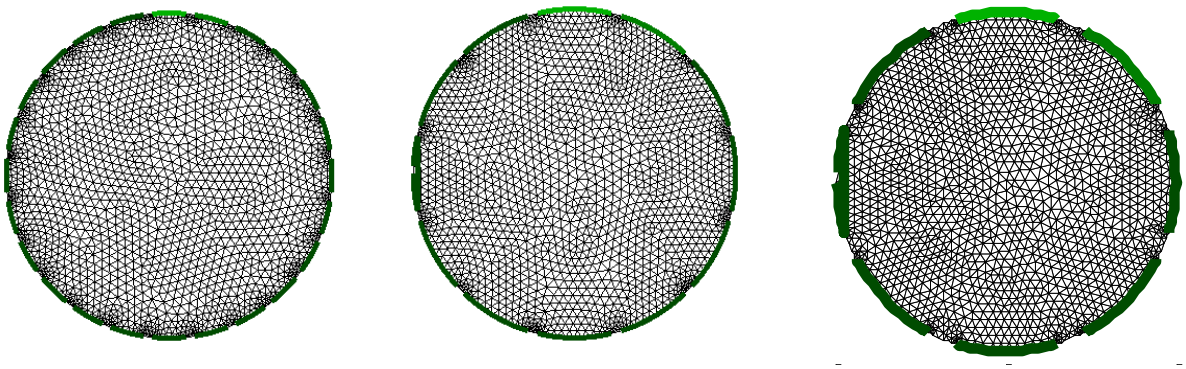

(a) **(b)** **(c)**

Figure 2-4: Mesh models of 2D ECT systems; (a): Model with 24 electrodes; (b): Model with 12 electrodes; (c): Model with 8 electrodes

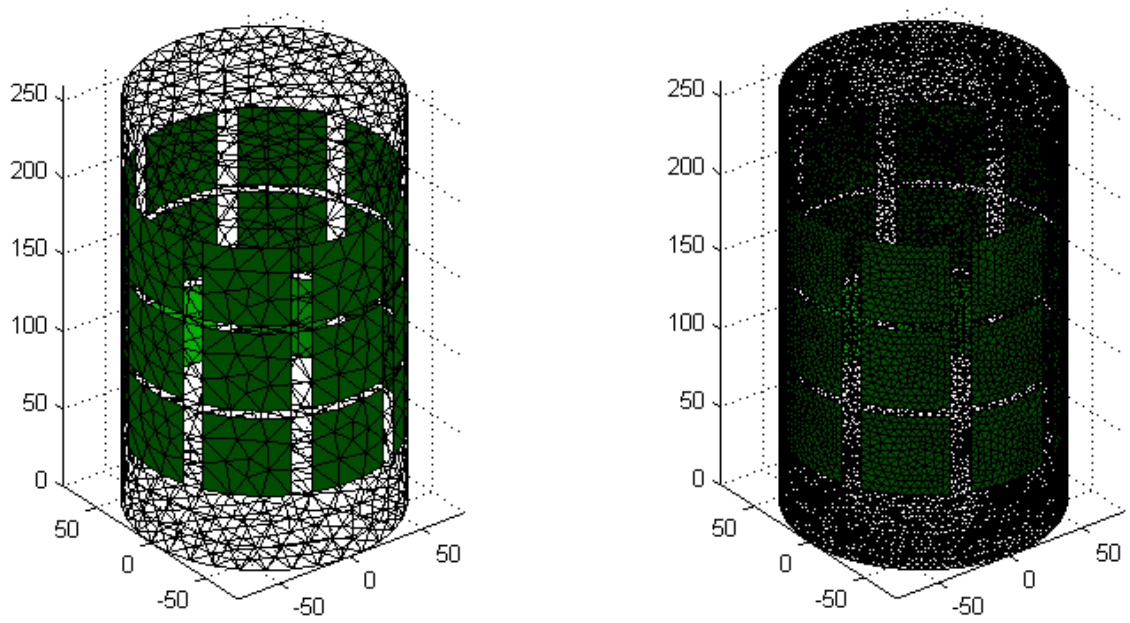

Figure 2-5: Mesh model of 3D ECT; Left: Coarse meshed model with 24 electrodes; Right: Dense meshed model with 24 electrodes;

Figure 2-4 and Figure 2-5 demonstrate the meshed models for 2D and 3D sensors respectively. Among the 2D meshed models in Figure 2-4, there are 8 electrodes, 12 electrodes and 24 electrodes respectively. Among the 3D models in Figure 2-5, two computer models are generated based on an ECT sensor with different mesh density.

A traditional circular 2D ECT sensor with 12 electrodes has been built. One of the planes in this 3D sensor was used as a 2D sensor. Several meshed models were programmed in different mesh densities, as shown in Figure 2-6, to compare how mesh density influences the reconstructed image.

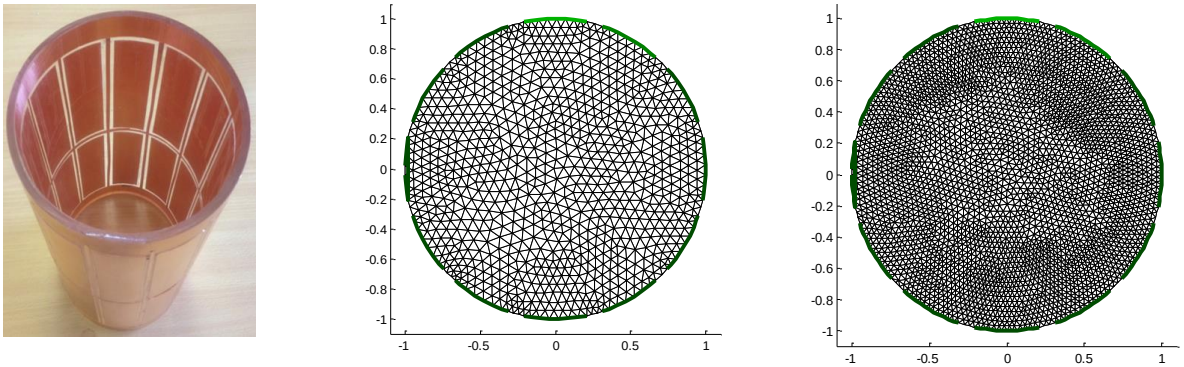

Figure 2-6 Mesh model of 12 electrodes 2D ECT system;(a): Real ECT 3D sensor with 12 electrodes; (b): Model with coarse mesh density; (c): Model with dense mesh density;

As shown in Figure 2-6, the first model is meshed into 1730 elements while the second model has 6210 elements. It is commonly known that with a fine meshed model, improvement in image quality could be achieved. However, a greater mesh density can cause longer computational time due to a larger number of elements and a larger number of calculations.

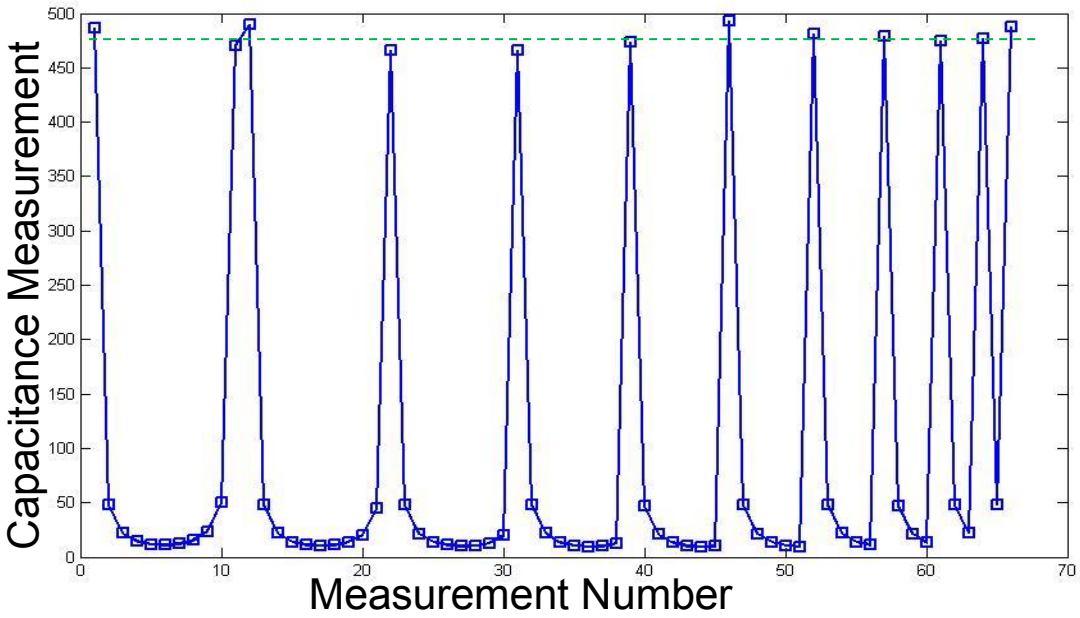

(a) 2D ECT measurement

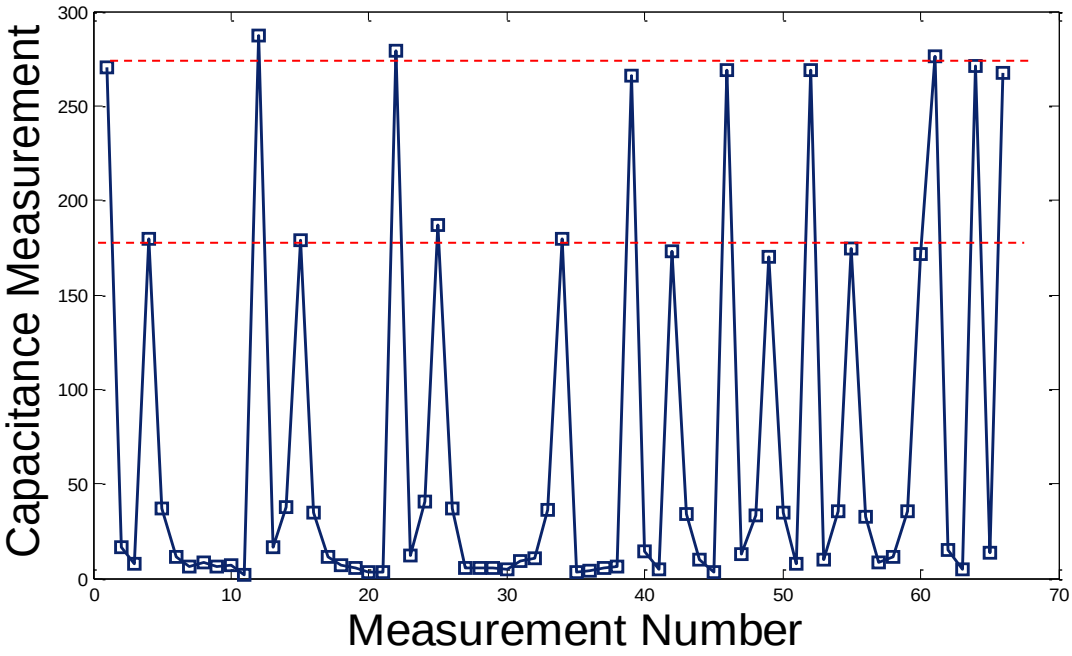

(b) 3D ECT measurement

Figure 2-7: Sample of capacitance measurements (a) 2D ECT measurement (b) 3D ECT measurement

Figure 2-7 shows the measurement data with (a) a 2D ECT sensor and (b) a 3D ECT sensor (b) respectively. The capacitance of each combination of electrodes was measured, the relation between the number of measurements and the number of electrodes is:

$$Numer\ of\ measurement = \frac{N(N-1)}{2} \tag{2.10}$$

where N is the number of electrodes.

With a 12 electrode system, there are 66 measurements captured. With respect to Figure 2-7, graph (a) shows the measurement data for 66 measurements in a 12-electrode-2D system, while graph (b) shows a 2 x 6 electrode 3D system (12 electrodes in total). As can be seen, the capacitive measurement pattern in (b) is formed by two

peak levels (marked in red line) while the single plane 2D system only has one peak level in measurement (marked in green line). In ECT, measurements of the capacitance between each combination of two electrodes are taken in turn. For free-space measurements, as shown in Figure 2-7, neighbouring electrodes provide similar capacitance measurements so are the diagonal electrodes but at different level, when the entire measurement data is plotted with measurement number as shown in this case, the peak levels, as marked in dashed line in Figure 2-7, are formed.

2.2.1 *Rectangular ECT sensor*

A rectangular sensor has also been built, as shown in Figure 2-8. The rectangular ECT sensor (a) was meshed into the computer model (b). Compared to a circular sensor, by using the same number of electrodes of the same size, the rectangular sensor enlarges the sensor area. By applying a simulative voltage on the electrode and running forward problem process, the potential distribution (c), current distribution (d) and filed distribution (e) can be seen in Figure 2-8.

(a) Rectangular sensor

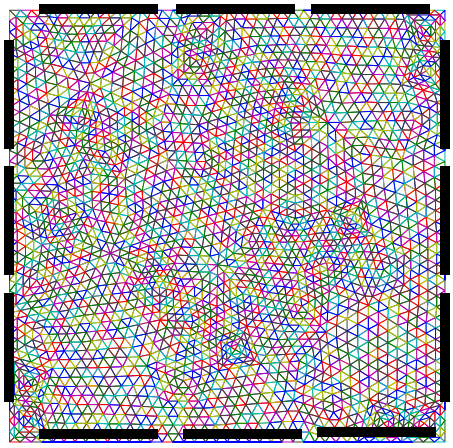

(b) Meshed computer model in MatLab

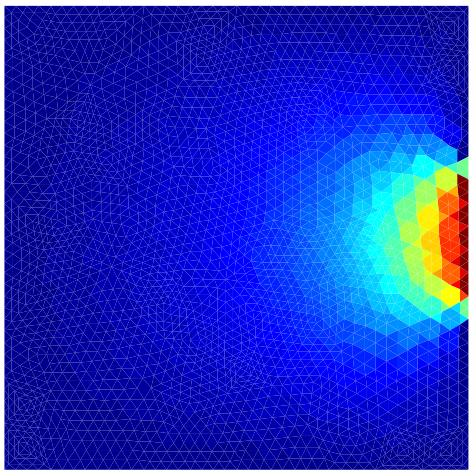

(c) Potential distribution of the rectangular sensor

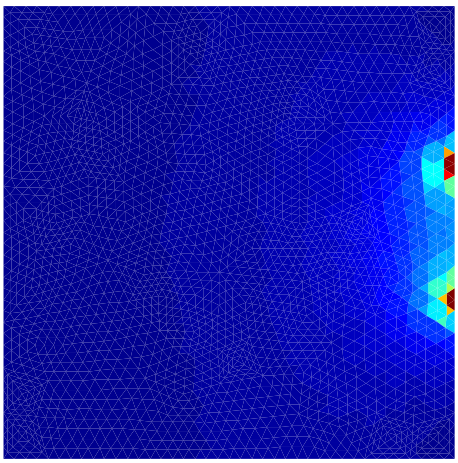

(d) Current distribution of the rectangular sensor

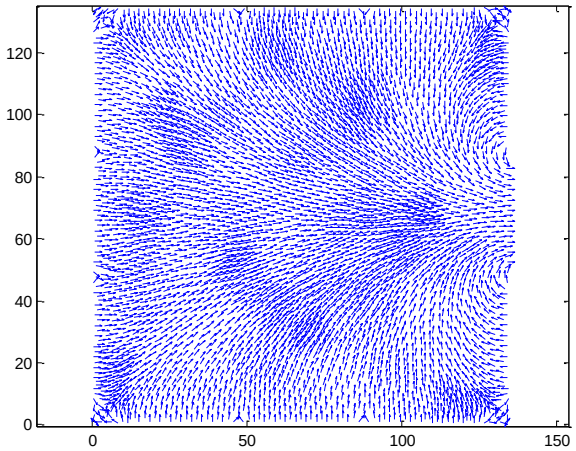

(e) Field distribution of the rectangular sensor

Figure 2-8: Forward results of the rectangular ECT sensor (a) Rectangular sensor,(b) Meshed computer model in MatLab, (c) Potential distribution of the rectangular sensor, (d) Current distribution of the rectangular sensor, (e) Field distribution of the rectangular sensor.

2.2.2 *Jacobian matrix and sensitivity map*

The relationship between capacitance and the permittivity in each pixel (2D) or voxel (3D) is non-linear. A Jacobian matrix is used to linearise this relationship. Each row of the Jacobian matrix represents the sensitivity of one measurement data with respect to all voxels. Each row of the Jacobian matrix (also called the sensitivity map) indicates the relationship between capacitance and the permittivity of each combination of electrodes [1, 7]. The sensitivity map can be calculated using an efficient formulation based on fields calculated from excitation and sensing electrodes [2, 3, 14].

$$\frac{\partial C_{ij}}{\partial \varepsilon} = -\int_{\Omega} \nabla u_i . \nabla u_j dx^3 \qquad (2.11)$$

where u_i and u_j are the potentials over the region Ω when electrodes i and j are excitation electrodes respectively. Examples of sensitivity plots for some combinations of excitation and sensing electrodes are shown in Figure 2-9 and 2-10.

In Section 2.2, the capacitance measurements between different combinations of electrodes in pairs can be defined as a function of the permittivity distribution. Hence:

$$C=F(\varepsilon) \qquad (2.12)$$

where $C = [C_1 \dots C_m \dots C_M]^T$ is the capacitance vector consisting of all capacitances measured for all possible combination of the electrodes and M is the number of measurements.

$F(\varepsilon) = [f_1(\varepsilon) \dots f_m(\varepsilon) \dots f_M(\varepsilon)]^T$, where $\varepsilon = [\varepsilon_1, \dots, \varepsilon_k, \dots, \varepsilon_K]^T$. ε is the vector of permittivity distribution, which includes K pixels of permittivity.

Therefore, the change in capacitance, ΔC, in response to a perturbation of the permittivity distribution can be defined as:

$$\Delta C = J \cdot \Delta\varepsilon + O(\Delta(\varepsilon)^2) = \begin{bmatrix} \frac{\partial f_1(\varepsilon)}{\partial \varepsilon_1} & \frac{\partial f_1(\varepsilon)}{\partial \varepsilon_2} & \cdots & \frac{\partial f_1(\varepsilon)}{\partial \varepsilon_k} & \cdots & \frac{\partial f_1(\varepsilon)}{\partial \varepsilon_K} \\ \vdots & \vdots & \ddots & \vdots & \ddots & \vdots \\ \frac{\partial f_m(\varepsilon)}{\partial \varepsilon_1} & \frac{\partial f_m(\varepsilon)}{\partial \varepsilon_2} & \cdots & \frac{\partial f_m(\varepsilon)}{\partial \varepsilon_k} & \cdots & \frac{\partial f_m(\varepsilon)}{\partial \varepsilon_K} \\ \vdots & \vdots & \ddots & \vdots & \ddots & \vdots \\ \frac{\partial f_M(\varepsilon)}{\partial \varepsilon_1} & \frac{\partial f_M(\varepsilon)}{\partial \varepsilon_2} & \cdots & \frac{\partial f_M(\varepsilon)}{\partial \varepsilon_k} & \cdots & \frac{\partial f_M(\varepsilon)}{\partial \varepsilon_K} \end{bmatrix} \cdot \Delta\varepsilon + O(\Delta(\varepsilon)^2)$$

(2.13)

where J is the Jacobian matrix of F with respect to permittivity, which as known as the sensitivity matrix.

Among the Jacobian matrix, $\frac{\partial f_m(\varepsilon)}{\partial f_k(\varepsilon)}$ indicates the change of the m^{th} capacitance due to the change in permittivity at the k^{th} pixel. Hence, each column of the Jacobian matrix defines the relationship between capacitance and the permittivity between a certain two electrodes, which is called the sensitivity map. The sensitivity map indicates the sensitivity condition between two certain electrodes in ECT.

As an example, an 8-electrode ECT sensor was used, as shown in Figure 2-9. Five sensitivity maps of different electrode combinations of this circular sensor are plotted in Figure 2-10.

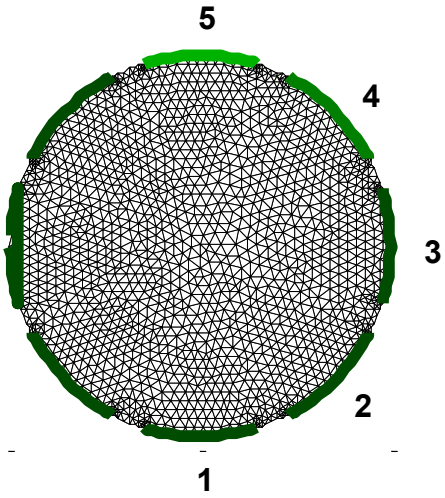

Figure 2-9: Computer model of an eight electrode 2D ECT sensor

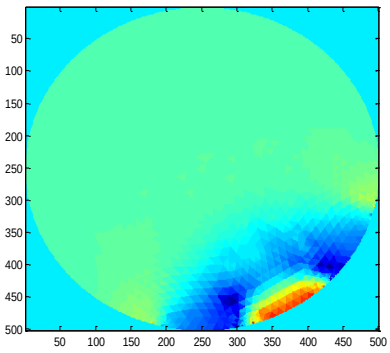

(a) Sensitivity map between electrodes 1 and 2

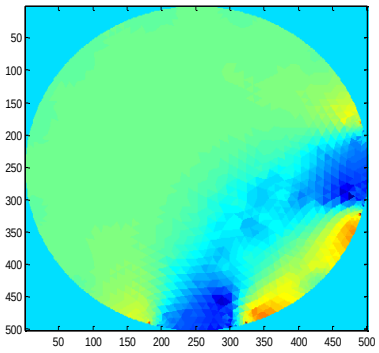

(b) Sensitivity map between electrodes 1 and 3

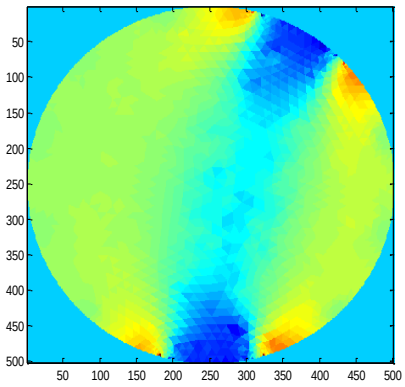

(c) Sensitivity map between electrodes 1 and 4

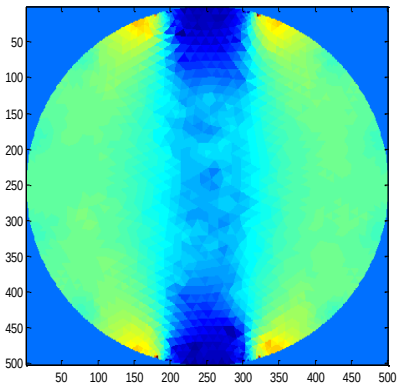

(d) Sensitivity map between electrodes 1 and 5

Figure 2-10: Sensitivity maps of the tubular ECT sensor

With respect to Figure 2-10, it can be seen that the sensitivity of the circular ECT sensor in the near electrode region is good while in the central region, it is poor. According to this, to detect an object in the centre using ECT tubular sensor is always challenging.

2.3 ECT inverse problem

The inverse problem is the process of calculating the permittivity given the capacitance data from electrodes. To start with single step inverse problems, several basic algorithms are introduced as below. ECT inverse problems are always ill-posed due to the fact that the Jacobian matrix is not in full rank hence the inversion of Jacobian matrix does not exist.

2.3.1 *Truncated singular value decomposition（TSVD）*

There is no universal formal definition for inverse problems. The definition of an ill-posed problem, according to Kabanikhin's article [147], Hadmard suggests that an 'ill-posed problem' is a problem for which the solution does not exist in its desired class, it is not unique (two or more) or the solution procedure is unstable. The inverse problems of ECT are ill-posed. Because the number of measurements is always smaller than the number of elements in ECT. Therefore, the Jacobian matrix is not full ranked.

SVD is considered as a tool for analysis of problems with ill-posed matrices and the truncated SVD method has been widely used to solve a variety of discrete ill-

conditioned problems [20, 22]. One of the disadvantages of using SVD is that it is frequently computationally expensive when dealing with large matrices [21].

Hence, to determine the ill-posedness of ECT inverse problem, SVD is used and presented as below:

According to Xu [63], any matrix $J \in R^{m*n}$ (in ECT A is the Jacobian matrix)

$$A = U\Lambda V^T \tag{2.14}$$

where U and V are unitary matrices, $U^T U = U U^T = I_m$, $V^T V = V V^T = I_n$. and $\Lambda \in R^{m*n}$ is a diagonal matrix of singular values of the matrix A, whose non-zero diagonal elements are $\lambda_1, \lambda_2, \ldots, \lambda_k$

The introduction of SVD of a Jacobian matrix J in ECT shows how much information the imaging system is able to potentially provide. As an ill-posed problem, ECT requires regularisation to stabilise the reconstruction procedure. The amount of information that can be extracted from the boundary measurements depends on the number of singular values that are not masked by the noise in the data. According to the Picard criteria [20, 22], only the singular values above the noise level will contribute to a reasonable result. In the Tikhonov regularisation, the regularisation parameter is selected to stabilise the inverse problem (mostly based on experiences). SVD also provides an important tool to analyse the behaviour of the underlying inverse problem [9], more specifically in ECT reconstruction procedure. Figure 2-11 shows an example of singular value decay for 2D ECT system. Further use of SVD will be demonstrated in detail in Chapter 5.

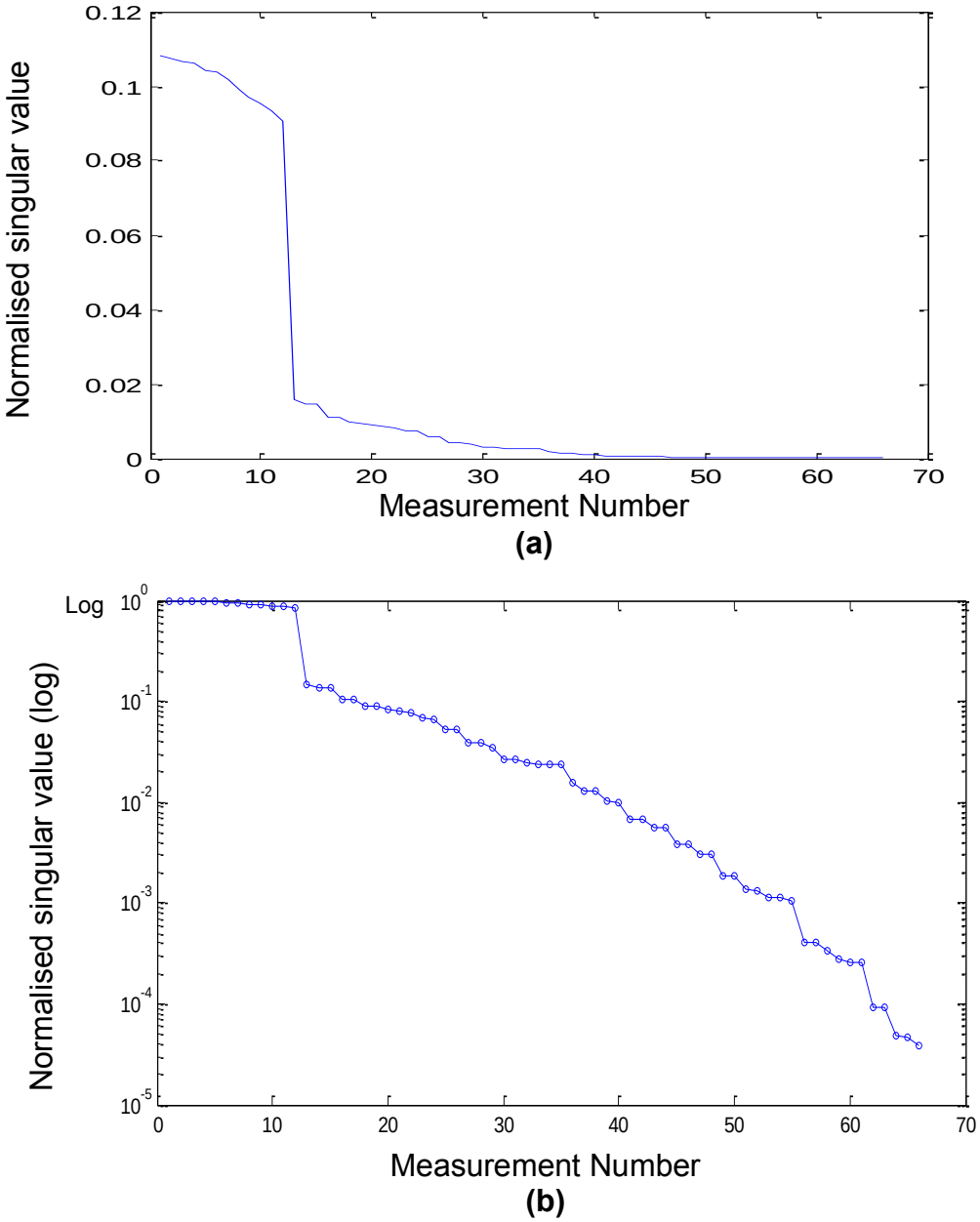

Figure 2-11: SVD plot for the Jacobian matrix from a 12 electrodes 66 measurement; (a) Standard SVD plot; (b) SVD plot in log format.

With respect to Figure 2-11, the singular value was plotted against measurement number. Figure 2-11 (a) shows the SVD plot with the standard values and (b) shows the SVD plot in semi-logarithmic scale. The SVD plots show the ill-posedness of the ECT inverse problem.

2.3.2 *TSVD algorithms*

Being an invaluable tool for analysis of problems with ill-conditioned matrices, the truncated SVD (TSVD) method has been widely used to solve a variety of discrete ill-posed problems. The method still lacks some theoretical criteria, in particular on selection of the number of singular values. The method of truncation determines the quality of a truncated SVD solution, but truncation is often done arbitrarily [63].

In practical evaluation in ECT, the ill-posed inverse problem can be written as the following linear algebraic model [13]:

$$y = Ax + \epsilon \tag{2.15}$$

where y is an array of boundary measurements collected by the data acquiring system of ECT. A is the Jacobian matrix with size of $(\mathrm{m} \times \mathrm{n})$ where m denotes the number of independent data and n is the total number of pixels in the image, x is an unknown pixel vector, and ϵ is the error vector which indicates the noise in the collected data.

Applying numerical methods, SVD for the Jacobian A is able to achieve. Without loss of generality, suppose the diagonal elements of A to be positive and to be arranged in decreasing order, $\lambda_1 \geq \lambda_2 \geq \cdots \geq \lambda_k > 0$, where k is the truncation parameter, $\mathrm{k} \leq \min(m, n)$.

The pseudo-inverse solution of Equation 2.14 is:

$$\hat{x}_{pi} = V\Lambda^{-1}U^T y \tag{2.16}$$

which is also the least squares approximations to the equation, because:

$$\hat{x}_{Is} = (A^T A)^{-1}A^T y = V(\Lambda^T \Lambda)^{-1}\Lambda^T U^T y \tag{2.17}$$

For the convenience of programming it is commonly rewritten in the least squares or pseudo-inverse solution in spectral form yields:

$$\hat{x}_{Is} = \sum_{i=1}^{t} \frac{u_i^T y}{\lambda_i} v_i \tag{2.18}$$

Dropping the smallest singular values and also the corresponding column vectors in matrices U and V by ignoring n-k number of small singular values in $\hat{x}_{Is}$, a least square and stable TSVD solution which is insensitive to the noise can be obtained as:

$$\hat{x}_k = \sum_{i=1}^{k} \frac{u_i^T y}{\lambda_i} v_i \tag{2.19}$$

2.3.3 *Linear back projection (LBP)*

Linear back projection (LBP) is a simple and a basic image reconstruction algorithm, and it has been commonly used in ECT for 2D and 3D image reconstruction due to its fast response ability.

As explained in Section 2.1, in a linear inverse problem the relationship between measured capacitance and permittivity distribution can be approximated and written in a linear normalised form: [3, 35]

$$\Delta C = J \Delta \varepsilon \tag{2.20}$$

Where ΔC , the system known, is an M x 1 vector representing the normalised capacitance matrix, M indicates the number of measurements, which can be calculated by using Equation 2.10 in Section 2.2.

J is an M x N vector representing the Jacobian sensitivity matrix (normalised capacitance with respect to normalised permittivity) $\Delta\varepsilon$, the system unknown, is an N x 1 matrix representing the normalised permittivity, where N means voxels. Then the system equations become:

$$\Delta\varepsilon = J^T \Delta C \tag{2.21}$$

LBP algorithm is always considered to be the fastest and simplest method in ECT. It is easy to achieve a fast reconstruction rate of a few tens of frames per second. However, in reality, the Jacobian matrix J is actually dependent on the unknown permittivity distribution due to the non-linear relationship between the capacitance and the permittivity distribution, as mentioned in the previous chapter. For this reason, the results are less good when the permittivity difference is too large.

Image reconstruction using the LBP algorithm in the linear case always relies on a sensitivity map while assuming a homogeneous permittivity distribution. By using proportionally adaptive thresholding and iteration, the blurring effect would be reduced significantly and quickly. However, the LBP algorithm is still the quickest method used nowadays due to the simple calculation process and assumptions.

2.3.4 *Tikhonov method*

Apart from the linear back projection algorithm in the previous section, Tikhonov algorithm is also commonly used and it is more advanced method compared to the LBP method. As said previously, the main task of image reconstruction for ECT is to determine the permittivity distribution from the measured capacitance. In the discrete

form, it is to find the unknown $\Delta\varepsilon$ from the known ΔC, while J acts as a constant matrix in linear image reconstruction cases, hence:

$$\Delta\varepsilon = J^{-1}\Delta C \tag{2.22}$$

However, J is an m*n matrix instead of a square matrix hence J^{-1} does not exist and this leads to another way to solve the ECT inverse problem as below:

$$\Delta C = J\Delta\varepsilon + Error \tag{2.23}$$

$$\Delta C = J\Delta\varepsilon \tag{2.24}$$

$$J^T\Delta C = J^T J\Delta\varepsilon \tag{2.25}$$

$$\Delta\varepsilon = \left(J^T J\right)^{-1} J^T\Delta C \tag{2.26}$$

$$\Delta\varepsilon = \left(J^T J + \alpha \mathrm{R}\right)^{-1} J^T\Delta C \tag{2.27}$$

R is the regulation identity matrix and the term $(J^T J + \alpha \mathrm{R})^{-1}$ has a filtering effect on the basic algorithms.

In a single step inverse problem, it is assumed that the Jacobian remains the same throughout the entire image reconstruction process. However, in reality, it is not. To solve this issue, the following section introduces algorithms in more than one step, which is known as the iterative method.

2.3.5 *Landweber iteration method*

Different from single step inverse problem solutions, [12, 13, 16, 17, 42] suggested that the iterative method is able to provide more accurate solutions as opposed to the direct inverse methods and that it has great advantages over a fixed Jacobian matrix. The numerical linear algebra algorithms are particularly useful when the size of a problem

is very large and hence it is difficult for direct methods to be used due to computational memory constraints.

The most commonly used and typical iterative reconstruction algorithm is the Landweber iteration method [13, 16], which can be defined as:

$$\Delta\varepsilon_n = \Delta\varepsilon_{n-1} + \beta J^T(C - J\Delta\varepsilon_{n-1}) \tag{2.28}$$

where β is the relaxation factor. [13, 14]

According to Equation 2.28, $\Delta\varepsilon_n$ is obtained by adding the previous result $\Delta\varepsilon_{n-1}$ and the correction term $\beta J^T(C - J\Delta\varepsilon_{n-1})$, where C-J$\Delta\varepsilon_{n-1}$ is the error between the measurement C and the re-calculated capacitance J$\Delta\varepsilon_{n-1}$.

The latest result is calculated by choosing $\Delta\varepsilon_0$ as zero and using SVD. Therefore, the general expression of the Landweber iteration can be expressed in equivalent in SVD form [13]:

$$\Delta\varepsilon_n = \sum_{j=1}^{p}[(1 - (1 - \beta\sigma_j^2)^n] \cdot \frac{u_j^T C}{\sigma_j} \cdot v_j \tag{2.29}$$

where p is the rank of matrix J; σ_j is the j^{th} singular value of matrix J and v are the left and the right singular vectors of the matrix J, respectively, and n is the number of iterations.

With respect to Equation 2.28, the result using n-step Landweber iteration can be achieved by using this algorithm. However, using the Landweber iteration algorithm, the convergent speed may be slow while it could be difficult in reality to decide on the optimal n.

To solve the time consuming issue of using the Landweber iteration algorithm, in a more efficient expression of this method using SVD, Equations 2.28 and 2.29 can be expressed as:

$$\Delta\varepsilon_n = \Delta\varepsilon_{n-1} + \beta DJ^T(C - J\Delta\varepsilon_{n-1}) \tag{2.30}$$

$$\Delta\varepsilon_n = \sum_{j=1}^{p}[1 - (1 - \beta d_j\sigma_j^2)^n] \cdot \frac{u_j^T \cdot C}{\sigma_j} \cdot v_j \tag{2.31}$$

where D is the pre-conditioner, which represents a diagonal matrix and d_j is the j^{th} diagonal element of matrix D. It can be seen that, for any J, and $|1 - \beta d_j\sigma_j^2| < 1$, Equation 2.31 converges. When this condition is satisfied, it can be expressed as:

$$0 < \beta d_j < \frac{2}{\sigma_j^2}, j = 1,2,\dots p \tag{2.32}$$

Literature [13, 67] suggests that, $\beta d_j\sigma_j^2 \leq 1$ should be satisfied and $\beta d_j\sigma_j^2$ should be close to 1, so that this method can converge faster.

A common way to select D is τ =1 and $d_j = \frac{1}{\alpha_j^2 + \gamma_j}$, where $\gamma_j > 0$ for any $j = 1,2,\dots.p$

Hence

$$d_j\sigma_j^2 = \frac{\sigma_j^2}{\alpha_j^2 + r_j} \tag{2.33}$$

In this way, D is more able to satisfy the conditions described above. Generally, the term r_j can be chosen as a constant for simplicity, which will lead to a sharpened reconstruction because of certain abnormal high frequency noise after a large number of iterations. [35]

2.3.6 *Non-linear Tikhonov reconstruction*

As has been discussed in the previous section, linear methods sometimes fail to provide accurate image reconstruction, due to the assumption made against the non-linear nature of the problem. In linear analysis the problem J(x) =y is assumed to be linear. However, Yang demonstrated [3, 13, 16] that, if it cannot be described by a linear mapping from x to y, applying a non-linear algorithm can sometimes improve both the image quality and accuracy. For example, in the separation of an oil and water mixture [35], the linear method would fail to solve the problem properly due to the high contrast [43, 53]. The predicted values using a Jacobian matrix have an error due to the perturbation and solving the forward problem.

A non-linear iterative algorithm requires computation of the Jacobian matrix in every iterations and re-calculation of the forward problem based on the latest update on permittivity values. Image reconstruction in ECT using regularised Gauss-Newton is to optimise $\|Cm - F(\varepsilon)\|^2 + \alpha^2 \|L\varepsilon\|^2$.

Therefore, the advanced formula in each iteration is:

$$\delta\varepsilon_{n+1} = (J_n^T J_n + \alpha^2 L^T L)^{-1} J_n^T ((C_m - F(\varepsilon_n)) - \alpha^2 L^T L \varepsilon_n) \qquad (2.34)^{[13,35]}$$

when n=1, this becomes a linear reconstruction. In this case, as mentioned for a linear algorithm, J_n is the Jacobian matrix, which is achieved with the permittivity ε_n, C_m is the capacitance measurements vector, and the forward solution $F(\varepsilon_n)$ is the predicted capacitance from the forward model with permittivity ε_n. The matrix L is the

regularisation matrix, which penalises extreme changes in permittivity removing the instability in reconstruction.

The residual error indicates the convergence of the inverse solutions, which can be defined as:

$$Residual\ error = \|Ax - b\|_2 \quad (2.35)$$ [146]

where A is the updated Jacobian matrix, b is the capacitance measurement, and x is the solution from the inverse problem. Residual errors converge in good condition once the algorithms are forced to run for more than one iteration.

Higher accuracy forward modelling is needed for non-linear reconstruction. This means that the closer the simulating analysis approaches the reality situation, the more improvement can be achieved using an iterative algorithm compared to a single-step method.

2.4 Summary

The forward problem is a process to simulate the electric potential, given the permittivity distribution and particular excitation at the boundary [1, 3]. By solving the forward problem, the potential data, which will be used in inverse problem to calculate the permittivity distribution, can be achieved. By using data achieved in the inverse problem, the image can be reconstructed as shown in the following chapter.

For linear image reconstruction, it is commonly simplified by assuming that the normalised capacitance varies linearly against the measurement before convergence. In reality, however, the relationship between the change of capacitance and permittivity is not linear. As a result, a more accurate model was used, and more difference between linear and non-linear analysis was achieved. In the results achieved, the differences were not that obvious because of the accuracy of the model. Hence, in the current experiments, it was difficult to visually detect the improvement produced by using a non-linear method.

CHAPTER 3 Approximate Error Method

Since most reconstruction algorithms rely on model-based approximations, it is important to ensure numerical accuracy for the model being used. FEM is a commonly used modelling technique for the ECT forward problem. The error modelling is used for mesh density and electrode size analyses are covered in this chapter. Due to the characteristic of the ECT technique, the size of the electrodes needs to be large enough to cover the entire image area. To solve the forward model accurately, a large number of elements are required in and around electrodes. Notably，a complete sensor model will provide the best solution to the forward problem. However, a large number of elements also bring in a large number of calculations, which results in longer computation time. For this reason, the advantages of incorporating discretisation and modelling error in ECT problem are studied. The approximation error model (AEM) has been used to account for discretisation error, and this allows using a coarse mesh for the forward problem to minimise the number of calculations, and achieving reconstruction accuracy close to that of a denser mesh.

This chapter is written based on a published work [44], to which, the first two authors contributed equally. The author of this thesis (second author of the publication) was in charge of the development of the algorithms, 2D model building and analysis while the first author provided the 3D model, analysis which can be seen in [44]. Because the author was focusing on 2D AEM analysis, 3D results are not included in this thesis. Current theory of AEM and the one presented in this thesis are only implemented in

second order algorithms. Hence only Tikhonov regularisation methods are used in this chapter.

3.1 Introduction

The characteristics of ill-posed inverse problems in ECT make it sensitive to measurement noise and modelling errors [70]. A complete sensor model (CSM) in ECT is the most accurate forward model. The CSM requires meshing the exterior shielding, inter-electrode shielding and the air behind the electrodes and external shields [8]. This will make the ECT computationally intensive. In [44], it investigated the differences (also called systematic error in this chapter) between CSM and a simple sensor model with a coarse mesh for the forward problem. AEM has been developed [69] to provide a statistical way to compensate for these errors [5]. AEM is currently used successfully on optical tomography and Electrical Impedance Tomography (EIT) technique [68]. This algorithm is presently able to be applied on similar inverse problems [73-78]. A major difference in 3D ECT is the setup of the capacitive sensors, which makes it very mesh intensive around the electrodes [44]. This chapter presents 2D ECT forward modelling using AEM in 2D ECT.

Literatures show that by making improvements to the forward model and the non-linear inversion technique [5, 70], it is possible to reconstruct complicated geometrical shapes by ECT [8]. The measured capacitance data C contains an error e, which is caused by noise. The other source of error is due to the discretisation of the problem using the FEM. Finite element theory says that, with increasing the number of elements for a

certain specific model, the element size h tends to zero and the accuracy in the model will increase. In another word, $f_h(\varepsilon_h)$ tends to C as h tends to 0. In some cases (depending on the mesh density and design of the measurement system), the discretisation error ($\psi(\varepsilon)$) can be even higher than the measurement error [5]. These errors can greatly reduce the quality of an image for coarser mesh-based FEM models.

3.2 Approximation error model

The aim is to improve the quality of the reconstructed images achieved by using coarser meshes and, thus, to reduce the computational time required to obtain a sufficient level of accuracy, which is very important to fast ECT imaging. The measurement error model is given by the approximate equation

$$C = f_h(\varepsilon_h) + e \tag{3.1}$$

where e is the noise error in the measurement data, h is the mesh parameter controlling the level of discretisation, and $f_h(\varepsilon_h) \to f(\varepsilon)$ as $h \to 0^+$ according to FEM, which is that the equation becomes exact within the measurement accuracy. The enhanced error model, which incorporates the discretisation error, is given by

$$C = f_h(\varepsilon_h) + [f(\varepsilon) - f_h(\varepsilon_h)] + e = f_h(\varepsilon_{bh}) + \psi(\varepsilon) + e \tag{3.2}$$

where $\psi(\varepsilon)$ is the discretisation error.

By determining the probability distribution for the modelling error $\psi(\varepsilon)$, it can be treated as measurement noise, and a coarser mesh can thus be used to obtain higher reconstruction quality by correcting the modelling error. The first step in achieving this

goal is to assume that the forward problem of ECT can be approximated to an appropriate level of accuracy by a densely discretised finite-dimensional model $\varepsilon_\delta \to f_\delta(\varepsilon_\delta)$ where $\delta > 0$ is small and $h > \delta$. Suppose $f_\delta(\varepsilon_\delta) = f(\varepsilon)$ within this level of accuracy and so the enhanced error model can be written as

$$C = f_h(\varepsilon_h) + [f_\delta(\varepsilon_\delta) - f_h(\varepsilon_h)] + e = f_h(\varepsilon_h) + \psi(\varepsilon_\delta) + e \tag{3.3}$$

A set of random samples can be generated from the permittivity solutions of size N, using both the denser mesh with permittivity solutions ε_δ and the coarser mesh with permittivity solutions ε_h. This can be achieved by randomising the location, size and permittivity distribution of spherical 3D objects and circular 2D object in material under examination, and then by using the Tikhonov regularisation approach to solve the inverse problem, for both the permittivity distribution ε_δ in the denser mesh and the permittivity distribution ε_h in the coarser mesh, for each random case. Assume that the solutions ε_δ from the denser mesh, are accurate and the discretisation errors in capacitance are calculated in each case using

$$\Psi_h = f(\varepsilon_\delta^{(i)}) - f(\varepsilon_h^{(i)}) \tag{3.4}$$

The distribution of the discretisation approximation error from the samples will be calculated by assuming a Gaussian error term, $\psi_h \sim N(\psi_h^*, \Gamma_{\varepsilon_h})$, using the approximations [5].

$$\psi_h^* = \frac{1}{N}\sum_{i=1}^{N} \psi_h^{(i)} \tag{3.5}$$

and

$$\Gamma_{\varepsilon_h} = \frac{1}{N-1}\sum_{i=1}^{N}\left[\psi_h^{(i)}\psi_h^{(i)T} - \psi^*\psi^{*T}\right] \tag{3.6}$$

Assuming the noise error is mutually independent and Gaussian-type, and considering $e \sim (e^*, \Gamma_e)$, where e^* is the mean and Γ_e is the symmetric and positive definite covariance matrix. The average discretisation error plus the average noise e^* provides the mean $E(n)$ of the noise vector, $n = \psi + e$. The covariance of the noise vector can be calculated using [5, 127]

$$\Gamma_n = \Gamma_\psi + \Gamma_e \tag{3.7}$$

By using the Cholesky factorisations [5]

$$L_{\varepsilon_h}{}^T L_{\varepsilon_h} = \Gamma_{\varepsilon_h}{}^{-1} \quad , \; L_{\psi+e}{}^T L_{\psi+e} = \Gamma_n^{-1} \tag{3.8}$$

These can then be incorporated into the ECT model, to correct for the discretisation error, along with the noise error, so that the common method (objective function) to obtain the solution to the inverse problem becomes:

$$Minimise\left\|L_{e+\psi}(C - f_h(\varepsilon_h) - \psi^* - e^*)\right\|^2 + \left\|L_{\varepsilon_h}(\varepsilon_h - \varepsilon_h^*)\right\|^2 \tag{3.9}$$

In linear form, this is equivalent to finding the permittivity that minimises the function:

$$Minimise\left\|L_{e+\psi}(J(\varepsilon_h)(\varepsilon - \varepsilon_h^*) - \psi^*)\right\|^2 + \left\|L_{\varepsilon_h}(\varepsilon_h - \varepsilon_h^*)\right\|^2 \tag{3.10}$$

Given that the actual ε is approximated by the simulated ε_{δ} , there will be measurement error e in both sets of solutions for ε. This means that the distribution for the measurement error can be taken as $e \sim N(0,\Gamma_e)$, where $\Gamma_e = diag(\sigma_{e,1}^2,\ldots,\sigma_{e,m}^2)$, where $\sigma_{e,j} = rel_e \left| C_j^* \right| / 100$ and rel_e is the relative noise of the system expressed as a percentage. In Equation 3.9, the instrument noise is not required as the capacitance differences of different measurement data are used.

3.3 AEM results comparison

3.3.1 *AEM for different mesh density*

The effect of modelling this error has been examined first, using the traditional pixel based approach for 2D mode. Figure 3-1 shows two computer models built for a 12 electrodes ECT system with different mesh densities. Figure 3-1 (a) is a coarse meshed model with 18300 elements, while (b) has a higher mesh density of 98384 elements. Assuming Figure 3-1 (b) is able to provide the best quality of image reconstruction, this model is taken as a reference ('true image') to pre-calculate the error between other models to model (b). Figure 3-2 shows the true 2D ECT image and a comparison between two cross-sectional images reconstructed on a coarse 2D meshed model (model (b) in Figure 3-1). In Figure 3-2, (a) was achieved without the inclusion of the error model (by using model (b) in Figure 3-1, hence this is the 'true image' in this case) while (b) and (c) were achieved by using model (a) in Figure 3-1. From the two results (b) and (c) in Figure 3-2, AEM was applied to result (b), while (c) was achieved by using the traditional Tikhonov algorithm.

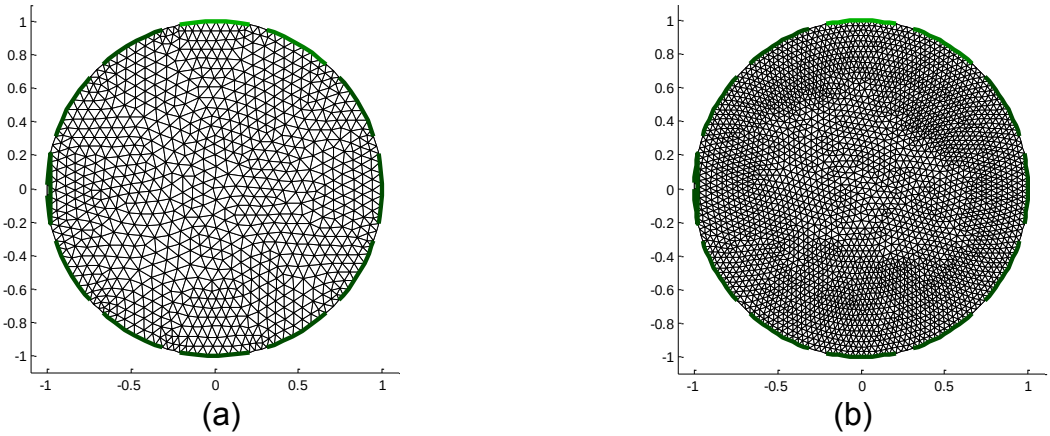

Figure 3-1: 2D ECT computer models used for AEM comparison: (a) coarse meshed model; (b) dense meshed model

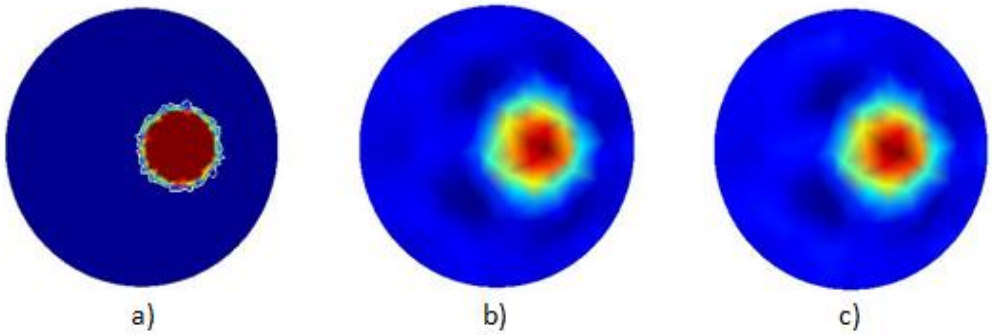

Figure 3-2: (a) 'True' image, (b) image with pre-calculated error, (c) image without pre-calculated error.

As far as Figure 5-2 is concerned, for 2D mode the image quality improvements are hard to be seen in visualisation. However, Figure 3-3 shows the error values of these two approaches and demonstrates that the inclusion of the error approximation model has enhanced the quality of the reconstruction through reducing error.

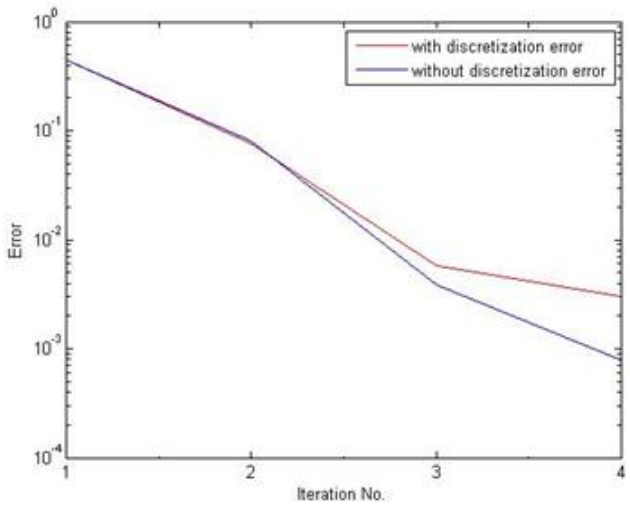

Figure 3-3: Comparison between error in the normal model and that in the enhanced error approximation model for 2D ECT mode

By accounting for modelling error through AEM, it is possible to gain more information by lower level of regularisation as shown in Figure 3-4. It is clear that more singular values are above the blue error line, representing the error in the enhanced error model, than the red line which represents the uncorrected 2D ECT model. Hence, this allows more detailed images to be achieved.

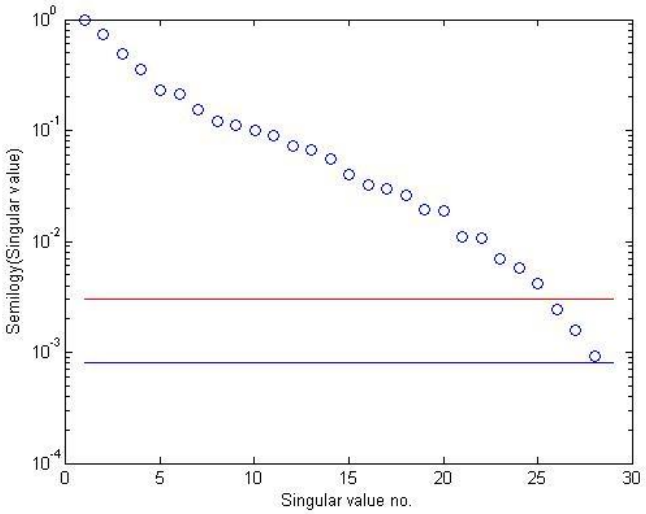

Figure 3-4: SVD graph with error levels for the model with discretisation error (red) and without discretisation errors (blue).

It is commonly known that by using a dense meshed model it is possible to improve image quality, but a large number of elements also bring in more calculations. As shown in all results in this chapter, by applying AEM between a coarse meshed model and a dense meshed model it is possible to improve the image quality using a coarse meshed model. At the same time, by applying this method to a coarse model also minimises the differences without increasing the number of elements and calculations compared to a dense meshed model. Several future tasks are discussed in the following chapter.

3.3.2 *AEM for other possible errors*

In this section, the AEM is applied to two models, which have same mesh density but different electrode sizes to demonstrate other uses of this method. The principle of the AEM is to calculate the predictable error and apply it to the result from the inverse problem, to minimise the systematic error. Apart from the systematic error caused by different mesh density, there are many other kinds of possibilities for systematic error to occur. In this sub-section, two different computer models were built, as shown in Figure 3-5, using the same mesh density. Meshed models were built with exactly the same dimensions and mesh densities, apart from the electrode size. Among them, model A has the correct dimension while the other model (model B) has smaller electrode size than the actual electrodes, as marked in red circles in Figure 3-5. Taking model A as the reference and images reconstructed by using this model as ‘true images’, the results are shown in Figure 3-6.

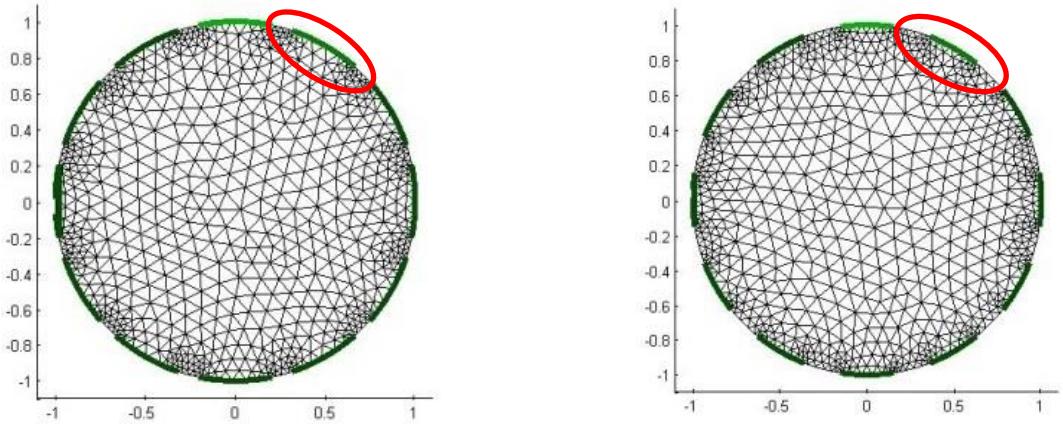

Figure 3-5: Computer model built for a 12 electrode ECT system

Initial experiments were carried out using model A and B from Figure 3-5 and the results are listed in Figure 3-6. Assuming model A is the perfect model, results achieved by using this model are the 'true image', as shown in column A of Figure 3-6. Results achieved by using the incorrect model (Model B) are listed in column B. The approximate error between model A and B was re-calculated and applied to the results from the inverse problem by using incorrect model B; results achieved by applying AEM are listed in column C in Figure 3-6.

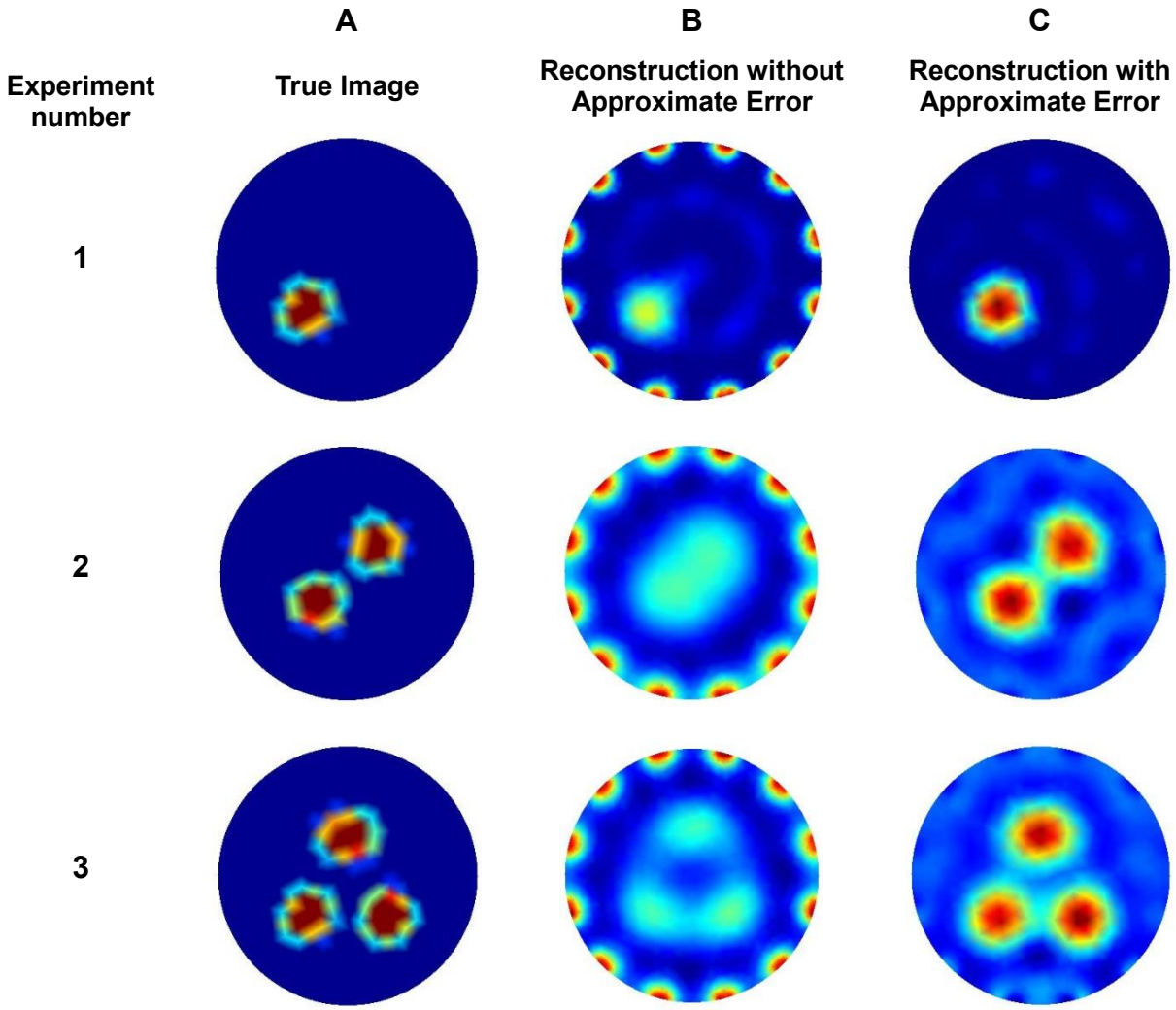

Figure 3-6: Initial test of image reconstruction: A: True images; B: Image reconstruction by using incorrect model; C: Image reconstruction by using incorrect model with AEM applied

With respect to Figure 3-6, images reconstructed without AEM clearly have poorer quality. Because of incorrect electrode size in model B, the results clearly show errors in neighbouring electrodes. With respect to experiment 3 in Figure 3-6, the samples, which were reconstructed without AEM, were connected together without being separated as they are supposed to be.

However, by applying AEM, the differences between results, which were achieved by using the incorrect model and correct mode, respectively, have been reduced, as shown in Figure 3-6. With the incorrect model (model B), the samples were well separated and the imaging error in neighbouring electrodes was reduced by using the AEM based model (as shown in column B and C). The test samples reconstructed in those results are much more clearly separated, as shown in the initial results.

Having shown the initial improvement, follow-up tests were carried out as shown in Figure 3-7. Five models were built with the same mesh density and dimensions apart from the different electrode size. Among these models, model E has the largest electrode size (correct model, electrode size same as the sensor). From models D to A, the electrode size is reduced when building the meshed model gradually (shown in the first column of Figure 3-7).

Among all models, A has the largest error in electrode size. Taking E as reference, the error between all sample models to model E (“perfect model”) was calculated and applied to the image reconstruction process. The results are shown in Figure 3-7.

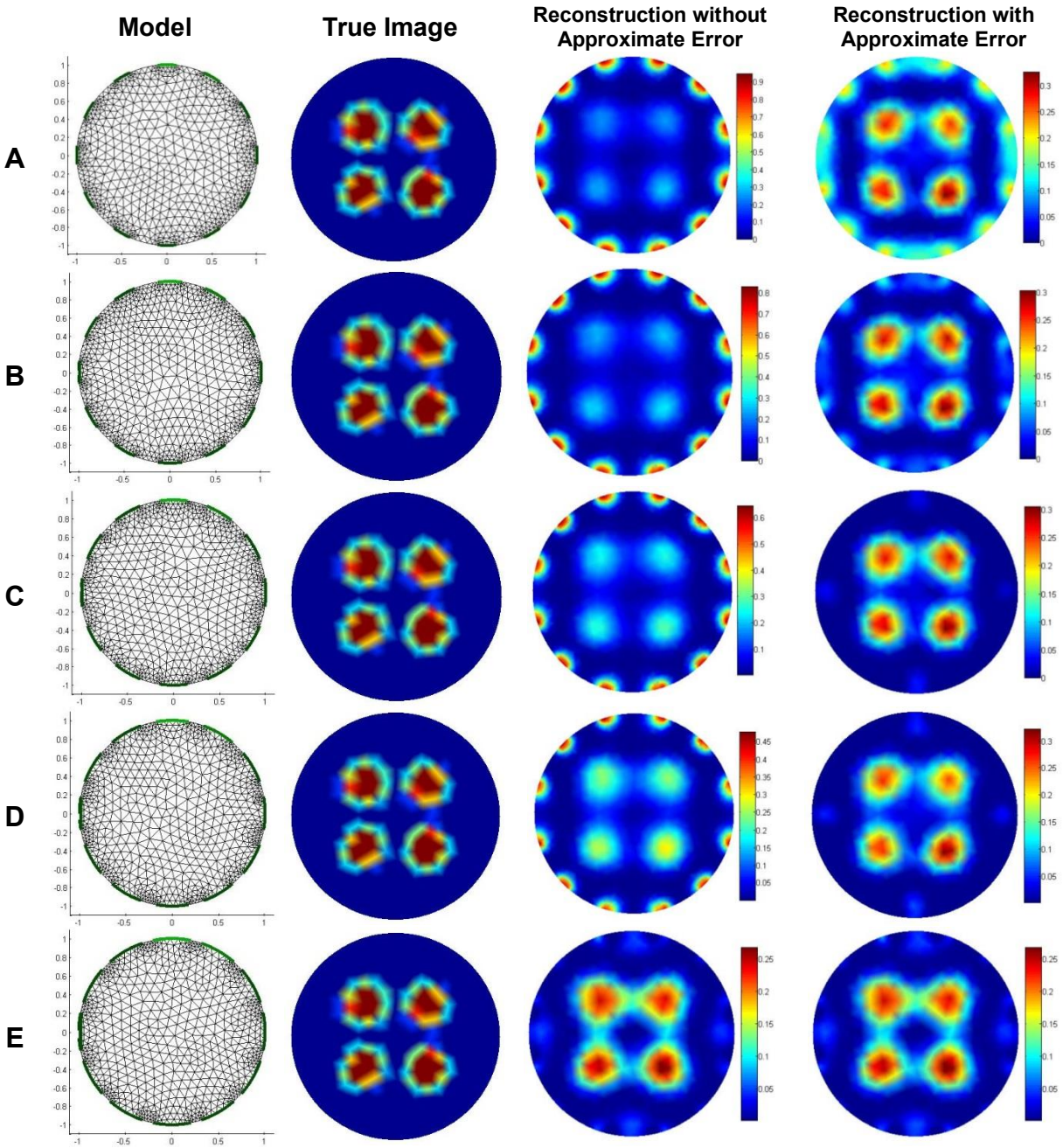

Figure 3-7: Comparison of image reconstruction with and without AEM

As far as the results shown in Figure 3-7 are concerned, taking model E (perfect model) as the reference, models A and B both have large error by comparing the results achieved using these two models to those using model E, this is due to the large error in the size of electrodes. Applying approximate error to the image reconstruction for models A and B, the error in neighbouring electrodes has been

reduced but not completely removed. The test sample has been reconstructed and a visual improvement can been seen. With respect to results achieved by using models C and D, due to the smaller difference (error) in size of electrodes to the reference model (model E), by applying AEM, those errors in neighbouring electrodes have been reduced using the standard Tikhonov reconstruction. Test samples are enhanced in both changing in signal and reconstructed size. Because model E is the perfect model and the calculated error was achieved by using model E as reference, it is hard to see any improvement by applying AEM to the process when using this model as shown in Figure 3-7 row E.

The cases of incorrect electrode size are not common in reality in the ECT, this has been taken as an example of one of the predictable systematic errors to demonstrate the application of AEM method.

3.4 Computational time

The error term and the inverse of the covariance of the error are calculated offline in AEM. The computational time of this process depends on the size of forward problem and the number of sample models. For 2D examples in this chapter, the computational time is 20 minutes (on Intel core i7) for 1000 sample models. Once the error term is pre-calculated, the computational time associated with Equation 3.10 is very close to the traditional Tikhonov based method (10% higher). Because the additional calculations of subtraction of the error term with traditional Tikhonov method is not computational intensive in 2D.

Presented in [44], due to the large amount of computational complexity of this process in 3D ECT, the GP GPU CUDA technology was applied to speed-up the process. Normally the AEM training can take a few days using Intel Core i7 (conventional CPU unit). MatLab AccelerEyes Jacket implementation provides about 9 times speed-up using Nvidia GT555M graphic processing unit. Thus, the AEM training process can be completed in a reasonable time (8-9 hours) in 3D for 5000 training samples.

Since the AEM are developed in second order method such as Tikhonov algorithm and not yet implemented for first order method such as Landweber and LBP algorithms, the application to a large scale ECT problem is more challenging

3.5 Summary

This chapter presented simulation study of 2D ECT. The use of AEM has been shown as an effective method of modelling 2D ECT. However, some error is created in the discretisation of the problem. In this chapter, it has been shown that a noticeable improvement in the image reconstruction in 2D is achieved by modelling the discretisation error using AEM in finite element, thus resulting in improved image reconstruction with coarser meshes or incorrect sensor models (incorrect electrode size model) and reduced computation time. The negative influence to the image reconstruction quality due to potential error in model dimension can be minimised by using AEM. Apart from this, the AEM method can be applied in reducing the difference

between using a complete model and an incomplete model (i.e. a simplified ECT sensor model without grounded shield).

CHAPTER 4 3D Planar Array ECT

In the majority of non-destructive evaluation (NDE) applications for ECT there is only limited access to the targeted objects, making conventional circular array ECT impractical. In this chapter, a planar array ECT system is developed and proposed for 3D sub-surface imaging as a form of limited access tomography. The sensor development, practical implication, capability and limitation of the proposed planar array ECT are discussed. Experimental results are used to evaluate the system performance. A depth of up to 53% of the length of the sensor array can be achieved using an array of 12 electrodes in a three by four arrangement.

4.1 Introduction

To date, most ECT systems have been designed and built using a traditional arrangement of electrodes, where the electrodes are arranged circumferentially around the target object [3, 5, 6]. This type of arrangement has a circular or rectangular geometry and requires free access around the complete periphery, when 'full access tomography' can be achieved [1, 5, 7, 8, 10, 19]. However, there are a number of potential applications where it may be difficult to examine the object in a 360 degree case and image reconstruction cannot be implemented using a traditional ECT system.

There has been growing interest in planar array ECT for several new application areas in the past few years. In [60] commercial finite element software was used to model the forward problem for 3D planar array ECT. A 2D imaging planar array ECT was presented for a possible security scanning application [14, 58, 60, 124]. A single sided capacitive imaging system was developed for applications such as inspection of composite materials [14]. The system was applied to several NDT applications such as inspection of composite materials [14]. The capacitive imaging system uses a single pair of electrodes. In [14] the authors stated the advantages of an array imaging system for rapid inspection. In this chapter, the development of planar sensor model and system setup is presented, followed by experimental evaluation. A series of experiments were carried out and demonstrated.

4.2 Sensor description

The planar sensor array was built consisting of 12 electrodes, which were constructed using conductive copper tape as shown in Figure 4-1. The 12 electrodes were arranged in a 4 x 3 matrix array and attached to a plastic square plate with a surface area of 25 cm x 25 cm and 4 mm in thickness. The dimension of the electrode array is 17 cm x 17 cm. There are grounded conductors between all electrodes and the surrounding area of the sensor array. A thin 5 mm conductive ground is used to separate electrodes. The planar electrodes are attached to a 2 mm thick plastic plate with relative static permittivity (dielectric constant) of 1.6. A metallic shield, on the rear of the sensor array, is used to partly shield the planar array from external interferences. Capacitance was measured using the PTL300E (Figure 4-1 (a)) from Process

Tomography Ltd. The PTL300E ECT system allows 12 channel capacitance measurements with frequency of 1.25 MHz, which allows capacitance values down to 0.0003 pF (0.3 femtofarads) to be resolved. This ECT system is capable of data collection at 100 frames per second. This makes it suitable for use as a rapid imaging device. According to the system instruction, the capacitance measurement noise level is typically better than 0.07 fF rms and the effective measurement resolution is 0.1 fF.

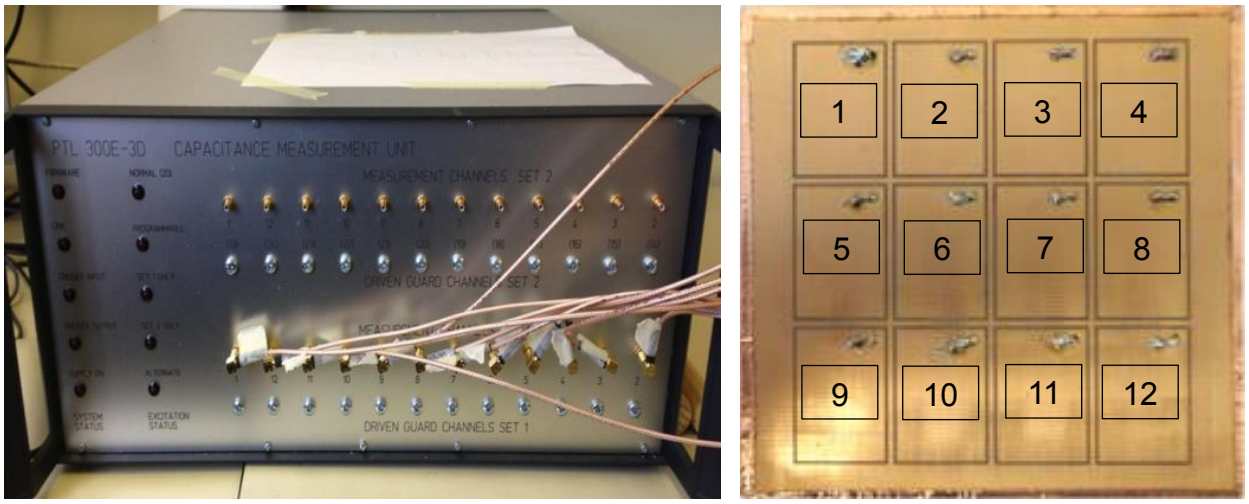

(a) Measurement Unit (b) Electrode arrangements

Figure 4-1: 3D planar array ECT system: (a) ECT 3D measurement system (b) electrode arrangements in the array.

4.3 Image reconstruction

In the case of a planar ECT, a wooden block covering the region of interest for imaging was used for C_{high}. The wood block has a size of 17 cm x 17 cm x 17 cm, which is able to cover the whole area of interest for imaging over the surface of the planar array ECT. Figure 4-2 shows the meshed model generated by using Netgen mesh generator [54], with the same geometry as the experimental planar sensor. The number of

elements in this mesh is 81834**.** By solving the forward model [3] it is possible to evaluate the capacitance data, which then can be used in the inverse problem.

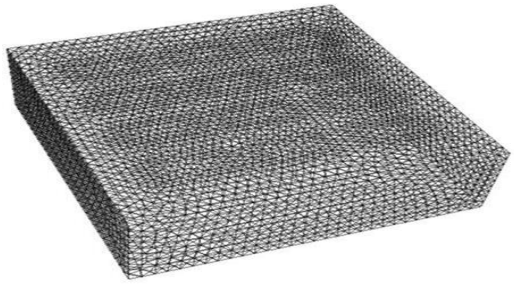

Figure 4-2: Mesh model for the planar sensor

The proposed sensor has 12 electrodes and hence there are 66 measurements. As shown in Figure 4-3, the simulated measurement data and experimental measurement data for free space have a certain difference. A complete sensor model can further improve the accuracy of the forward model [44], but also makes the computing of the forward model more costly.

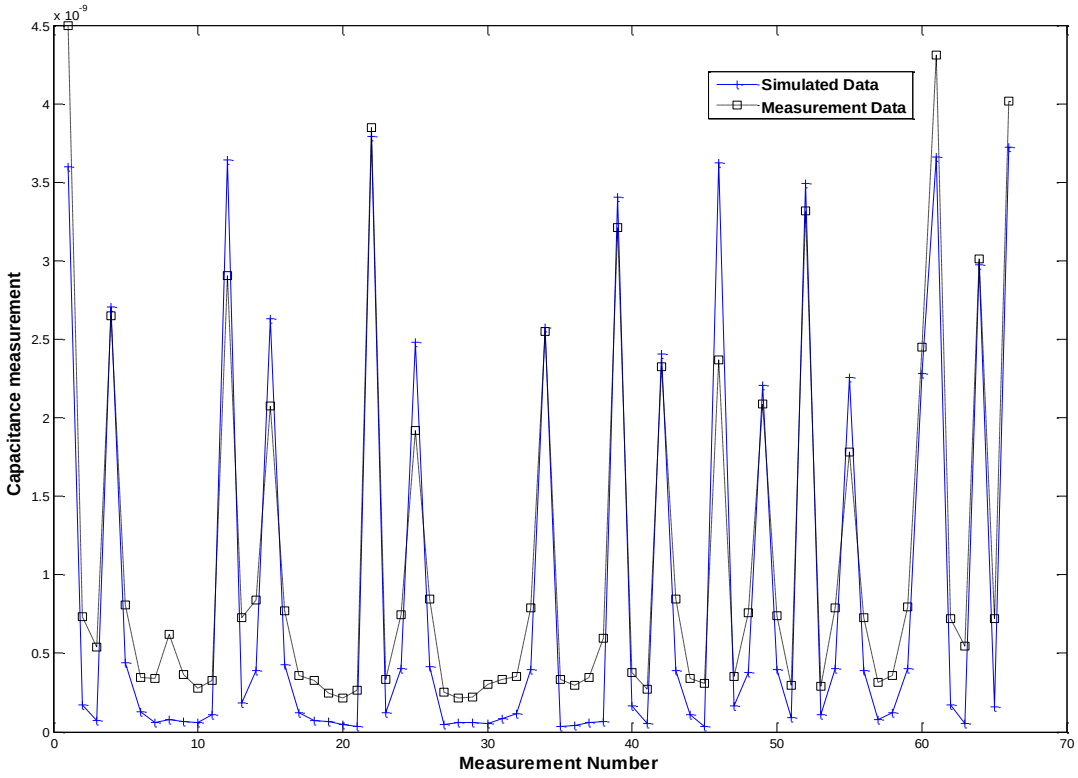

Figure 4-3: Simulated and measured capacitance.

As explained in Chapter 2, the relationship between capacitance and the permittivity of each voxel is non-linear. Therefore a fixed Jacobian matrix is used to linearise this relationship. Each row of the Jacobian matrix represents the sensitivity of one set of measurement data with respect to all voxels. Each row of the Jacobian matrix (also called the sensitivity map) indicates the relationship between capacitance and the permittivity of each combination of electrodes [1, 7].

Within the Jacobian matrix, the derivatives indicate the change of the m^{th} capacitance due to the change in permittivity at the k^{th} voxel. Therefore, each column of the Jacobian matrix indicates the relationship of the capacitance and the permittivity between two specific electrodes, which is the sensitivity map.

Regarding the electrode arrangement in Figure 4-1 (b), two examples of the sensitivity maps are shown in Figure 4-4. While the nearby electrodes are producing higher capacitance data ((b) in Figure 4-4), the diagonal electrodes show good depth detection but noisier data ((a) in Figure 4-4).

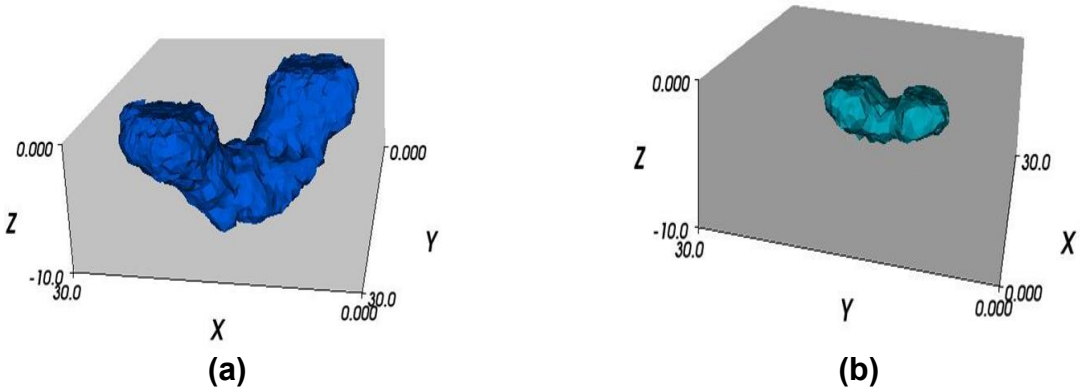

Figure 4-4: The sensitivity maps for planar array ECT: (a) Sensitivity maps for electrodes 1 and 12. (b): Sensitivity maps for electrodes 5 and 6

Planar array ECT is an open boundary imaging system, and depending on the selection of the range of interest for imaging, many voxels will have very small sensitivity to various capacitance measurements. In this chapter, the Jacobian matrix is converted into a sparse matrix by applying a sparse function. Meanwhile the smallest values in the Jacobian matrix are set to zero. Hence the Jacobian matrix memory consumption is minimised in an efficient way and this shows a significant improvement in ECT processing time. However, some information in the Jacobian matrix is lost while its values are set to zero.

The Landweber method is a commonly used algorithm to solve the inverse problem in ECT [2, 13]. As stated in Section 2.3.5, the main task of image reconstruction for ECT is to determine the permittivity distribution from the measured capacitance. In the discrete form, it is necessary to find the unknown $\Delta\varepsilon$ from the known ΔC, while J acts as a constant coefficient matrix in linear image reconstruction cases. In this study, Landweber iteration was used [16] (see equation 2.28).In equation 2.28, τ is the relaxation factor chosen to be 0.5, with 200 iterations for experiments in this chapter.

Several image quality measures were presented in [146], such as resolution (RES), positioning error (PE) and ringing effect (RNG). A modified image quality parameter, normalised resolution (NRES), is used to define the variation of the image quality with the depth. Image resolution, which is calculated using the equations defined in [12], measures the ratio of the voxel number in inclusions (in the case of the experiments in this chapter) to the total voxel number [12]. The total voxel number represents the volume of region of interest for imaging. It can be defined as:

$$RES = \frac{1}{V}\sum_{k}[\hat{x}_k \geq \frac{1}{4}\max_{j}(\hat{x}_j)] \quad (4.1)$$

where $\hat{x}_k$ is each voxel in the reconstruction inclusion, and V is the volume in the pixel of the true permittivity distribution.

4.4 Results and discussion

Here, the experimental results are presented for a planar array 3D ECT system. For this purpose, extensive simulations and experiments have been carried out, which show the feasibility of 3D planar array ECT imaging. In the following sections, the simulation study to systematic experimental tests has been extended. Dry wooden samples with dielectric constant around two to six were used in these experiments. Single object and multiple objects were reconstructed. Depth evaluation tests were carried out and all results are presented in this section.

4.4.1 *Single object testing*

In this experiment, single objects of different sizes were placed very close to the sensor at different locations on the planar array, as shown in column (a) of figures 4-5 and 4-6. Two dry wooden blocks were tested as a target sample. The larger wood block (sample A) was 150 mm x 50 mm x 50 mm and is shown Figure 4-5, while the smaller block was 50 mm x 50 mm x 50 mm (Figure 4-6). These two samples were placed in different locations in the near sensor region, examination results are listed. 3D results are listed in column c in both Figure 4-5 and Figure 4-6. As it is difficult to see the

location by exporting 3D results into 2D figures, cross-sectional images of corresponding results are added in column b in both figures to show the locations of reconstructed results. With respect to figures 4-5 and 4-6, it has shown that the planar ECT system is able to reconstruct single objects in any location when it is very near to the sensor region as shown in Figure 4-5 and Figure 4-6.

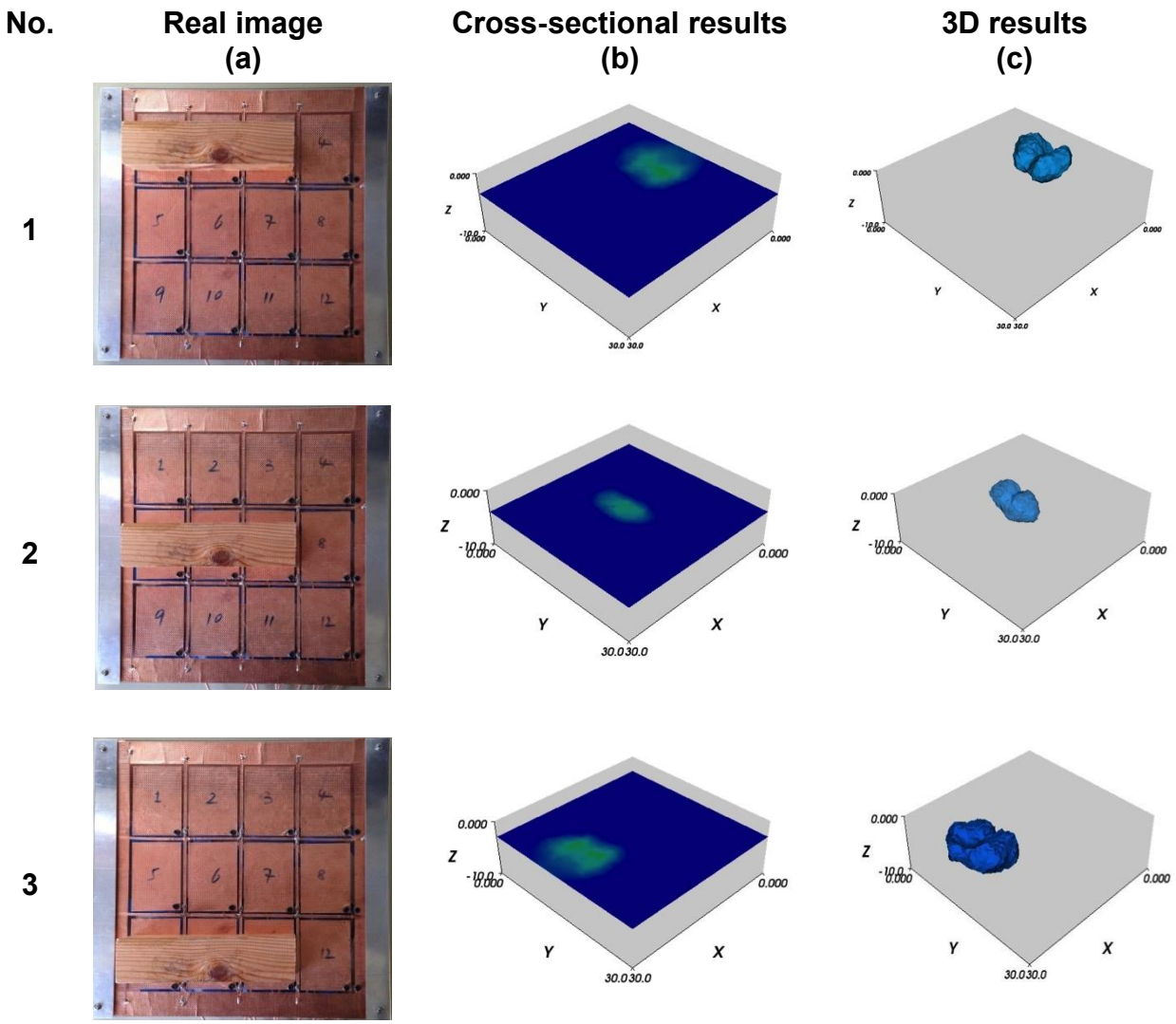

Figure 4-5: Results of reconstruction of single object in different location near the sensor (150 x 50 x 50mm target). (a): true object, (b): cross sectional image, and(c): iso-surface image

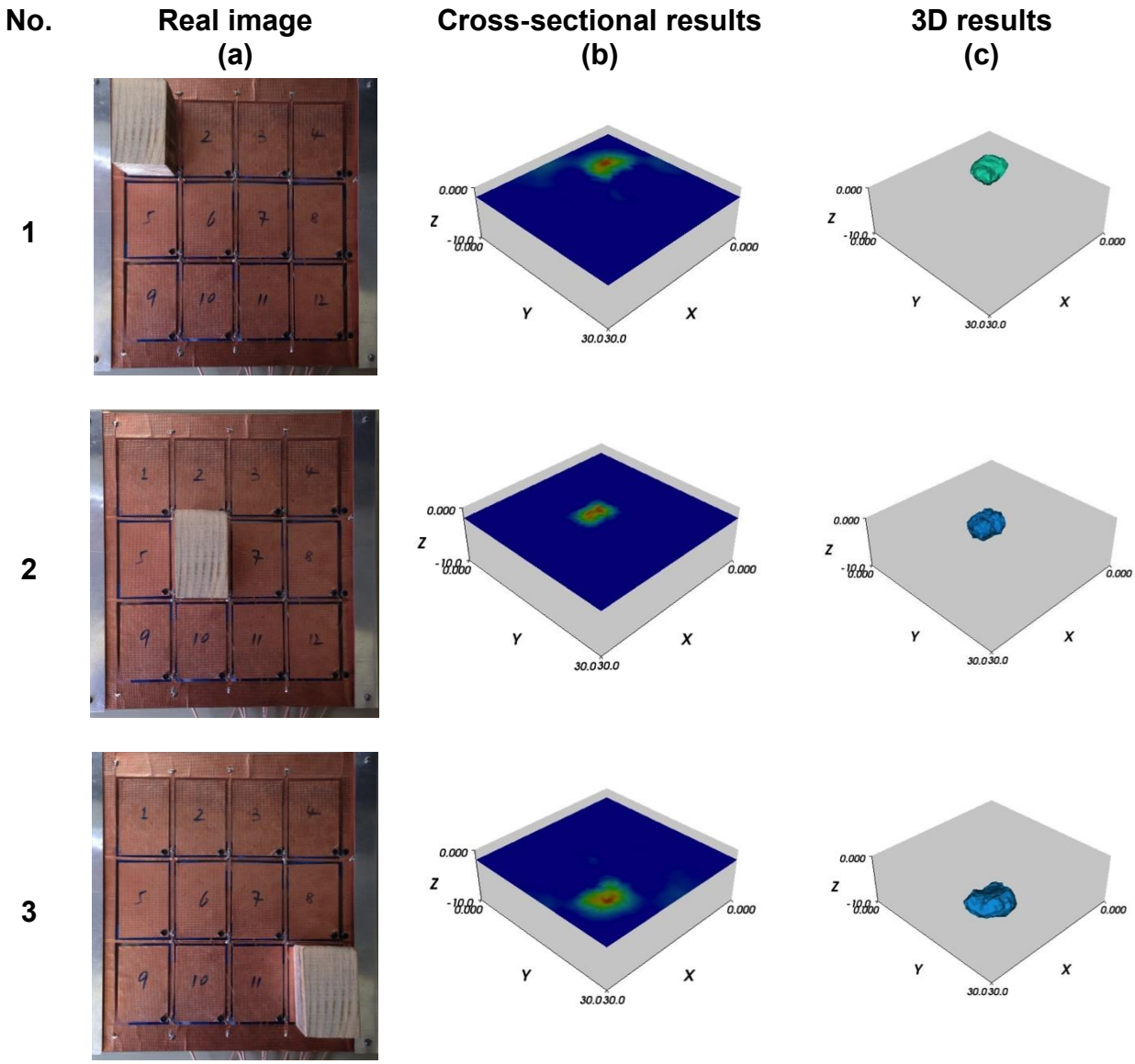

Figure 4-6: Results of reconstruction of single object in different location near the sensor (50 x 50 x 50mm target). (a): true object, (b): cross sectional image, and (c): iso-surface image

4.4.2 *Multiple object testing*

As far as the results achieved in Section 4.4.2 are concerned, to test the performance with multiple objects, further tests were accomplished.

In this section, the experiment of detecting multiple objects using the planar ECT sensor has been demonstrated. Maximum five wooden blocks (Four samples of size

30 mm x 20 mm x 50 mm and one has size 10 mm x 20 mm x 50 mm) were tested in different locations near the sensor surface, as shown in column a in Figure 4-7.

No.	Real Image (a)	Cross-sectional results (b)	3D results (c)
1	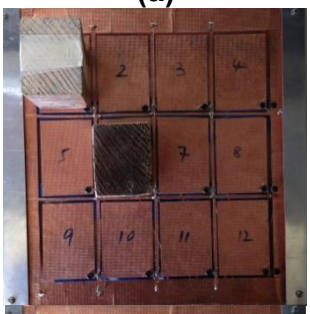	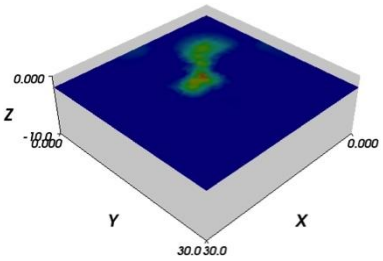	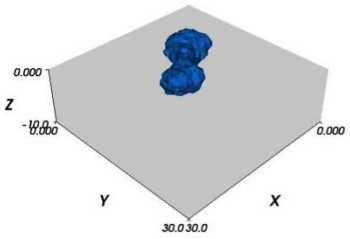
2	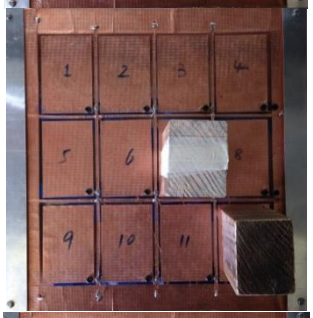	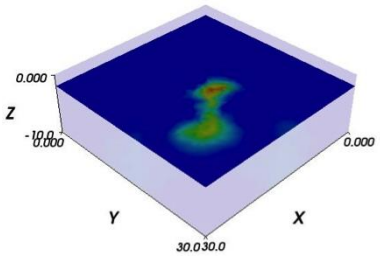	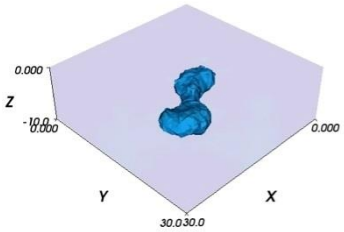
3		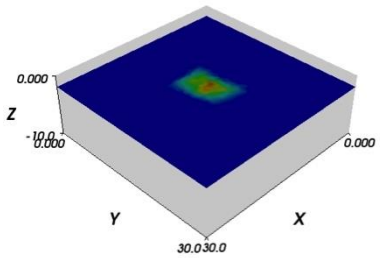	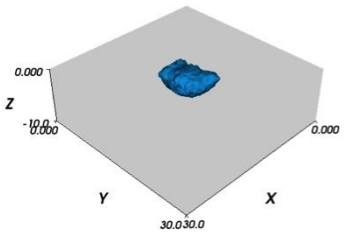
4	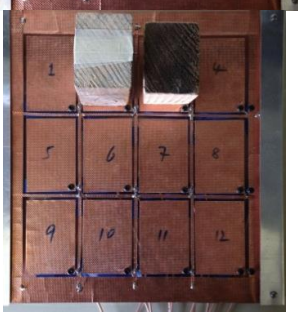	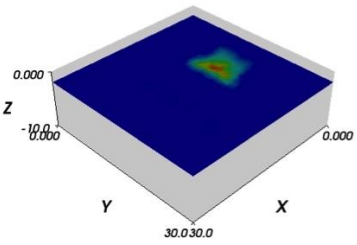	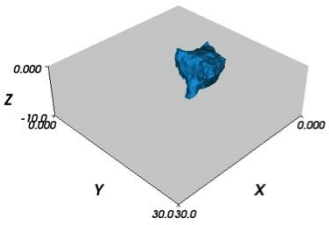

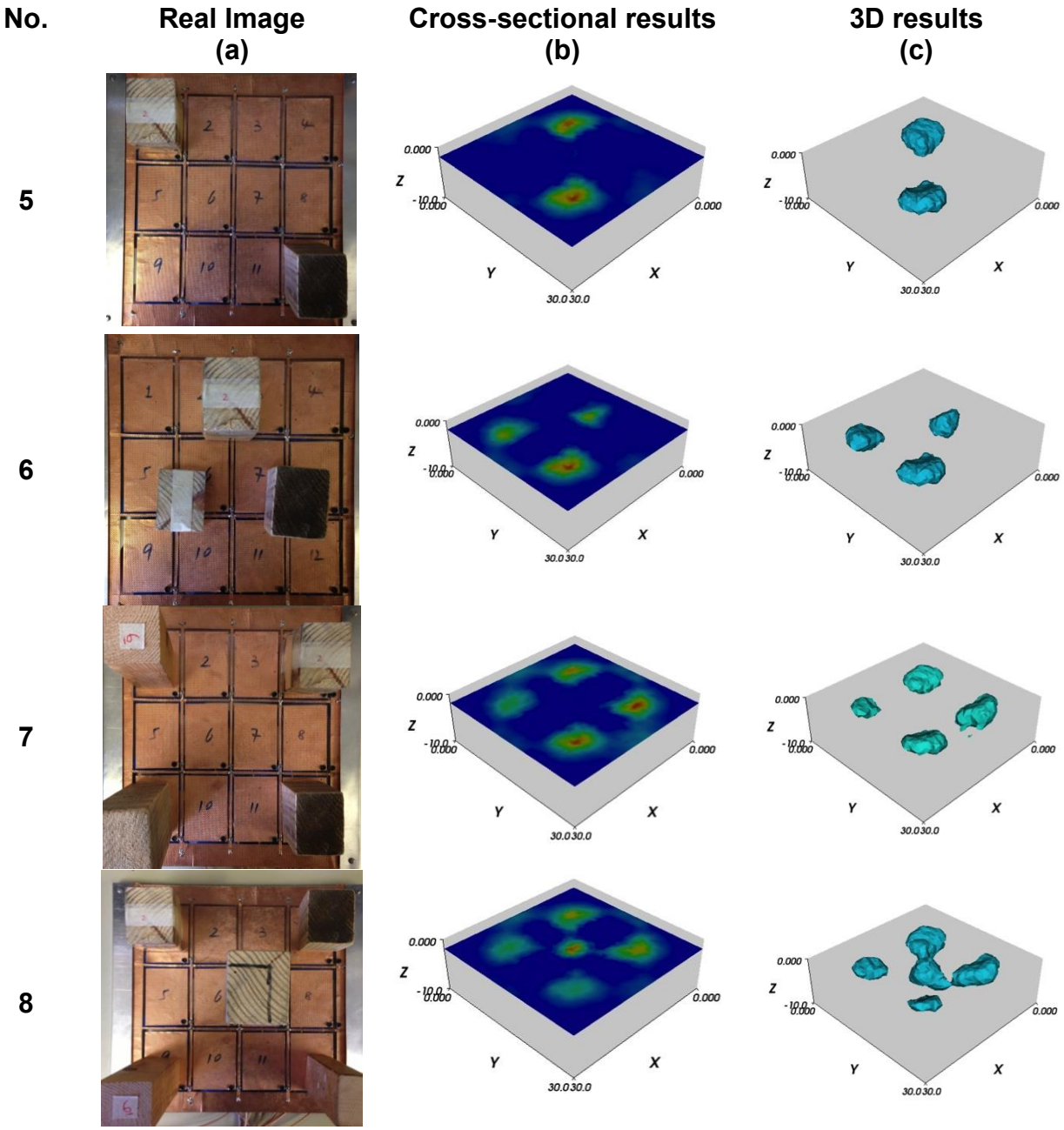

Figure 4-7: Results of reconstruction of multiple objects in different location near the sensor. (a): true object, (b): cross sectional image, and (c): iso-surface image

With respect to Figure 4-7, multiple wooden objects were detected and re-constructed with different locations by using 3D planar array ECT. This shows that the actual sensitivity of the planar ECT sensor is capable of detecting multiple objects attached to

the sensor in different locations within the near-sensor region. For example, when the wooden blocks were close to each other, as shown in experiment numbers 1 and 2, it was still possible to discriminate the two blocks. However, once samples were too close to each other, it was hard to separate them in image reconstruction, as shown in experiments number 3 and 4 in Figure 4-7.

4.4.3 *Depth detection*

In the previous two sections, the feasibility of the planar ECT system was investigated for object(s) close to the plane array sensor. In this section, the depth of penetration of the planar ECT system for potential sub-surface imaging applications will be examined. As shown in Figure 4-8, the test involved hanging an object from a steel rig, which was far enough from the sensor to minimise its influence on the system. The object was placed between the 6^{th} and 7^{th} electrodes, while the distance between the object and the sensor was varied in steps of 1cm to determine the maximum depth that the planar ECT system could sense.

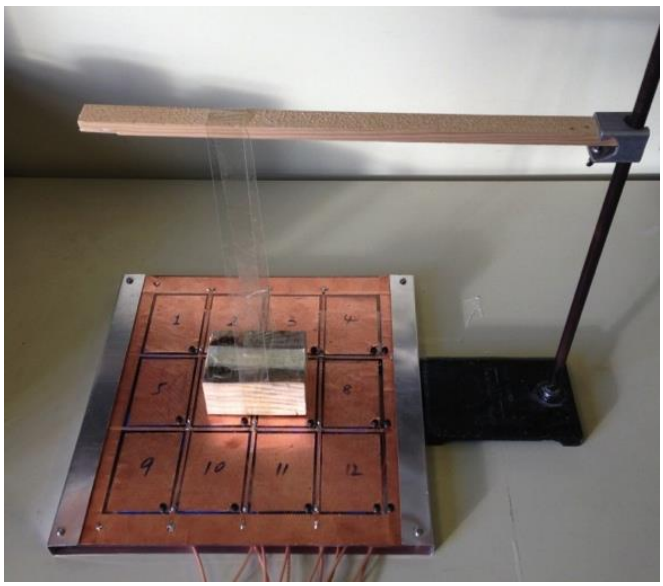

Figure 4-8: Experimental set-up for depth sensitivity

No.	Distance	Slice image (a)	3D View (b)
1	0 cm	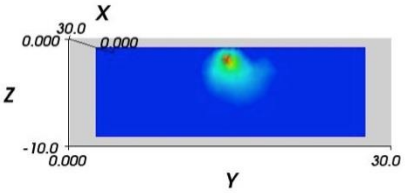	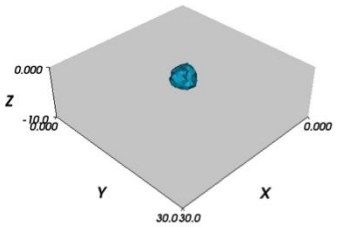
2	1 cm	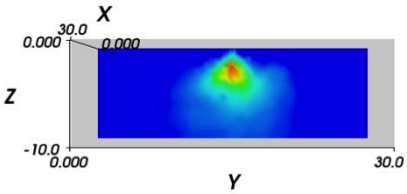	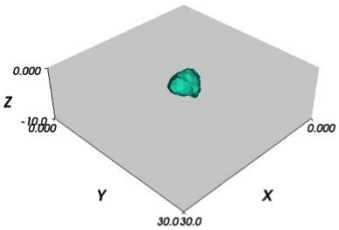
3	2 cm	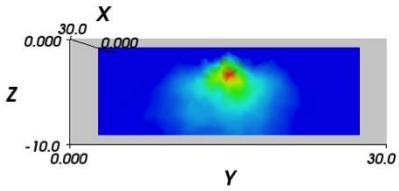	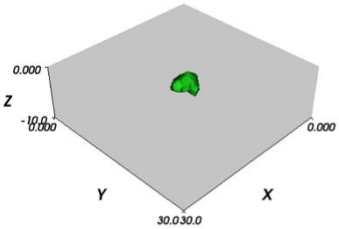
4	3 cm	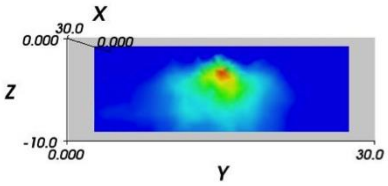	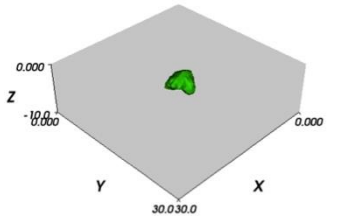
5	4 cm	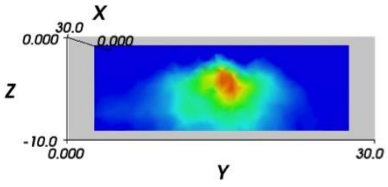	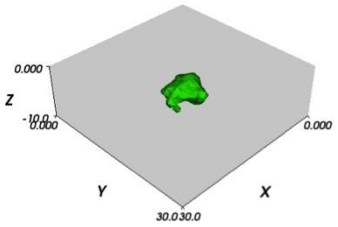
6	5 cm	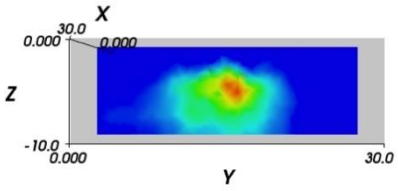	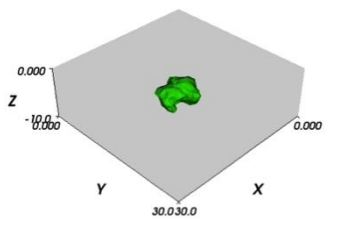

No	Distance	Slice image (a)	3D View (b)
7	6 cm	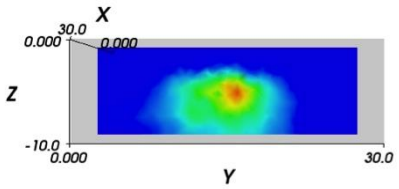	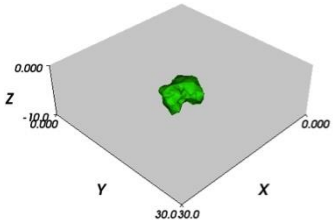
8	7 cm	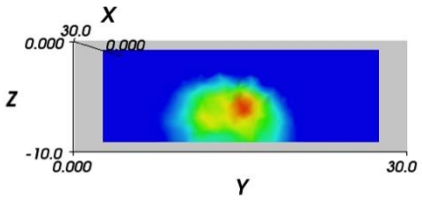	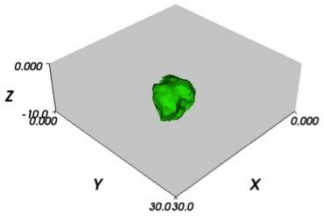
9	8 cm	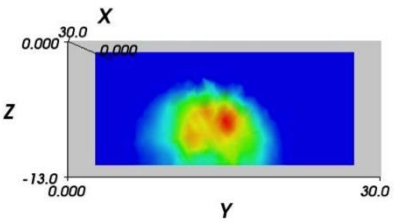	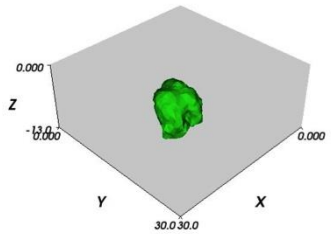
10	9 cm	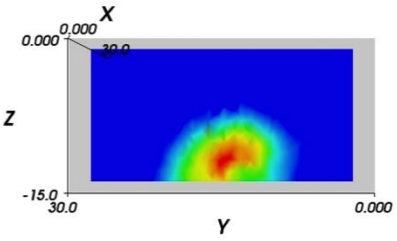	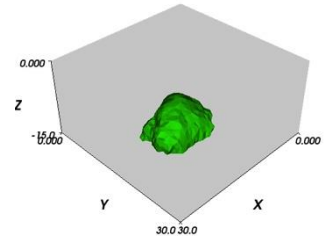

Figure 4-9: Results for single object in different location near the sensor

As shown in Figure 4-9, ten sets of experiments were carried out. In these experiments, the distance between the test sample and 3D planar array ECT sensor was increased gradually in steps of 1cm. The 3D results of each experiment are listed in column c, while the side view of cross-sectional results are listed in column b to understand the locations of reconstructed sample by using the planar array ECT

sensor. With respect to the results in Figure 4-9, there is a drop in the sensitivity of the planar ECT sensor, which consequently results in a decrease of resolution of the reconstructed results as the distance between the test object and sensor is increased. The maximum distance, at which the system was still able to noticeably detect the wooden object, was at least 8 cm for an array of 17 cm x 17 cm (area of electrode array). A plot of resolution against the depth is shown in Figure 4-10.

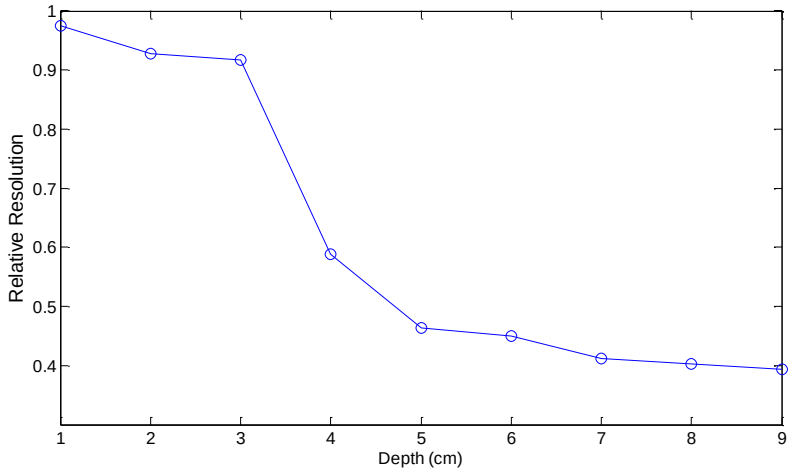

Figure 4-10: Resolution plot against the varying depth

Figure 4-10 shows the change in resolution of the reconstructed image with varying depth of the object moving away from the sensor. With respect to the first three tests, the resolution remains above 90% and goes down slightly when the depth is less than 3 cm. The resolution drops sharply when the depth reaches 4 cm and is totally lost after the depth goes above 9 cm, as shown in both Figures 4-9 and 4-10. This is an experimental observation and could be influenced by noise. In Figure 4-9, with increasing depth, cross-sectional results became bigger with increasing depth. The size of the reconstructed sample is bigger than the true size when the sample was far from the sensor. Because the noise becomes more dominant in the signal change

(ΔC in equation 2.21) with the increasing in depth compared with the actual signal change due to the permittivity of the test sample. This can be further confirmed by information provided in Figure 4-10.

4.5 Other potential applications

Several new studies of planar array ECT are shown for detection of high contrast permittivity imaging void detection, and imaging floating metals.

4.5.1 *Water level detection*

By taking advantage of the fact that water has a relative permittivity of 80, it is possible to achieve a higher change in signal. To further test the 3D planar array ECT system with a high contrast test sample, a number of experiments were carried out and both real images and reconstructed images are presented in Figure 4-11.

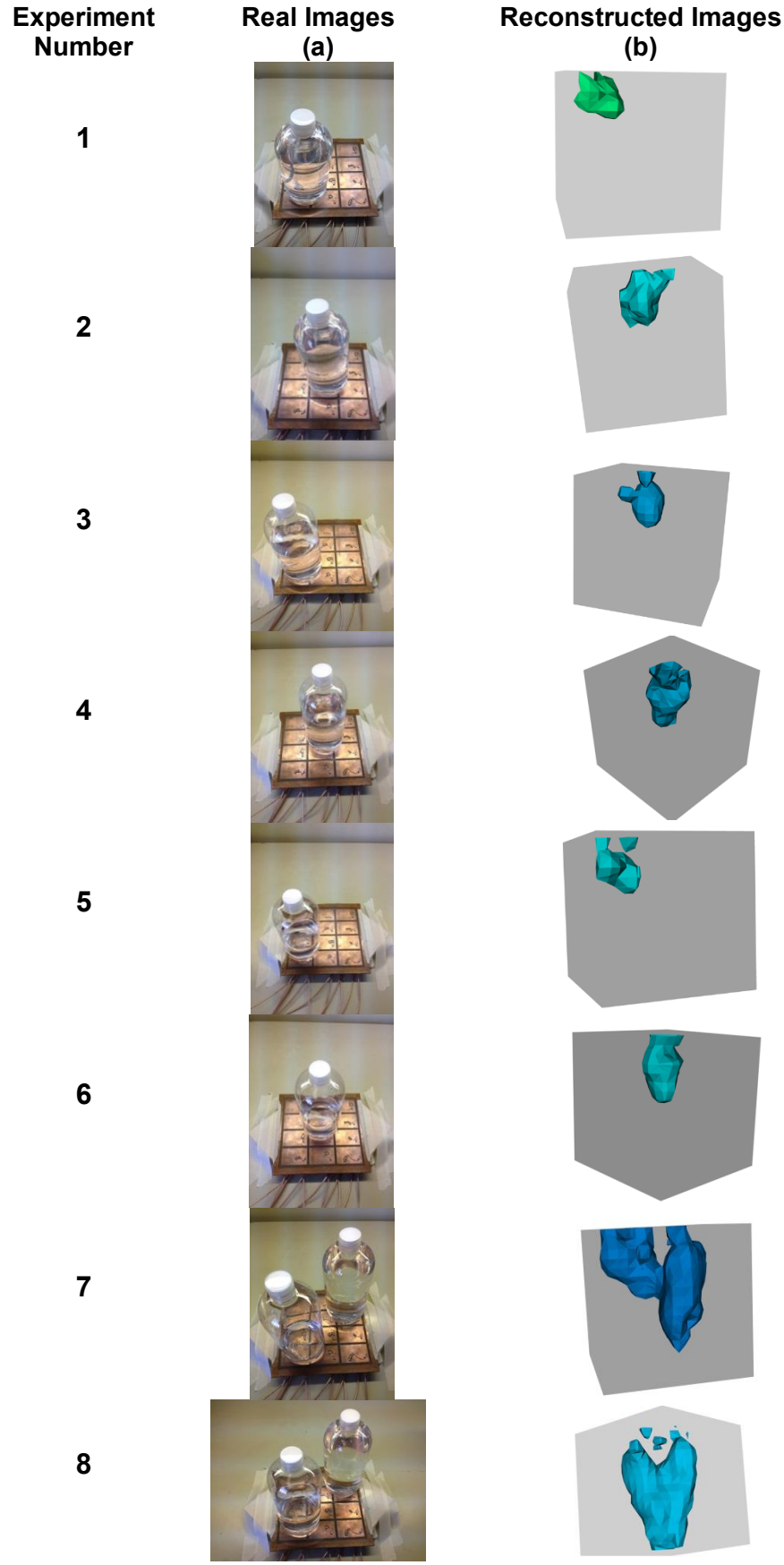

Figure 4-11: Water level testing results

With respect to experiment sets 1-3 in Figure 4-11, a quarter-filled bottle was tested in different locations near the planar array sensor. The results show that a high contrast sample (water) within the near sensor region was detectable.

To further investigate the depth detection, same bottle was half-filled and tested, as shown in experiment sets 4-6. The results also provide reasonable information with increasing water level. Experiment set 7 was carried out with a set of a quarter-filled bottle and a fully-filled bottle while set 8 was carried out with a set of a half-filled bottle and fully-filled bottle respectively.

With contrast, the water level can be detected in these experiments within the planar array sensor imaging region at near-sensor depth. The planar array ECT is able to detect the water level and multiple water samples. However, in the last two sets of results (experiments 7 and 8), reconstructed results went closer and attached together in depth direction because of the planar array's one-sided working process issue. Shown in sensitivity maps between neighbouring electrodes and diagonal electrodes in Figure 4-4, in the near surface region, neighbouring electrodes contribute the majority of changes in capacitance and signal and hence, it is sensitive in a wide region near the sensor as there are plenty of neighbouring electrodes in planar array ECT, as shown in experiment sets 1-6 in Figure 4-11. However, due to the characteristic of planar array's one-sided working issue, with the increase in depth, the neighbouring electrodes provide little useful signal changes, while those captured by diagonal electrodes become dominant. As shown in Figure 4-4(a), the sensitivity maps between diagonal electrodes are able to detect the changes in permittivity that are far away from

the sensor. However, diagonal electrodes are only sensitive to the central location. With the increase in depth, the planar array ECT sensor is less sensitive in the corner region. Therefore, the test samples are reconstructed in centre in depth direction, as shown in experiments 7 and 8 of Figure 4-11.

As far as Figure 4-12 is concerned, the bottle of water is hung up on the steel rig and is located between electrodes 6 and 7. The distance between the bottle and the sensor is varied from 1cm in steps of 1cm to the maximum depth that the planar ECT can sense.

Figure 4-12: Set-up for depth sensitivity

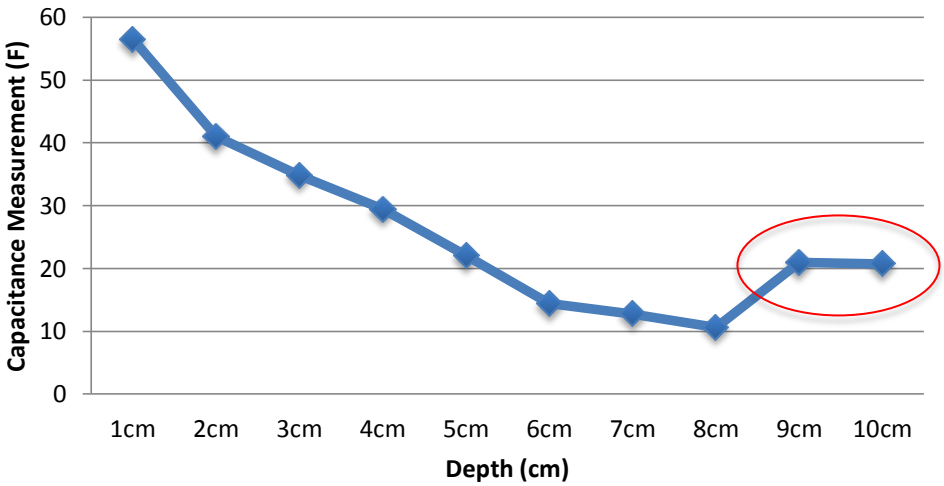

Figure 4-13: The resolution for depth sensitivity detection

Figure 4-13 shows that the capacitance measurement decreases with the changing of distance between the bottle and the planar array sensor. The change in capacitance becomes lower with increase in the distance between bottle and the sensor, which means the effect of the water on lower level of the electric field, becomes small. Hence the change in capacitance decreases. As the distance between the bottle and the sensor varying in step of 1 cm each time gradually, the volume of water in sensor region decreases linearly, and the overall equivalent permittivity of air and water ε drops linearly. The graph of the capacitance is linear in form until the distance reaches 9 cm, when the trend stops being linear. The part of irregular measurement curve after depth reaches 9 cm (marked in red circle in Figure 4-13) is predicted to be error. As at this depth, noise becomes dominant in measurement rather than change in capacitance in signal captured. In this case, similar to the result Section 4.4.3, the limitation of the ECT planar array sensor sensitivity is at also about 9 cm.

Using the rectangular tank with scale bar (marks on white bandage) attached on the outer surface of the tank, it was filled with different levels of water from 1 cm to 12 cm as shown in Figure 4-14.

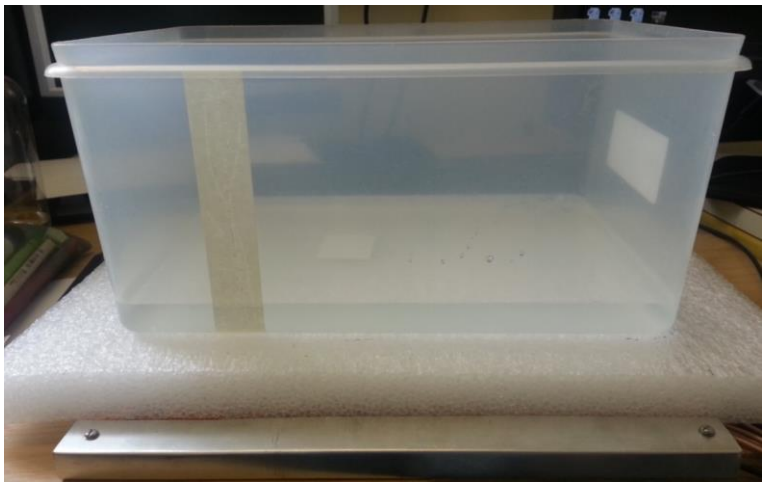

Figure 4-14: Volume sensitivity detection

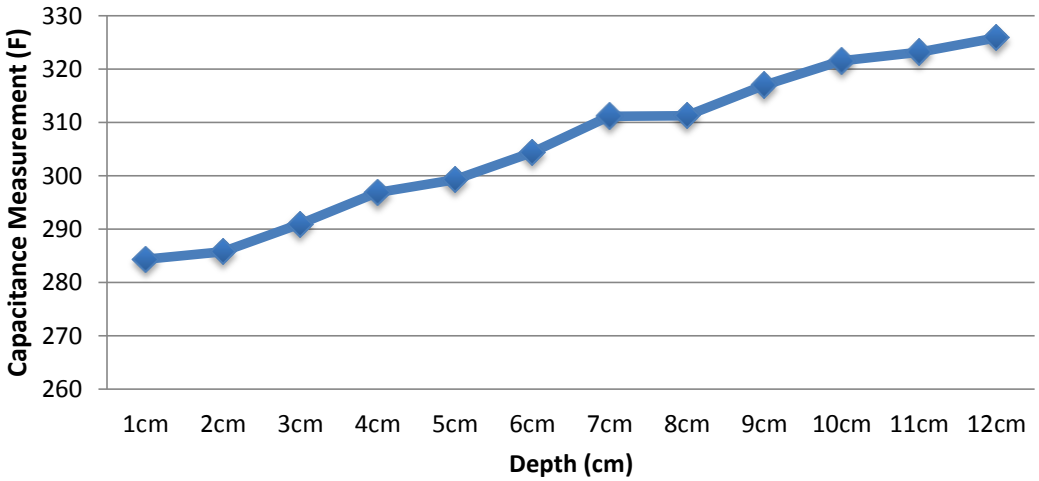

Figure 4-15: Normalised data of capacitance vs. volume with rectangular tank

Figure 4-15 shows that the capacitance measurement goes up when increasing the volume of water. The overall equivalent permittivity becomes larger when the tank is filled with more water, which results in the increase in capacitance. Since the water level increases in steps of 1cm, the volume of the water increases linearly, and the overall equivalent permittivity also increases linearly with the increasing volume of water.

4.5.2 *Dielectric material void testing*

ECT can be used in sensing dielectric materials where separated samples are placed on the planar sensor. The test material has changed to papers with large air void between the paper pads (as the large internal defects). In this section, the capacitance measurement of a full pad of paper, without out any air void (as shown in (a)), was used as the background reference data to reconstruct the air voids only instead of the paper pad itself.

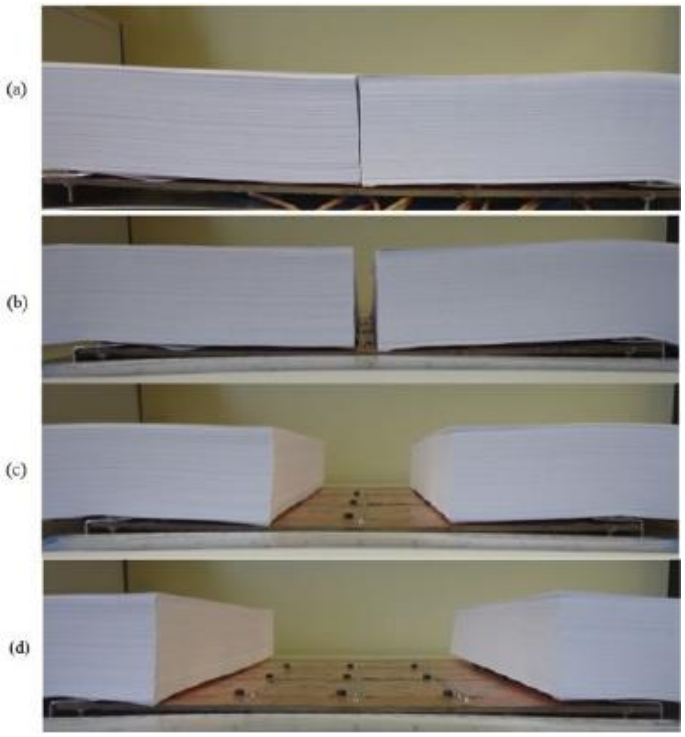

Figure 4-16: Gap detection of paper pads as test sample with a gap of (a) 1 mm, (b) 10 mm, (c) 100 mm and (d) 160 mm

The Landweber iterative algorithm was used in this series of tests. For optimum results, the reconstruction was run for different iterations using the Landweber algorithm, the closer to convergence the result (see Landweber algorithm in Chapter 2), the improved reconstructed image can be achieved. The convergence for 35, 50, and 50 iterations is plotted in Figure 4-17.

With respect to Figure 4-17, the curves of Residual error norm (A*x-b) (see. Section 2.3.6) indicates the error for solutions using different numbers of iterations. As a result, the number of iterations was reduced to 40, the results displayed in Figure 4-18 were reconstructed in 40 iterations using the Landweber algorithm with a scaling factor of 0.05. 3D iso-surface plots of reconstructed results represent the boundary between the

air and the paper. By comparing with the true images, it is noticed that the 3D results in Figure 4-18 correspond well with the widths of air gaps (shown in true images in Figure 4-18).

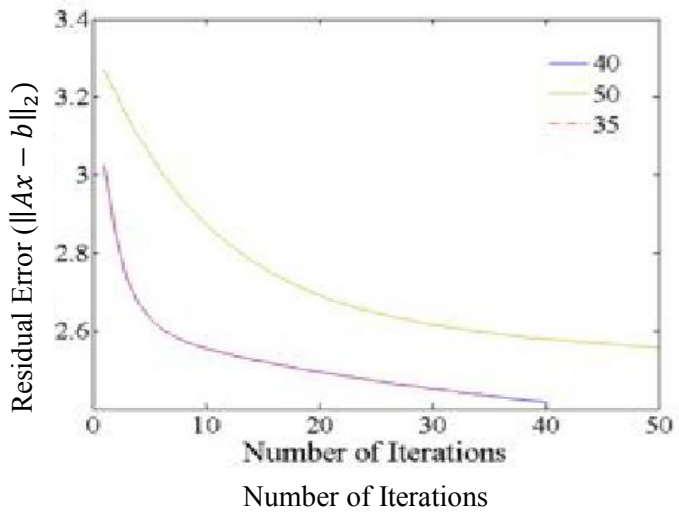

Number of Iterations

Figure 4-17: Number of iterations to convergence with the Landweber algorithm. For a scaling factor of 0.05* when the number of iterations varies from 35 to 50.

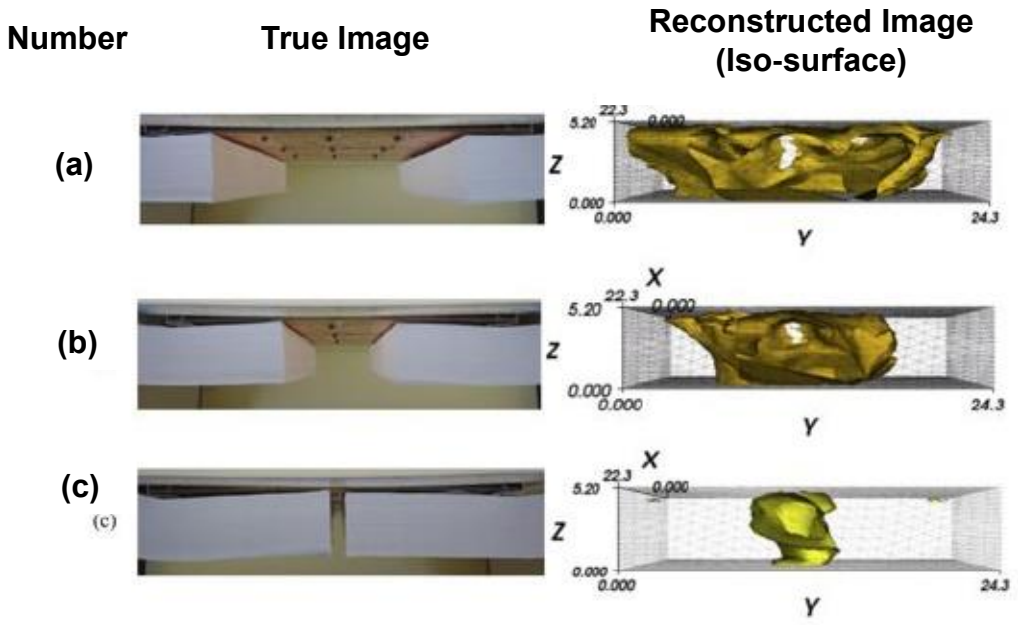

Figure 4-18: Gap of a paper sample of 50mm in depth, for gaps of (a) 160 mm, (b) 100 mm and (c) 30 mm.

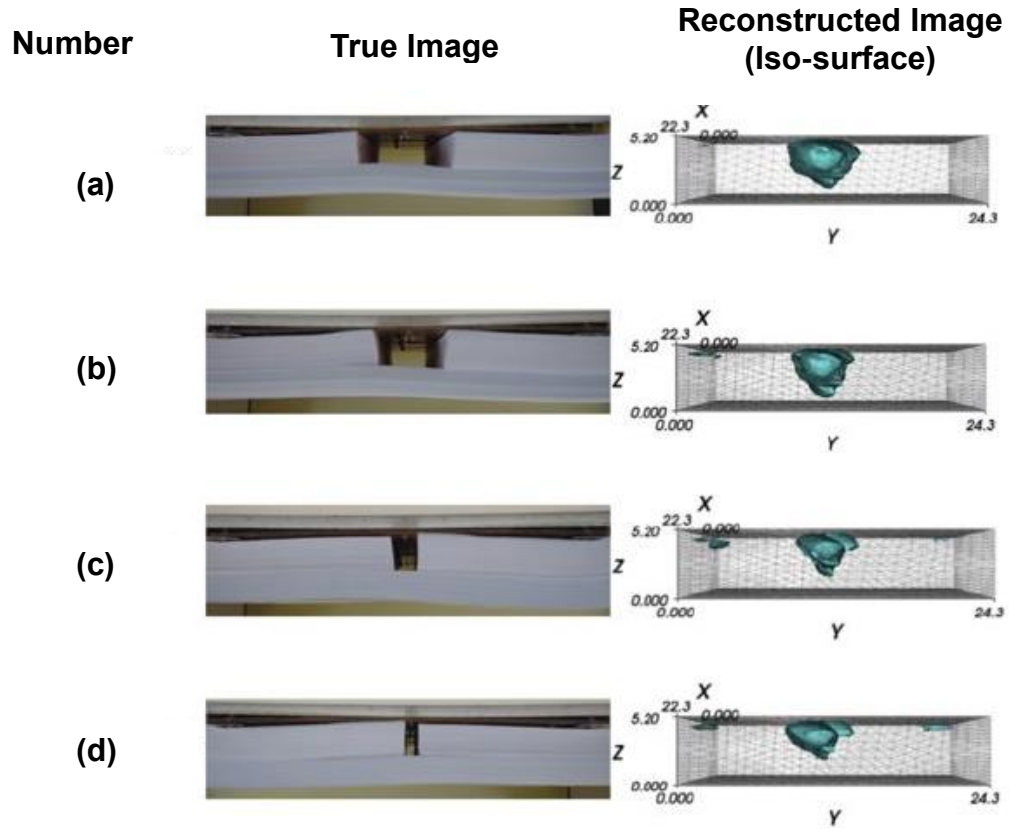

Figure 4-19: Gap of a paper sample of 30 mm in depth, for gaps of (a) 60 mm, (b) 40 mm, (c) 20 mm and (d) 10 mm.

In the primary NDE experiments shown in Figure 4-19, the depth of the gap was reduced to 30 mm. The results show that, by using a suitable parameter, the boundary between the paper and air can be reliably imaged. However, showing in experiment sets (c) and (d), the air volume are reconstructed in the same locations and sizes when the air volumes are different in true images, this potentially tells the limitation of detectable air volume size by using this planar array ECT sensor.

Figures 4-18 and 4-19 demonstrate the detection and image reconstruction of large defects in dielectric materials. With the system and sensor used in these sets of experiments, the minimum defect captured was around 20 mm.

4.5.3 *Floating metal and dielectrically material testing*

It is commonly considered that the ECT technique works only with dielectric materials, as in the previous sections, where it has been shown how planar array ECT works with dielectric materials such as wood and water. In this section, metallic samples were used to further investigate how metallic samples behave with planar array ECT, as shown in Figure 4-20.

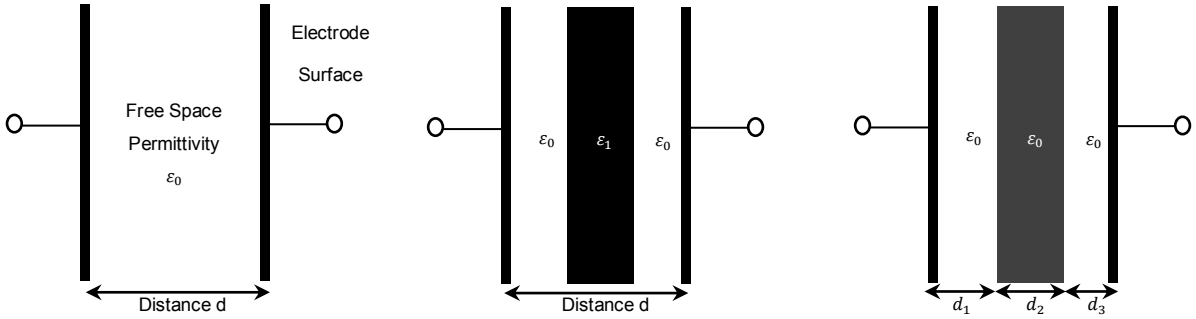

(a) Free Space Capacitance **(b) Capacitance with Media** **(c) Capacitance with Metal**

Figure 4-20: Capacitance with metallic object

It is known that the capacitance for parallel plates can be defined as:

$$c = \frac{\varepsilon_0 \varepsilon_r}{d} A \tag{4.2}$$

where c is the capacitance, ε_0 is the capacitance permittivity of air, ε_r is the relative static permittivity, and A and d are the surface area and the distance between electrodes, respectively.

Figure 4-20 (a) gives an example of a capacitance measurement for free space. In this situation:

$$C_a = \frac{\varepsilon_0}{d} A \tag{4.3}$$

Figure 4-20 (b) indicates the process of traditional ECT and, in this case, the capacitance has changed because the permittivity has changed. However, for metal

samples, which are conductive, charge would be gathered on both sides of the sample, as shown in Figure 4-20 (c). This is equivalent to changing the distance between two electrodes, which results in a change in capacitance measurement. In another words, metal samples can also result in capacitance changes, for which, they are detectable theoretically.

To further investigate the working preference of metals and the 3D planar array ECT system, the following experiments were carried out. To initially investigate and compare the performance of metallic material and dielectric material, as shown in Figure 4-21.

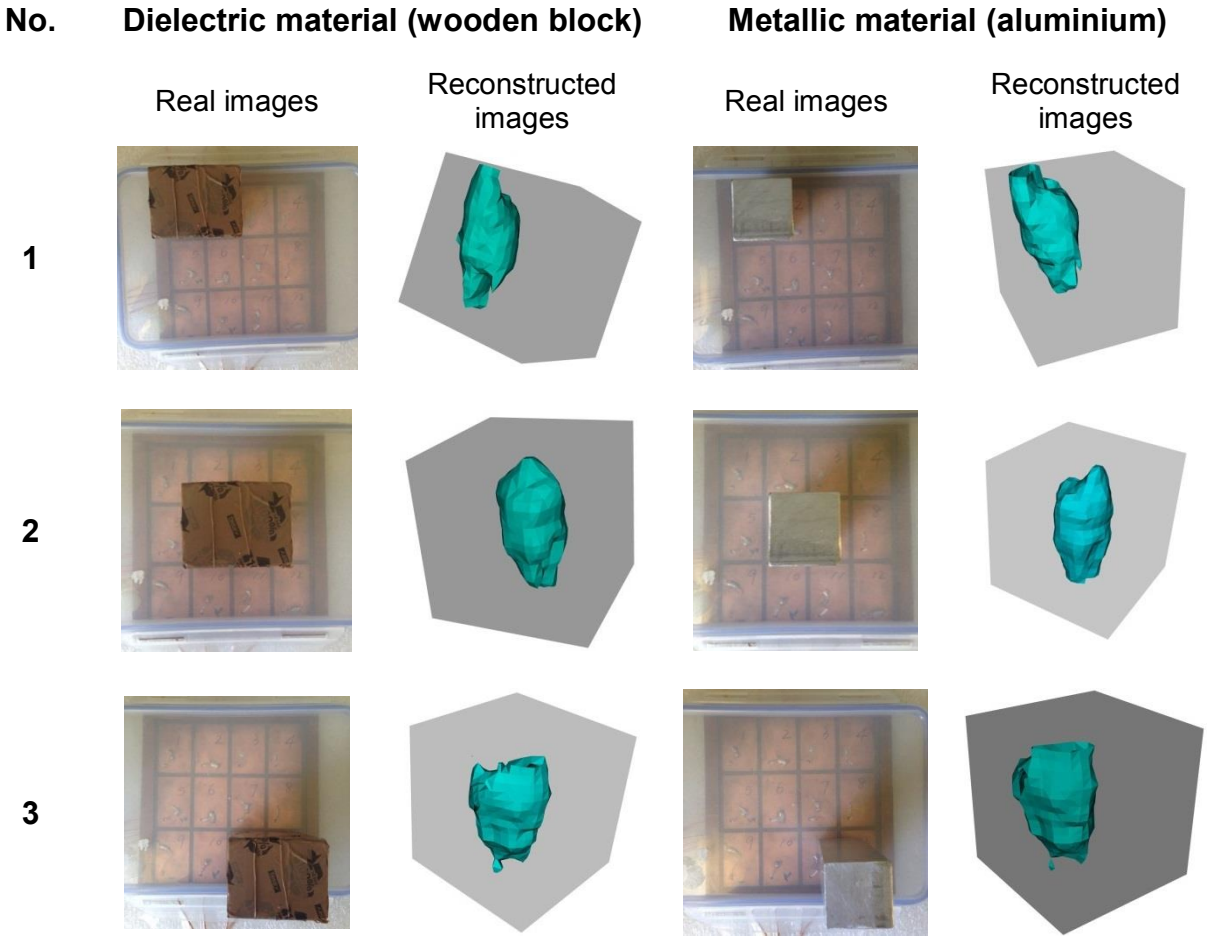

Figure 4-21: Single object testing

As far as Figure 4-21 is concerned, both a wooden block and a metallic block were tested individually in the near surface region using the planar array ECT sensor, to compare the results achieved with both dielectric and metallic material. Two test samples of different materials were placed in different locations. The results show that the metallic sample can be detected using the planar array ECT sensor. Metallic material can also cause changes in capacitance with a planar ECT system in the near surface region. However, different from dielectric material, due to the conductivity of metallic material, it can cause the invisibility issue beyond the metallic sample in a certain region due to the shield effect that is observed with metallic samples.

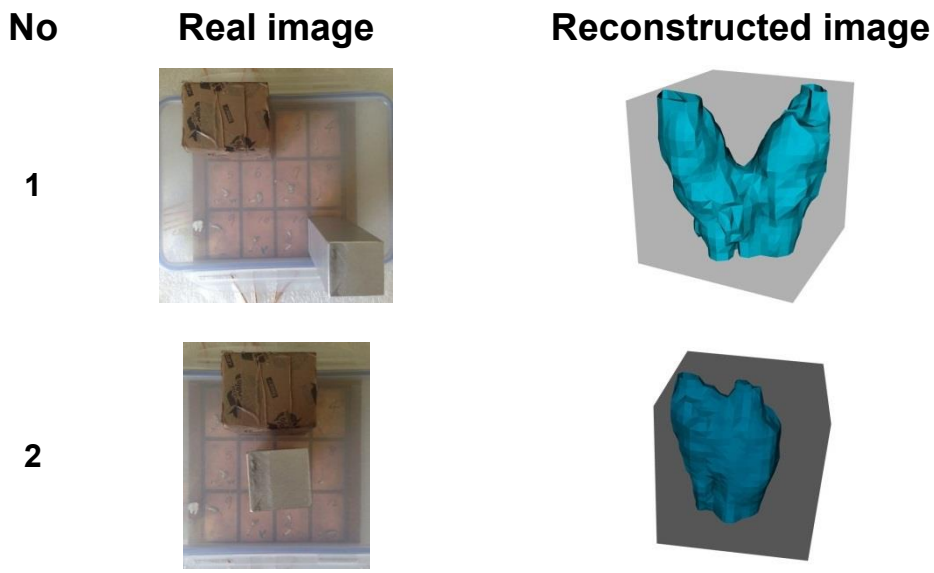

Figure 4-22: Multiple objects testing

With respect to the results shown in Figure 4-21, further experiments were carried out to further test the metallic sample performance with ECT, as shown in Figure 4-22. In this set of experiments, both the wooden block and the metallic block were tested at the same time using a 3D planar array sensor. The results of these multiple object

tests further proved that the ECT technique does work with metallic objects, as shown at the beginning of this sub-section. When two samples were placed in different locations, the reconstructed results were able to show each individual sample (as shown in experiment 1 in Figure 4-22). However, once the samples were placed too close (as shown in experiment 2 in Figure 4-22), the resulting reconstructed objects were visualised in one piece in the reconstructed image. Even though metallic material is detectable using ECT planar array system, it is hard to define from the results whether the sample is an electrical conductor or a dielectric material.

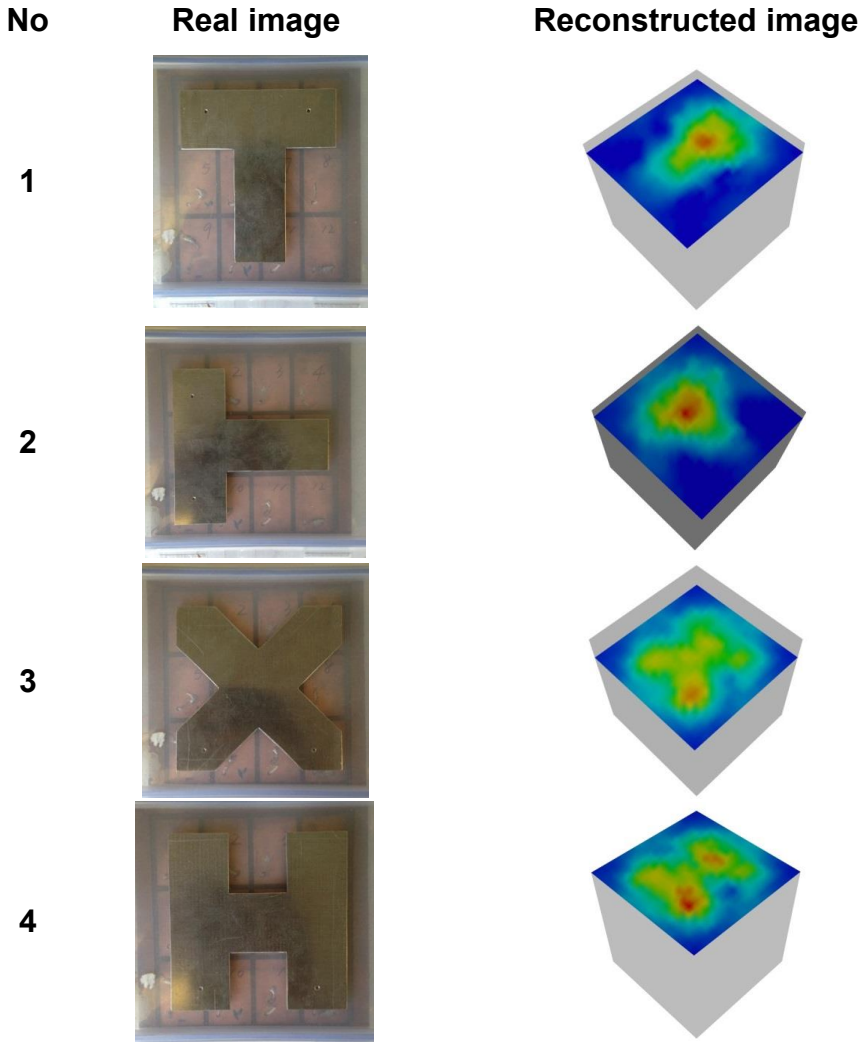

Figure 4-23: Complicated geometric objects testing

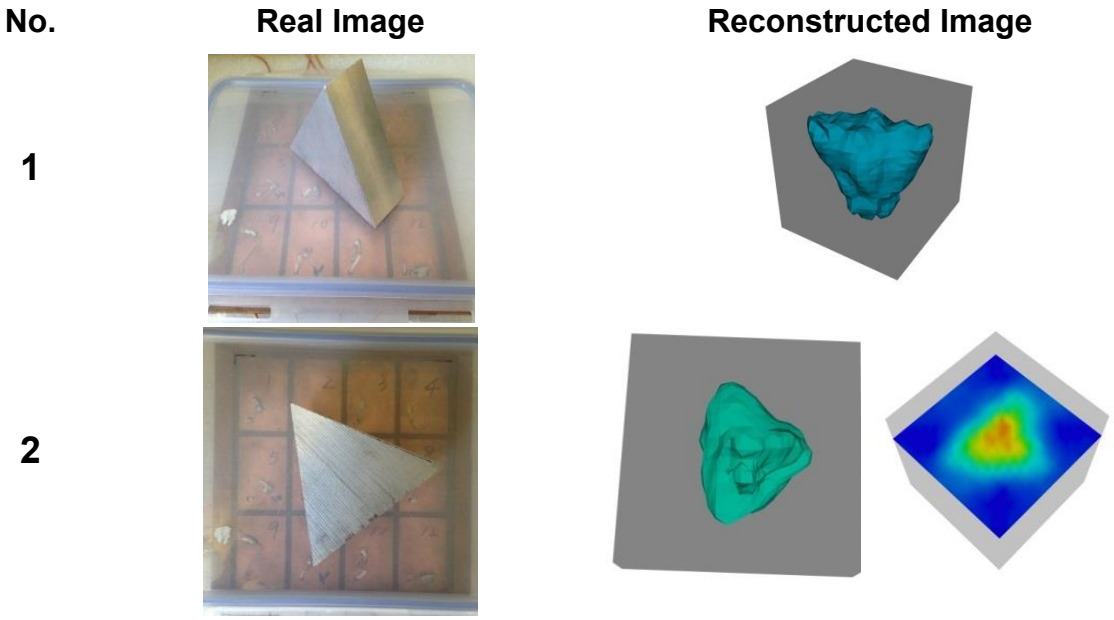

Figure 4-24: Depth testing of metallic object

Having been proven that metallic material works with the planar array ECT system in a similar way to that of a dielectric material, further tests were carried out as shown in figures 4-23 and 4-24. As far as Figure 4-23 is concerned, several metallic samples with different complicated geometries were tested in the near surface region, as shown in real images. In the reconstructed results, different geometries of the test samples are detected and reconstructed. It can be seen that, the metallic sample works well in both x and y directions with 3D planar array ECT sensor in the near surface area. In Figure 4-24, a triangular metallic sample was placed vertically (experiment 1 in Figure 4-24) and horizontally (experiment 2 in Figure 4-25) on the 3D planar array ECT sensor. According to results achieved from experiments 1 and 2, the triangular metallic sample was detected well in the near sensor region but not as well in the depth direction compared to the previous experiments.

However, different from dielectric material, the metal affects the signal due to the conduction characteristic of the metal. Metallic material can produce similar results to dielectric material in ECT. However, different from dielectric material, the metal can bring a shielding effect, which will change the electric field and result in invisibility beyond the metallic material in a certain range.

4.6 Summary

The capability and feasibility of a planar ECT system has been demonstrated in 3D. This type of electrode geometry makes imaging of the near sub-surface possible. The approach is a challenging imaging setup since the access to the targeted object is limited to one surface only. Furthermore, it is demonstrated that planar ECT is capable of detecting an object at the sub-surface. The experimental results show that, although the in-depth detection using planar ECT is limited to 53% of the sensor array length, the accuracy decreased as the distance between the sample and the sensor increased. Planar array ECT performs well in central locations than edge locations. Because an object in the centre is closer to more neighbouring electrodes, which then provide good quality measured signals. The planar ECT has potential to be used as a sub-surface imaging tool in applications where a traditional circular ECT electrode array is inappropriate.

Experimental results shown in this chapter are based on isolated dielectric samples, which are used to characterise the proposed planar ECT system.

CHAPTER 5 Full 3D ECT

In the majority of ECT applications there is only limited access to the targeted objects, making conventional circular array ECT impractical. However, with limited access testing the resolution is rather lower than for the traditional ECT technique. To improve the resolution, a clear understanding of the cause for lower resolution with the associated missing information is necessary. In this chapter, a cubic full 3D planar array ECT system is implemented to understand how image quality varies with different amounts of missing information by testing different numbers of sensor planes leading to a further understanding of planar array ECT.

5.1 Introduction to full 3D ECT

In 3D ECT, full access means access to all sides of the object [46, 79], so the term full 3D is used where the electrodes surround all sides of the objects. In the past few years there has also been growing interest in planar array ECT for several new application areas [38, 57, 58, 59, 60, 62, 81]. Limited access tomography is of great importance when there is limited access to the materials being tested. Consequently, the number of measurements that can be collected from materials being tested is comparatively small. This will further result in a loss in quality of the images that can be reconstructed. This chapter aims to investigate the effect of missing data on ECT image reconstruction. To reconstruct the whole process from a full access ECT

problem to a very limited ECT problem, a cubical ECT model is developed for 3D ECT imaging, while the amount of missing information is controlled by removing planes of sensor and is evaluated quantitatively. The image quality of the reconstructed results is analysed quantitatively using theoretical models, such as resolution (see Section 5.6.2) and SVD [20, 21, 22]. ECT imaging is fundamentally a 3D imaging problem. In the following section, the design of full 3D ECT will be presented in the very beginning, and the effect of missing data test will be explained afterwards. A full 3D ECT sensor model was previously proposed in [46, 79], by using a similar ECT sensor to this but analysed in a different way. This chapter verifies full 3D ECT using experimental data and analyses the image quality with different amounts of missing information (achieved by removing electrode planes in turn) to analyse the effect of missing data in limited access tomography.

5.2 Sensor and system description

A full 3D ECT sensor was built consisting of six planar ECT planes. On each plane there are four electrodes in 2 x 2 arrangement (as shown in Figure 5-1(b)), which were constructed using conductive copper tape at the outer surface to ground the outer surface, as shown in Figure 5-1. Each plane has a surface of 10 cm x 10 cm and 4 mm in thickness. The dimension of electrode array is 3.5 cm x 3.5 cm and between the electrodes and the surrounding area of the sensor array are grounded conductors. On the back side of the sensor array, a metallic shield was used to partly shield the planar array from external interference. The measurement of capacitance data was carried out by using the ITS M3C, as shown in Figure 5-1 (a), where 24 channel capacitance

measurements are possible with frequency of 1 MHz, based on a system, which allows capacitance values down to 0.01pF to be resolved. The measurement accuracy in this unit is not as good as other typical ECT systems such as the one used in Chapter 4.

(a) ECT 3D measurement system

(b) Electrode arrangement of one plane

(c) Inside view of full 3D ECT system

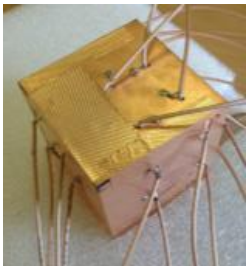

(d) Full 3D ECT sensor

Figure 5-1: 3D full 3D ECT system: (a) ECT 3D measurement system (b) Electrode arrangement of one plane of full 3D ECT system s in the array (c) Inside view of full 3D ECT system (d) Full 3D ECT sensor

5.3 Computational modelling

Figure 5-2 shows both the sensor model and the meshed model are generated by Netgen [54] using the same geometry as the experimental sensor. The number of elements in this meshed model is 81834**.** By solving the forward model it is possible to evaluate the capacitance data, which then can be used in the inverse problem.

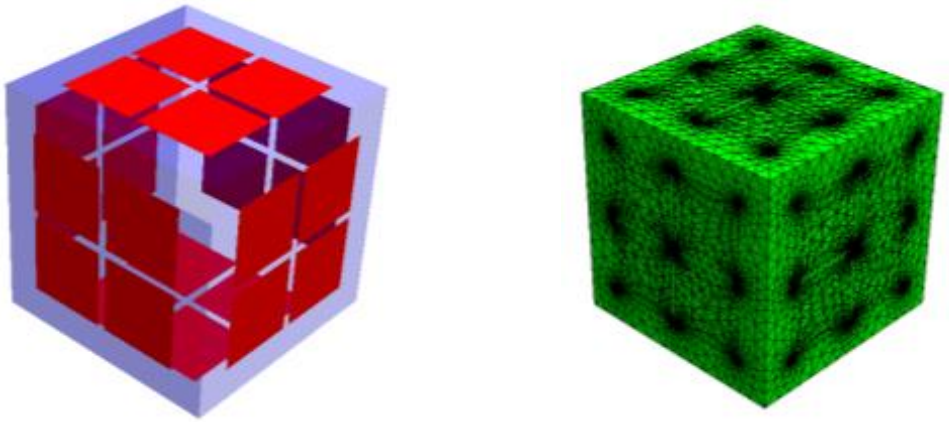

(a) (b)

Figure 5-2: (a) Computer model of full 3D ECT Sensor (b) Meshed model for full 3D ECT system

The proposed sensor has 24 electrodes hence there are 276 possible measurements. The relationship between measured capacitance and the permittivity of each voxel is non-linear. In this chapter, the standard linear Tikhonov algorithm is used. Therefore, the Jacobian matrix is not updated during the whole process. As explained in Section 2.2.2, each row of the Jacobian matrix (selectivity map) represents the sensitivity of one measurement data with respect to all voxels. The sensitivity map indicates the relationship between capacitance and the permittivity of each combination of electrodes. [1, 8] The sensitivity map can be calculated using an efficient formulation based on calculated fields from excitation and sensing electrodes [7].

By solving the forward problem in this ECT process, three of 276 the sensitivity maps of this full 3D ECT system with full access (no plane was removed) are presented in Figure 5-3.

(a) Neighbouring plane **(b) Opposite plane** **(c) Opposite plane and diagonal electrodes**

Figure 5-3: Sensitivity between certain electrodes: (a) Neighbouring planes (b) and (c) Opposite planes

The Tikhonov based method is commonly used to solve the inverse problem in ECT [3, 59]. The main task of image reconstruction in ECT is to determine the permittivity distribution from the measured capacitance. In the discrete form, it is necessary to find the unknown $\Delta\varepsilon$ from the known ΔC, while J acts as a constant coefficient matrix in linear image reconstruction cases. In this study, an iterative reconstruction method called Tikhonov method was used [59] (see Section 2.3.4, equation 2.27). As stated in equation 2.27, the diagonal elements of Hessian matrix (J^TJ), where J^T is the transpose of the Jacobian matrix, are used as the regularisation term. The parameter is chosen empirically as 0.01 for a full tomography data set, the regularisation parameter was reduced gradually for limited access data. To accomplish the analysis by removing the electrode plane, the regularisation parameter α for different number of removed electrode planes was reduced systematically by a rate which the $||\Delta C||_2$ changed.

5.4 Experimental results

In this section, experimental results will be presented using a full 3D ECT sensor to analyse how the image quality varies with different amount of information available. This is achieved by removing the electrode planes to reduce the number of working electrodes and increase the amount of missing information collected by ECT. When the electrode planes are removed, corresponding measurement data is systematically removed from full measurement data to represent the latest status full 3D ECT with different numbers of missing planes.

5.4.1 *Full 3D experiments:*

Several experiments were carried out using the full 3D sensor, including single and multiple inclusions. Figure 5-4 shows image reconstruction results for full 3D experimental data when a cylindrical rubber cork, 2.5 cm diameter and 3.0 cm height, is moving inside the cubic sensor area from the top front corner to the bottom back corner. Both the true images and the reconstructed images are listed. Figure 5-5 shows reconstruction of multiple inclusions. In (a), two corks were used in the diagonal direction as shown in the true image; the full 3D sensor was able to detect the location and the result is shown in the reconstructed result (a). Experiments (b) and (c) show reconstructions of the full 3D ECT used as a level detector, where 20% and 60% of cube was filled with polymer beads, respectively. The reconstruction results are shown in Figures 5-5 (b) and (c).

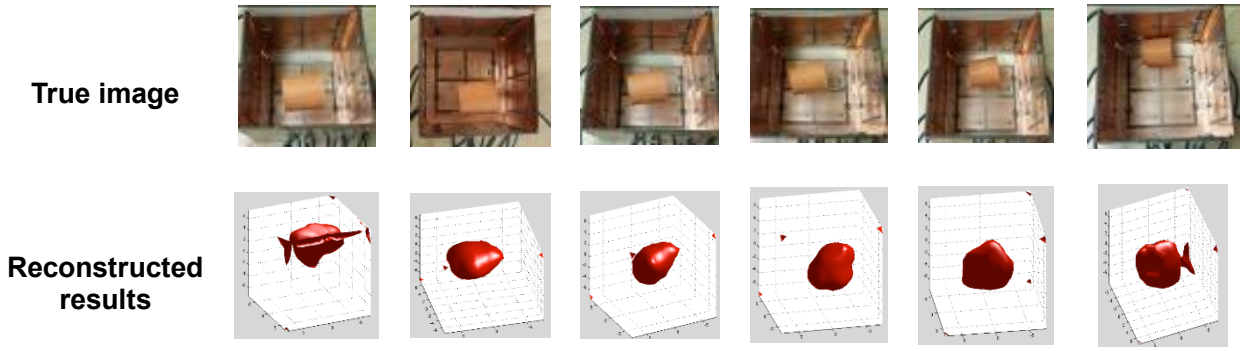

Figure 5-4: Sample and full 3D reconstruction of a moving rubber cork

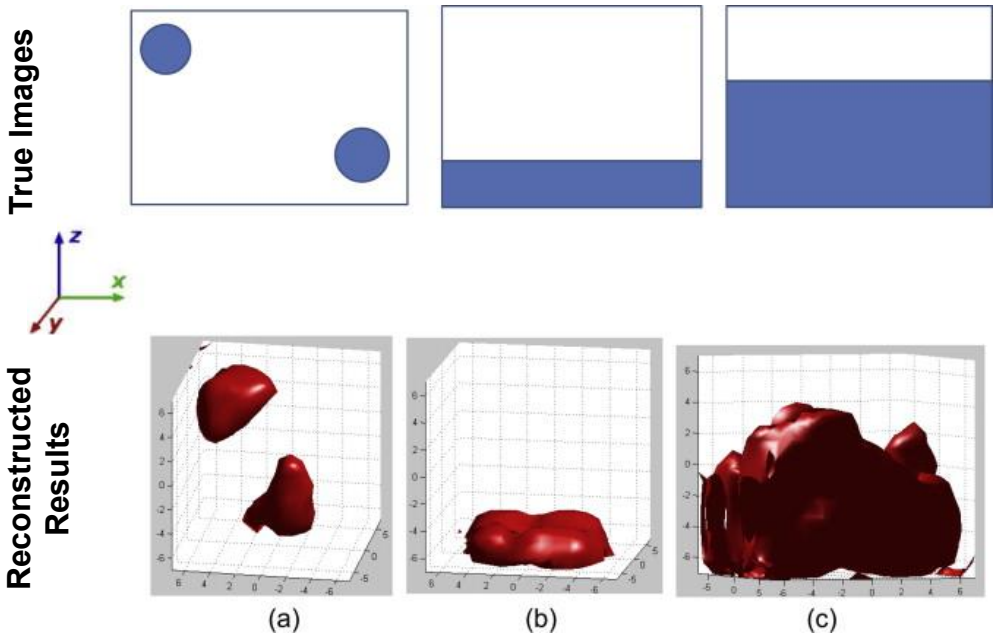

Figure 5-5: (a) Reconstruction of multiple inclusions, (b) level detection using full 3D ECT (20% filled), (c) level detection using full 3D ECT (60% filled),

5.5 Limited access 3D ECT

To analyse the effect of different amounts of missing information, five electrode planes were removed from the sensor one by one. Meanwhile, corresponding elements in capacitance measurement achieved from the full 3D ECT sensor were removed together with the electrode planes, to make limited access tomography. Figure 5-6

shows the guidance of missing sides for limited access tomography using this full 3D ECT system. The outer shield is assumed to remain in all missing data scenarios. This may not be possible in realistic limited access ECT cases.

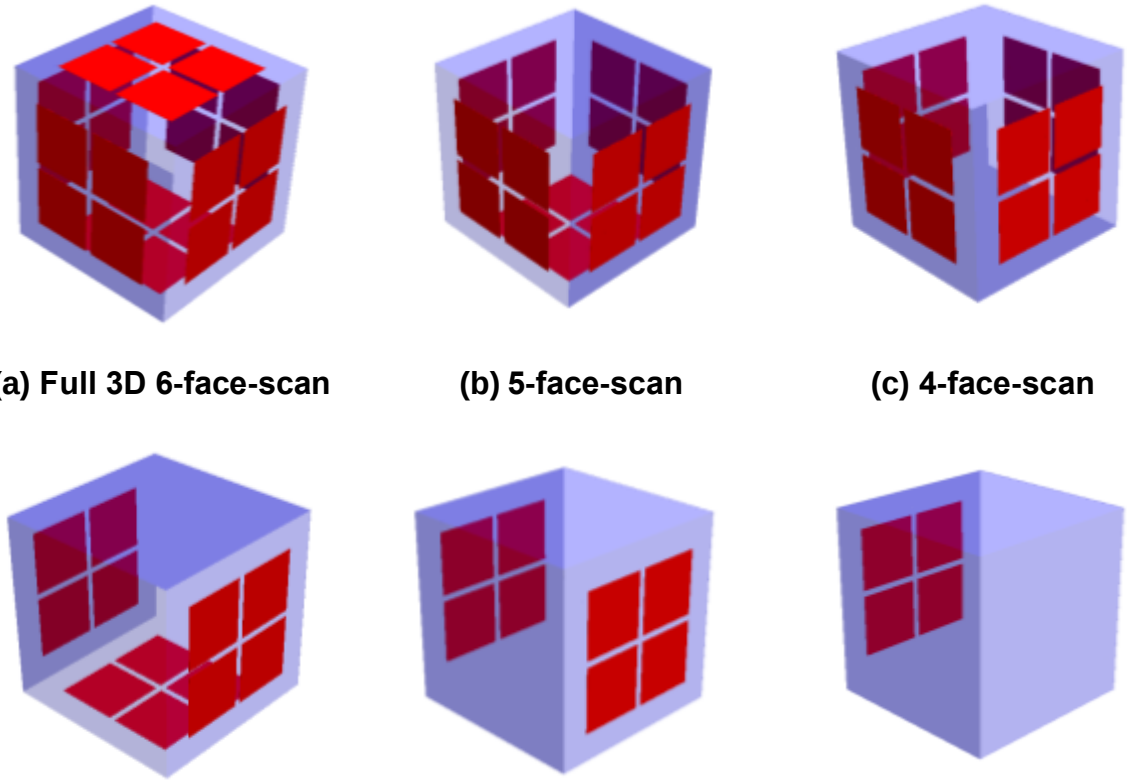

(a) Full 3D 6-face-scan **(b) 5-face-scan** **(c) 4-face-scan**

(d) 3-face-scan **(e) 2-face-scan** **(f) 1-face-scan**

Figure 5-6: full 3D scan and missing sides scan guide

The results of image reconstruction are shown in Figure 5-6 for a rubber cork located in centre of the imaging region. The experimental results are presented for reconstructed results with a missing side from the full 3D ECT system. As shown in Figure 5-7, image reconstruction of a cork in the central imaging area was accomplished. The central area is selected as it is not biased towards any plane. It is important that image degradation results when more than three sides are missing and this should be considered in the context of the low number of electrodes in this study.

In Figure 5-7, with an increasing number of missing electrode planes (from (b) to (g)) image quality went down gradually and was almost undetected in (g), in which only one electrode plane (4 electrodes, 6 measurements) was working. The image quality degradation will be further quantified and evaluated in the next section.

(a)

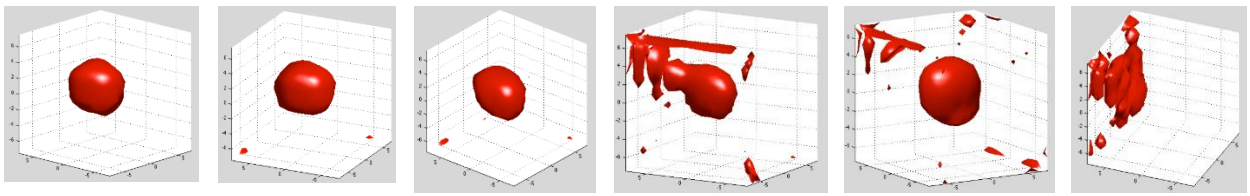

(b) **(c)** **(d)** **(e)** **(f)** **(g)**

Figure 5-7: Image reconstruction results for an object in the centre with missing sides. (a) Rubber cork in centre, (b) no missing data with 24 electrodes remaining, (c) one side is missing with 20 electrodes remaining, (d)two sides are missing with 16 electrodes remaining, (e) three sides are missing with 12 electrodes remaining, (f) four sides are missing with 8 electrodes remaining, and (g) five sides are missing.

5.6 Resolution analyses

To verify the effect of missing sides, three approaches have been adopted. The first one relies on SVD of the Jacobian matrix and monitoring the trend of singular value decay in different missing data scenarios [21]. The second method is based on analysis of the resolution [79], which provides an indication for uniformity of overall sensitivity in

different areas of interest for imaging. The third method is based on image quality analysis from actual reconstructed images [79].

5.6.1 *Singular value decomposition*

As explained in Chapter 2, SVD of the Jacobian matrix provides an important tool to analyse the behaviour of the underlying inverse problem [21]. SVD of the Jacobian matrix in the ECT system shows the potential advantages that the system is able to provide. In these ill-posed problems, ECT requires regularisation. The amount of information that can be extracted from the imaging problem depends on the number of singular values that are above the noise level. Based on the Picard criteria [20, 22], only the singular values above the noise level will contribute to the results.

Figure 5-8 shows singular value decay for full 3D and different numbers of missing sides. It can be seen that, by increasing the number of missing sides, the slope of the singular value shows a more rapid drop, showing more severity of the ill-posedness of the inverse problem. With respect to Figure 5-8, it can be seen that the full 3D ECT with all electrodes working (blue line) has a larger number of singular values above the noise comparing to the missing sides. Similar to Figure 3-4 in previous chapter, noise analysis can be done to evaluate the number of useful singular values depending on measurement noise (and modelling error) in the ECT system. In this figure, the blue line is plotted with 24 electrodes working (276 measurements), while the purple line is plotted with 4 electrodes working (6 measurements). It can been seen that the slope of the singular value shows a more rapid drop by increasing the number of electrodes removed; this suggests the severity of the ill-possedness of the inverse problem.

Hence, the inverse problem becomes more ill-posed with the increase in the number of missing information.

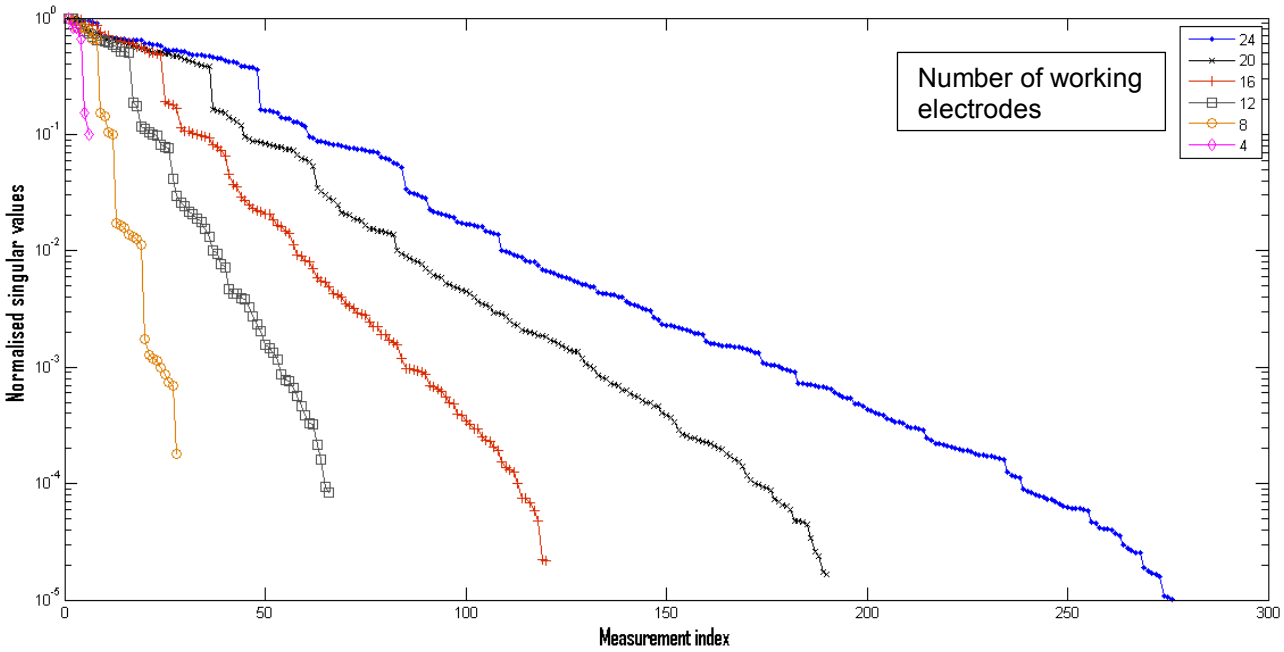

Figure 5-8: Singular value plot for full data and missing sides

5.6.2 *Resolution matrix method:*

The reliability of the inverted result could be very limited based on the amount of missing information, especially for zones where data are totally missing. To compare the quality of reconstructed results in a quantified way, the resolution, which identifies where the inversion has a good reliability and where it does not, is used in this chapter.

From the previous chapter, taking equation $\Delta C = J\Delta\varepsilon_{true}$ and substituting into the Tikhonov equation (Equation 2.27), the definition of the model resolution matrix R_m in this case can be obtained:

$$R_m = (J^T J + \alpha R)^{-1} J^T J \tag{5.1}$$

In the ideal scenario, the resolution matrix R_m will be the identity matrix. Figures 5-9 (a) and (b) show plots of diagonal values of the matrix R_m for full data and for the case with a 3 face scan, respectively. The diagonal values are normalised against the largest values. For a 9261 x 9261 matrix in an ideal scenario the sum of diagonal values should be 9261. Due to the ill-posedness of the inverse problem, in full 3D ECT, the sum of the diagonal values of the matrix R_m is 2000 and will gradually decrease with missing sides, as shown in Figure 5-9 (c). Figure 5-8 shows that various voxels (and regions) are not detectable in the same way. The variation in detectability decreases with the number of missing sides. Figure 5-9 (a) shows that, even with full 3D access, not all areas of imaging can be reconstructed with the same accuracy. In Figure 5-4, the same parameter and the same testing object are used in full 3D ECT, but the results were different with different locations of the testing object. The diagonal elements of the R_m matrix are normalised against their largest value to make it simple to compare the level of homogeneity for reconstructed images for different amounts of missing data. The overall level of reconstruction capability can be evaluated with the absolute value of the regularisation matrix and it will depend on the regularisation parameter; however, this chapter mostly focuses on comparison of missing data.

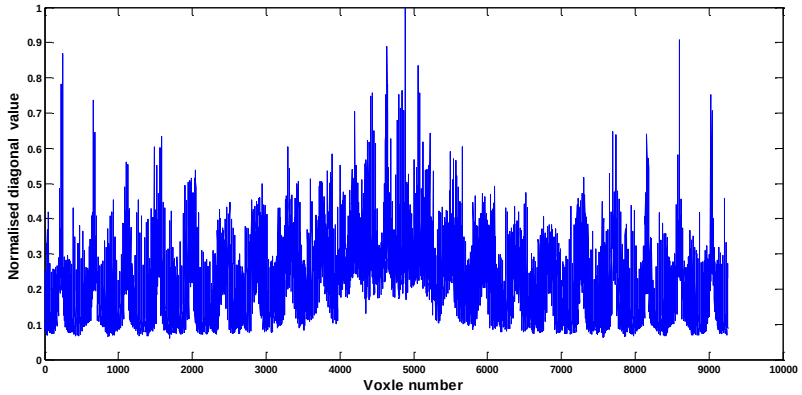

(a) Normalised diagonal value for full data

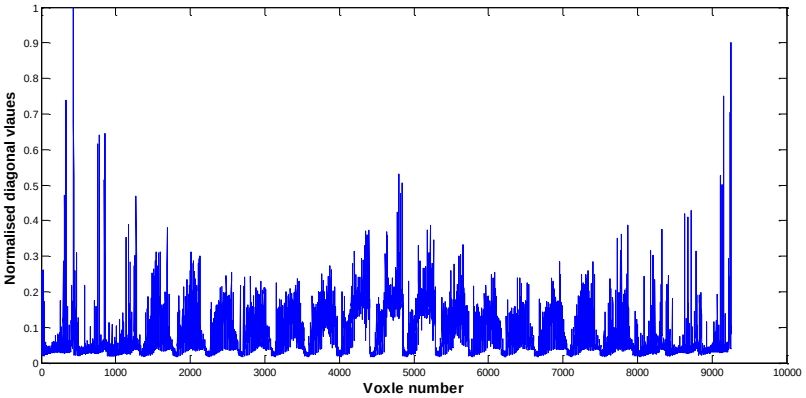

(b) Normalised diagonal value for 3 planes data

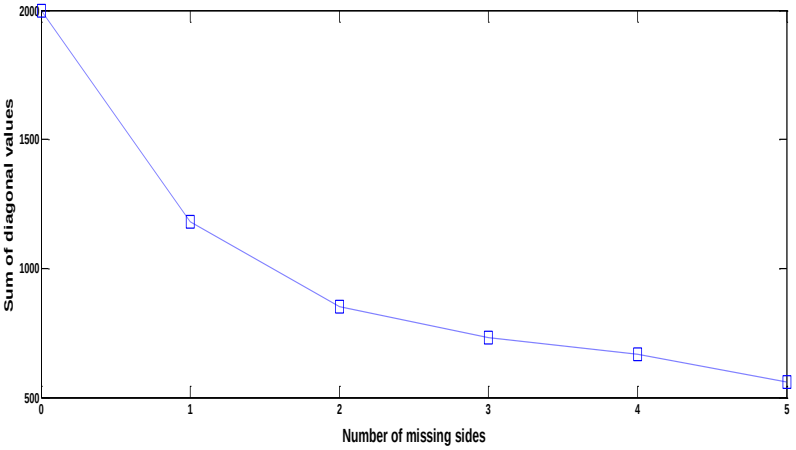

(c) sum of diagonal values against number of missing sides

Figure 5-9: Analysis of full 3D ECT with different missing planes: (a) And (b) Normalised diagonal value of the resolution for full data and 3 face scan, (c) sum of diagonal values against number of missing sides

5.6.3 *Image quality measures:*

Resolution (RES) measures the size of reconstructed targets as a fraction of the medium. There is wide variety of image quality parameters that could be used for analysis in this section. RES was selected for simplicity and also to show consistency with the resolution analysis, so was SVD. In [46] a shape deformation measure has been used for image quality, which could be used for this study.

Theoretical indication of resolution loss can be verified by analysing the reconstructed images from experimental data from full and missing data sets. Several image quality measures were presented in [146], such as resolution (RES), positioning error (PE) and ringing effect (RNG). Image resolution, which is calculated using the equations defined in [146], measures the ratio of voxel numbers in inclusions (in the case of the experiments in this chapter, the wooden sample) to the total voxel numbers [146]. The total voxel numbers represent the volume of the region of interest for imaging. It can be defined as stated in Section 4.3 (Equation 4.1). The RES value is then normalised against the full data set so that the relative resolution loss can be presented from the range 0 to 1. Figure 5-10 shows the image resolution values RES normalised against the resolution value for full access ECT data, which shows image quality degradation by missing sides.

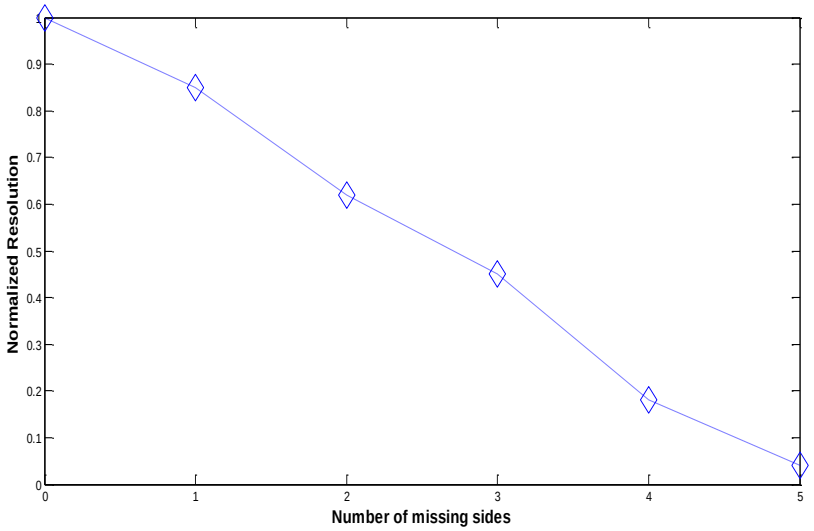

Figure 5-10: Resolution values for reconstructed images of Figure 5-5

With respect to the result, it can be seen that the quality of the image varies significantly with different levels of missing data. Furthermore, various analysis methods were used to confirm the conclusion. It can be seen that with the increase in the number of missing information, the slope of the normalised resolution drops rapidly. In other words, with more missing information (by removing more electrode planes), the severity of the ill-posed condition of the inverse problem becomes worse. This is the same as shown in Figure 5-8. For a given noise level in a measurement system, the full 3D ECT has a larger number of singular values above the noise with full access to the sample compared to the missing sides. Shown in Figure 5-10, the resolution values drop sharply with an increasing amount of missing information. It is important that the results of this chapter are solely level on missing sides. The number of electrodes in each side remains constant so does the distance between electrode sides. Some of these resolution losses may be recoverable by adding electrodes on available sides and also by adjusting the distance from the object. Image analysis is

carried out for an inclusion in the central area of the imaging region to keep the comparisons meaningful for missing sides.

5.7 Summary

In this chapter a full 3D ECT sensor was developed and a series of experiments were carried out to analyse how image quality varies with different amounts of missing information. Quantitative image quality measures and theoretical tools are used to quantify the effect of missing sides. An analysing tool has been provided, which makes it possible to evaluate the effect of missing sides in each imaging scenario, or in other words, the effect of adding sides. More evaluations can be carried out in future studies with a large number of electrodes, for example 96 electrodes allowing more scenarios. However, with the increase in the number of electrodes, more information can be achieved, but this could result in reduction surface area of the electrodes hence the change in measurement signal. Future studies could include varying the number and shape of electrodes in each side and allowing change of distances between various sides.

CHAPTER 6 Conclusions and Future Work

6.1 Conclusions

The thesis aims at development of the ECT for possible NDE application and evaluation of its limitations and challenges. This is extremely challenging, but the aim of this thesis was to develop the fundamental tools needed to move the ECT towards this direction. This thesis began by development of several ECT sensor fabrications in wide variety of geometries and associated modelling work. Several ECT sensors have been built and tested. A good understanding of ECT algorithms and the ECT forward modelling have been developed. Modelling skills are gained for mesh generation for a variety of imaging geometries. These are presented in Section 2.2. It was always challenging to validate an ECT forward model against experimental data. A statistical method enabling evaluation of error between current model and a perfect scenario have been implemented. AEM was developed to account for a model imperfection in 3D ECT. AEM theory has been used to present study of 2D ECT in this thesis.

The capability and feasibility of a planar ECT system has been demonstrated in 3D. This type of electrode geometry makes imaging of the near sub-surface possible. The approach is a challenging imaging setup since the access to the targeted object is limited to one surface only. Furthermore, it is verified that planar ECT is capable of

detecting the object in the sub-surface. The experimental results show that although the in-depth detection using planar ECT is limited up to 50% of length of sensor array, but the accuracy goes down, as the sample is getting further away from the planar array sensor. Because objects located in the central area of sensor array are able to be detected and reconstructed in higher quality than the objects at the edge of electrode array. According to the sensitivity map plotted in Figure 4-4, different from traditional ECT system, planar array ECT is more sensitive in the centre of near sensor region than near the edge region. In depth direction, objects reconstructed were moving toward the central area with increasing depth. Because the change in signals mostly captured by the diagonal electrodes in depth direction. The capacitance difference between diagonal electrodes becomes dominant while capacitance measurement from neighbouring electrodes provides little information in depth direction. The problem with this is that the diagonal electrodes are only sensitive in the central area in depth detection, as shown in Figure 4-4

Planar ECT has potential to be used as a sub-surface imaging tool in application where a circular ECT electrode array is inappropriate. The sub-surface imaging technique works well with dielectric material in a certain depth. Metallic material works with this technique as well. However, due to the conductive characteristic of metallic material, invisibility issue exists beyond the metallic material at a close range. For void detection using planar array ECT, experimental results are based on isolated dielectric samples, which are used to characterise the proposed planar ECT system.

A full 3D sensor was developed and a series of experiments were carried out to analyse how image quality varies with different amount of missing information.

Quantitative image quality measures and theoretical tools are used to quantify the effect of missing sides. It has provided an analysing tool, which makes it possible to evaluate the effect of missing side in each imaging scenario or the effect of adding sides. More evaluations can be carried out in future with a large number of electrodes for example 96 electrodes allowing more scenarios. These results further explained the behaviour of the planar array ECT system. Limited access ECT always has the challenge of lacking in achieving full information, the full 3D system and the validation results gives direction of improvement of 3D planar array ECT.

6.2 Future work

More work to be done in design aspect of planar ECT array so that it makes it a suitable NDE sensor array. This needs to be done in NDE requirement and in context of individual applications. For the application of these results further investigation is required to bring the work to a suitable level, at which it can be incorporated into a suitable system. To achieve this there are several points to focus on for each sensor array.

According to the demonstration of both planar array ECT and full 3D ECT, the potential application of planar array has been shown clearly while full 3D ECT provides addition knowledge to understand how planar array ECT works and the reason of limitation of planar array ECT. To increase the resolution of the planar array is of prime importance for furthering the field of subsurface 3D imaging for limited access imaging. An investigation into improvement in 3D image reconstruction software is needed to

improve the imaging speed and the resolution. Hidden defects within the paper pad can be created and tested as demonstrated in Chapter 5.6.2.

Both sensor improvement and sensor design are worth studying in future. An in depth investigation into how the size of electrodes and the capacitive signal are measured, particularly for the planar sensor array, is needed. Following the identification of the ideal sensor size for application automatic threshold should be included to increase the rate, at which the results can be completed and analysed to provide relevant information.

The non-uninform sensitivity maps of planar array ECT system in depth direction, needs to be studied in future. The sensitivity map of an ECT system indicates the image reconstruction ability of the system. The system performance of the 3D planar array ECT system in the near surface region is achieved from both neighbouring electrodes and diagonal electrodes. However, the depth sensitivity of the 3D planar array ECT system was significantly achieved from the diagonal electrodes and those electrodes, which are far away from each other. These electrodes are also influenced by increasing noise rather than change in signal with increasing depth. This has been mentioned in Chapter 4.4.4, for this reason, even the working depth of the planar array ECT system has been proven to be around 50% of the size of the sensor. In deep sensor region, due to the non-uniform sensitivity, multiple objects became difficult to be separated in reconstructed image. Samples in a corner region moved towards the central region in depth direction. This needs to be analysed and solved to improve the performance of the 3D planar array ECT system in future.

List of Own Publications

Journal papers:

1. Ye, Z., Banasiak, R. and Soleimani, M., *Planar array 3D electrical capacitive tomography*, Insight, 55(12), 2013, pp 675-680.

2. Dong, X., Ye, Z. and Soleimani, M., *Image reconstruction for electrical capacitance tomography by using soft-thresholding iterative method with adaptive regulation parameter*, Meas. Sci. Technol., 24(8), 2013, pp 085402.

3. Banasiak, R., Ye, Z. and Soleimani, M., *Improving three-dimensional electrical capacitance tomography imaging using approximation error model theory*, Journal of Electromagnetic Waves and Applications, 26, 2013, pp 411-421

4. Ye, Z., Wei, H.Y., Soleimani, M., *Resolution Analysis Using Fully 3D Electrical Capacitive Tomography*, Measurement, 61, 2015, pp 270-279

Conference papers:

5. Wei, H.Y., Yang, C.L., Ma, L., Ye, Z., Yao, A. and Soleimani, M., 2012. *Three-dimensional industrial process tomography using electrical and electromagnetic tomography: recent developments*, In IEEE International Instrumentation and Measurement Technology Conference, Graz, Australia, 13-16 May 2012

6. Zhang, M., Ma, L., Ye, Z., Yang, C.L., Wei, H.Y., Banasiak, R. and Soleimani, M., *Near subsurface 3D imaging using planar array : EIT, ECT, MIT*, In 7th World Congress in Industrial Process Tomography, Krakow, Poland, 2-5 Sept. 2013

7. Soleimani, M., Wei, H.Y., Banasiak, R., Ye, Z., Yang, C. L., Qiu, W., Yao, A., Ma, L., Adler, A. and Pengpen, T., *Volumetric soft field and hard field tomography: MIT, ECT, EIT, cone beam CT*, In 7th World Congress in Industrial Process Tomography, Krakow, Poland, 2-5 Sept. 2013

References

1. Williams R.A. and Beck M.S., *Process Tomography: principles, techniques and applications,* 1995, Oxford: Butterworth-Heinemann. xxv, 581 p.

2. Lu, G., Peng, L., Zhang, B. and Liao, Y., *Preconditioned Landweber iteration algorithm for electrical capacitance tomography,* Flow Meas. and Instrum., 16(2-3), 2005, pp 163-167

3. Soleimani, M. and Lionheart, W.R.B., *Nonlinear image reconstruction for electrical capacitance tomography using experimental data*, Meas. Sci. Technol., 16(10), 2005, pp 1987-1996

4. Alme, K.J. and Mylvaganam, S., *Electrical Capacitance Tomography—Sensor Models, Design, Simulations, and Experimental Verification*, IEEE Sensors J., 6(5), 2006, pp 1256-1266

5. Arridge, S.R., Kaipio, J.P., Kolehmainen, V., Schweiger, M., Somersalo, E., Tarvainen, T. and Vauhkonen, M., *Approximation errors and model reduction with an application in optical diffusion tomography*, Inverse problems, 22(1), 2006, pp 175-195

6. Yang, W.Q., *Hardware design of electrical capacitance tomography systems*, Meas. Sci. Technol., 7(3), 1996, pp 225-232

7. Soleimani, M., *Three-dimensional electrical capacitance tomography imaging,* Insight, 48(10), 2006, pp 613-617.

8. Banasiak, R., Wajman, R., Sankowski, D. and Soleimani M., *Three-dimensional nonlinear inversion of electrical capacitance tomography data using a complete sensor model*, Progress in Electromagnetics Research, 100, 2010, pp 219-234

9. Wajman, R., Banasiak, R., Mazurkiewicz, Ł., Dyakowski, T. and Sankowski, D., *Spatial imaging with 3D capacitance measurements*, Meas. Sci. Technol., 17(8), 2006, pp 2113-2118

10. Sharma, D., Goyal, S., Khanna, R. and Mukherjee, A., *Non-destructive Testing of Materials using Capacitive Sensing Technique*, MIT International Journal of Electronics and Communication Engineering, 1, 2011, pp 73-77

11. Warsito, W., Marashdeh, Q. and Fan, L.S., *Electrical capacitance volume tomography*, IEEE Sensors J., 7(4), 2007, pp 525-535

12. Tarantola, A., *Inverse problem theory and methods for model parameter estimation*, 2005, SIAM

13. Yang, W.Q. and Peng, L., *Image reconstruction algorithms for Electrical Capacitance Tomography*, Meas. Sci. Technol., 14(1), 2003, pp R1-R13

14. Diamond, G.G. and Hutchins, D.A., *A new capacitive imaging technique for NDT,* ECNDT, Berlin, 25-29 Sept. 2006.

15. Alvarez, D., Dorn, O., Irishina, N. and Moscoso, M., *Crack reconstruction using a level-set strategy,* Journal of Computational Physics, 228, 2009, pp 5710-5721

16. Li, Y. and Yang, W.Q., *Image reconstruction by nonlinear Landweber iteration for complicated distributions,* Meas. Sci. Technol., 19(9), 2008, pp 094014

17. Yang, W.Q. and York, T.A., *New AC-based capacitance tomography system*, IEE Proc., Meas. Sci. Technol., 146(1), 1999, pp 47-53.

18. Björck, A., *Numerical methods for least-squares problems*, 1996, Philadelphia: SIAM. xvii, 408 p.

19. Hanke, M., *Conjugate gradient type methods for ill-posed problems*, Pitman research notes in mathematics series, 1995, Harlow: Longman Scientific & Technical. 134 p.

20. Hansen, P.C., *The truncated SVD as a method for regularisation*, BIT Numerical Mathematics, 27(4), 1987, pp 534-553.

21. Hansen P.C., *Analysis of Discrete Ill-Posed Problems by Means of the L-Curve,* SIAM Review, 34(4), 1992, pp 561-580.

22. Hansen P.C. and O'Leary D.P., *The use of the L-curve in the regularisation of discrete HX-posed problems*, SIAM Journal on Scientific Computing.

23. Huang, S.M., Dyakowski, T., Xie, C.G., Plaskowski, A.B., Xu, L.A. and Beck, M.S., *A tomographic flow imaging system based on capacitance measurement techniques*, in Pattern Recognition, 9th International Conference, Rome, Italy, 14-17 Nov. 1988

24. Jeanmeure, L.F.C., Zimmerman, W.B.J., Dyakowski, T., Jaworski, A.J. and Davies, G.A., *An algorithm based on Perturbation Theory for Electrical Capacitance Tomography*, in Proc. 1st World Congress on Industrial process Tomography. Buxton, Greater Manchester, 14-17 April 1999

25. Zhao, J.C., Fu, W.L., Li, T.S. and Shi, W., *An image reconstruction algorithm based on a revised regularisation method for electrical capacitance tomography*, Meas. Sci. Technol., 13(4), 2002, pp 638-640

26. Liepa, V., Santosa, F. and Vogelius, M., *Crack determination from boundary measurements—Reconstruction using experimental data,* Journal of Nondestructive Evaluation, 12(3), 1993, pp 163-174

27. Li, X.B., Larson, S.D., Zyuzin, A.S. and Mamishev, A.V., *Design principles for multichannel fringing electric field sensors,* IEEE Sensors J., 6(2), 2006, pp 434-40

28. Marashdeh, Q., Fan, L.S., Du, B. and Warsito, W., *Electrical capacitance tomography - A perspective*, Industrial & Engineering Chemistry Research, 47(10), 2008, pp 3708-3719.

29. Osher, S. and Fedkiw R.P., *Level set methods and dynamic implicit surfaces*, Applied mathematical sciences, 2003, New York: Springer. xiii, 273 p.

30. Osher, S. and Sethian, J.A., *Fronts Propagating with Curvature-Dependent Speed-Algorithms Based on Hamilton-Jacobi Formulations,* Journal of Computational Physics, 79(1), 1988, pp 12-49.

31. Plaskowski, A.B., Beck, M.S., Thorn, R. and Dyakowski, T., *Imaging industrial flows: Applications of electrical process tomography*, 1995, CRC Press

32. Polydorides, N., Lionheart, W.R.B. and McCann, H., *Krylov subspace iterative techniques: On the detection of brain activity with electrical impedance tomography,* IEEE Trans. on Med. Imag., 21(6), 2002, pp 596-603.

33. Saad, Y., *Iterative methods for sparse linear systems*, 2003, Philadelphia: SIAM. 528 p.

34. Sethian, J.A., *Level set methods and fast marching methods: evolving interfaces in computational geometry, fluid mechanics, computer vision, and materials science*, 1999, Cambridge University Press

35. Soleiman,i M., *Image and shape reconstruction methods in magnetic induction and electrical impedance tomography,* PhD thesis. 2005, University of Manchester, Manchester.

36. Hu, X.H., Yang, M., Li, Y. and Yang, W.Q., *An impedance-analyser-based multi-channel imaging system and its applications,* Proc. Of IEEE International Workshop on Imaging System and techniques, Chania, Greece, 10-12 Sept. 2008.

37. Li, Y., *Key issues of 2D/3D image reconstruction in electrical tomography*, PhD thesis, 2008, University of Manchester.

38. Yin, X., Hutchins, D.A., Diamond, G.G. and Purnell, P., (2010), *Non-destructive evaluation of concrete using a capacitive imaging technique: Preliminary modeling and experiments*, Cement and Concrete Research, 40(12), 2010, pp 1734-1743

39. Warsito, W. and Fan, L.-S., *Development of 3D Electrical Capacitance Tomography based on neural Network Multi-Criterion Optimization Image Reconstruction,* 3rd World Congress on Industrial Process Tomography, Banff. Canada, 2-4 Sept. 2003

40. Xie, C.G., Huang, S.M., Hoyle, B.S. and Thorn, R., *Electrical capacitance tomography for flow imaging: system model for development of image reconstruction algorithms and design of primary sensors*, IEE Proc. G, 139(1), 1992, pp 89-98.

41. Feuillet, V., Ibos, L., Fois, M., Dumoulin, J. and Candau, Y., *Defect detection and characterization in composite materials using square pulse thermography coupled with singular value decomposition analysis and thermal quadrupole modelling,* NDT and E International, 51, 2012, pp 58-67

42. Yang, W.Q., Spink, D.M., York, T.A. and McCann, H., *An image-reconstruction algorithm based on Landweber's iteration method for electrical-capacitance tomography*, Meas. Sci. Technol., 10(11), 1999, pp 1065-1999.

43. Yang, W.Q., Stott A.L., Beck, M.S., Xie, C.G., *Development of Capacitance Tomographic Imaging Systems for Oil Pipeline measurements*, Rev. Sci. Instrum., 66(8), 1995, pp 4326-4332.

44. Banasiak, R., Ye, Z. and Soleimani, M., *Improving three-dimensional electrical capacitance tomography imaging using approximation error model theory*, Journal of Electromagnetic Waves and Applications, 26, 2012, pp 411-421

45. Hayes, R., Podd F., Newill P., Grieve B.D. and York T.A., *Capacitively-coupled impedance measurements for ERT*, In: 6th International Symposium on Process Tomography, Cape Town, South Africa, 26-28 March 2012.

46. Soleimani, M., Wang, H.G., Li, Y. and Yang, W.Q., *A comparative study of 3d electrical capacitance tomography,* International Journal of Information Systems Sciences, 3, 2007, pp 292–306.

47. Cao, Z., Xu, L. and Wang, H.X., *Image reconstruction technique of electrical capacitance tomography for low-contrast dielectrics using Calderon's method*, Meas. Sci. Technol., 20, 2009, pp 104027

48. Rabbani, K.S., Kabir, A.M.B.H., *Studies on the effect of the third dimension on a two-dimensional electrical impedance tomography system*, Clinical Physics and Physiol. Meas., 12(4), 1991, pp 393-402.

49. Jang, J.D., Lee, S.H., Kim, K.Y. and Choi, B.Y., *Modified iterative Landweber method in electrical capacitance tomography*, Meas. Sci. Technol., 17(7), 2006, pp 1909-1917

50. York, T., *Status of electrical tomography in industrial applications*, J. Electron. Imaging, 10(3), 2001, pp 609-619

51. Schlicker, D., Washabaugh, A., Shay, I. and Goldfine, N., *Inductive and capacitive array imaging of buried objects*, Insight, 48(5), 2006, pp 302-306

52. Li, Y. and Yang, W.Q., *Measurement of multi-phase distribution using an integrated dual-modality sensor*, IEEE International Workshop on Imaging Systems and Techniques, Shenzhen, China, 11-12 May 2009

53. Li, Y., Yang, W.Q., Xie, C., Huang, S., Wu, Z., Tsamakis, D. and Lenn, C., *Gas/oil/water flow measurement by electrical capacitance tomography*, Meas. Sci. Technol., 24(7), 2013, pp 074001

54. Schoberl, J., *NETGEN: An advancing front 2D/3D-mesh generator based on abstract rules*, Computing and Visualization in Science, 1, 1997, pp 41–52.

55. Adler, A., Arnold, J.H., Bayford, R., Borsic, A., Brown, B., Dixon, P., Faes, T.J.C., Frerichs, I., Gagnon, H., Gärber, Y., Grychtol, B., Hahn, G., Lionheart, W.R.B., Malik, A., Patterson, R.P., Stocks, J., Tizzard, A., Weiler, N. and Wolf, G.K, *GREIT: A unified approach to 2D linear EIT reconstruction of lung images*, Physiol. Meas., 30(6), 2009, pp S35–S55.

56. Murphy, S.C., Stanley, S.J., Rhodes, D. and York, T.A., *3D electrical tomographic imaging using vertical arrays of electrodes*, Meas. Sci. Technol., 17(11), 2006, pp 3053–3065.

57. Wang, F., Marashdeh, Q., Fan, L. and Warsito, W., *Electrical Capacitance Volume Tomography: Design and Applications*, Sensors, 10(3), 2010, pp 1890-1917.

58. Hu, X.H. and Yang, W.Q., *Planar capacitive sensor: designs and applications*, Sensor Review, 30(1), 2010, pp 24-39.

59. Chen, D.X., Hu, X.H. and Yang, W.Q., *Design of a security screening system with a planar single-electrode capacitance sensor matrix*, Meas. Sci. Technol., 22(11), 2011, pp 114026.

60. Diamond, G.G., Hutchins, D.A., Gan, T.H., Purnell, P. and Leong, K.K., *Single-sided capacitive imaging for NDT*, Insight, 48(12), 2006, pp 724-730.

61. Yin, X. and Hutchins, D.A., *Non-destructive evaluation of composite materials using a capacitive imaging technique*, Composites Part B-Engineering, 43(3), 2012, pp 1282-1292

62. Gebrial, W., Prance, R.J., Harland, C.J. and Clark, T.D., N*on-Invasive Imaging Using an Array of Electric Potential Sensors,* Rev. Sci. Instrum., 77, 2006, pp 063708

63. Xu, P., *Truncated SVD methods for discrete linear ill-posed problems*, Geophysics Journal International, 135(2), 1998, pp 505-514.

64. Sun, J. and Yang, W.Q., *3D effect of Electrical Capacitance and Resistance Tomography Sensors*, in Imaging Systems and Techniques, 2012 IEEE International Conference, Manchester, England, 16-17 July 2012.

65. Ye, J.M., Wang, H. and Yang, W.Q., *Characterization of electrical capacitance tomography sensors with different diameter*, IEEE Sensors J., 14(7), 2014, pp 2240-2251

66. Jeanmeure, L.F.C., Zimmerman, W.B. and Clark, W., *Direct flow-pattern identification using electrical capacitance tomography*, Experimental Thermal and Fluid Science, 26, 2002, pp 763-773.

67. Elfving, T., Nikazad, T. and Hansen, P.C., *Semi-convergence and relaxation parameters for a class of SIRT algorithms*, ETNA, 37, 2010, pp 321-336

68. Nissinen, A., Heikkinen, L.M. and Kaipio, J.P., *The Bayesian approximation error approach for electrical impedance tomography-experimental results*, Meas. Sci. Technol., 19(1), 2008, pp 015501.

69. Kaipio, J.P. and Somersalo, E., *Statistical and computational inverse problems*, in *Applied Mathematical Sciences,* 2005, Springer Science and Business Media, Inc.: New York, NY.

70. Dehghani, H. and Soleimani, M. *Numerical modelling errors in electrical impedance tomography*, Physiol. Meas., 28, 2007, pp S45-S55.

71. Marashdeh, Q, Warsito, W, Fan, L.S. and Teixeira, F.L., *A multimodal tomography system based on ECT sensors*, IEEE Sensors J., 7, 2007, pp 426-433

72. Soleimani, M., Mitchell, C.N., Banasiak, R., Wajman, R. and Adler, A., *Four-dimensional electrical capacitance tomography imaging using experimental data,* Progress In Electromagnetics Research, 90, 2009, pp 171-186.

73. Catapano, I., Soldovieri, F. and Crocco, L., *On the feasibility of the linear sampling method for 3D GPR surveys,* Progress In Electromagnetics Research, 118, 2011, pp 185-203.

74. Flores-Tapia, D., O'Halloran, M. and Pistorius, S, *A bimodal reconstruction method for breast cancer imaging*, Progress In Electromagnetics Research, 118, 2011, pp 461-486.

75. Asimakis, N. P., Karanasiou, I. S. and Uzunoglu, N. K., *Non-Invasive Microwave Radiometric System for Intracranial Applications: A Study Using the Conformal L-Notch Microstrip Patch Antenn,* Progress in Electromagnetics Research, 117, 2011, pp 83-101.

76. Litman, A., Geffrin, J.M. and Tortel, H., *On the calibration of a multistate scattering matrix measured by a fixed circular array of antennas*, Progress In Electromagnetics Research, 110, 2010, pp 1-21.

77. Parise, M., *Fast computation of the forward solution in controlled-source electromagnetic sounding problems*, Progress In Electromagnetics Research, 111, 2011, pp 119-139.

78. Wei, H.Y. and Soleimani, M., *Three-dimensional magnetic induction tomography imaging using a matrix free Krylov subspace inversion algorithm*, Progress In Electromagnetics Research, 122, 2012, pp 29-45.

79. Ren, S., Xu, Y., Tan, C. and Dong, F., *Reconstructing the geometric configuration of three dimensional interface using electrical capacitance tomography*, International Journal for Numerical Methods in Engineering, 96, 2013, pp 628–644

80. Li, Y. and, Holland, D., *Fast and robust 3D electrical capacitance* tomography, Meas. Sci. Technol., 24(10), 2013, pp 105406.

81. Ye, Z., Banasiak, R. and Soleimani, M., *Planar array 3D electrical capacitance tomography*, Insight, 55(12), 2013, pp 675-680

82. Ren, S., Dong, F., Xu, Y. and Tan, C., *Reconstruction of the three dimensional inclusion shapes using electrical capacitance tomography*, Meas. Sci. Technol., 25(2), 2014, pp 025403.

83. Dong, X.Y., Ye, Z.Y., and Soleimani, M., *Image reconstruction for electrical capacitance tomography by using soft-thresholding iterative method with adaptive regulation parameter,* Meas. Sci. Technol., 24 (8), 2013, pp 085402

84. Yang, C.L., Wei, H.Y., Adler, A. and Soleimani, M., *Reducing computational costs in large scale 3D EIT by using sparse Jacobian matrix with block-wise CGLS reconstruction*, Physiol. Meas., 34 (6), 2013, pp 645-658.

85. Zhang, M., Ma, L. and Soleimani, M., *Magnetic induction tomography guided electrical capacitance tomography imaging with grounded conductors*, Measurement, 2014, 53, pp 171-181.

86. Ye, J., Wang, H. and Yang, W.Q., *Evaluation of effect of number of electrodes in ERT sensors on image quality*, IEEE International Conference on Imaging Systems and Techniques, Beijin, China, 22-23 Oct. 2013

87. Stewart, V., Soleimani, M. and Budd, C., *Crack detection in dielectric objects using electrical capacitance tomography*, 6th World Congress in Industrial Process Tomography, Beijing, China, 6-9 Sept. 2010

88. Evangelidis, M., Ma, L. and Soleimani, M., *High definition electrical capacitance tomography for pipeline inspection*, Progress In Electromagnetics Research, 141, 2013, pp 1-15

89. Cui, Z.Q., Wang, H.X., Xu, Y.B. and Zhang, L.F., *An integrated ECT/ERT dual modality sensor*, IEEE Instrumentation and Measurement Technology Conference, Singapore, 5-7 May 2009

90. Dyakowski, T., Jeanmeure, L.F.C. and Jaworski, A.J., *Applications of electrical tomography for gas–solids and liquid–solids flows-A review*, Powder Technol., 112, 2000, pp 174-192

91. Wen, J., Xia, Z. and Choy, F., *Damage detection of carbon fiber reinforced polymer composites via electrical resistance measurement*, Composites Part B, 42(1), 2011, pp 77-86

92. Dickin, F.J., Hoyle, B.S., Hunt, A., Huang, S.M., Ilyas, O., Lenn, C., Waterfall, R.C., Williams, R.A., Xie, C.G. and Beck, M.S., *Tomographic imaging of industrial process equipment: techniques and applications*, IEE Proc.-G Circuits, Devices and Systems, 139(1), 1992, pp 72-82

93. Rao, S.M., Zhu, K., Wang, C. and Sundaresan, S., *Electrical capacitance tomography measurements on the pneumatic conveying of solids,* Industrial & Engineering Chemistry Research, 40(20), 2001, pp 4216-4226.

94. Fan, L.S., Warsito, W., and Du, B., *Electrical capacitance tomography imaging of gas-solid and gas-liquid-solid fluidized bed systems,* Journal of Visualization, 7(1), 2004, pp 5-5.

95. Liu, S., Chen, Q., Xiong, X., Zhang, Z. and Lei, J. *Preliminary study on ECT imaging of flames in porous media,* Meas. Sci. Technol., 19(9), 2008, pp 094017

96. Schickert, M., *Ultrasonic NDE of concrete*, IEEE Ultrasonic Symposium Proceeding, 1, 2002, pp 739-748

97. Rose, J.L., Li, J., Zhao, X. and Quarry, M.J. *Ultrasonic guided wave flexural mode tuning for limited access pipe inspection,* Review of Progress in Quantitative Non-destructive Evaluation, 20, 2001, pp 164-171.

98. Maldague, X., *Theory and practice of infrared technology for non-destructive testing,* Wiley series in Microwave and Optical Engineering, 2001.

99. Bai, W. and Wong, B.S., *Evaluation of defects in composite plates under convective environments using lock-in thermography,* Meas. Sci. Technol., 12(2), 2001, pp 142-150

100. Ishikawa, M., Hatta, H., Habuka, Y., Fukui, R. and Utsunomiya, S., *Detecting deeper defects using pulse phase thermography*, Infrared Physics and Technology, 57, 2013, pp 42-49

101. Omar, M., Hassan, M., Donohue, K., Saito, K. and Alloo, R., *Infrared thermography for inspecting the adhesion integrity of plastic welded joints*, NDT and E International, 39(1), 2006, pp 1-7

102. Chen, D., Deng, X. and Yang, W.Q. *Comparison of three electrical capacitance tomography systems*, IEEE International. Conference on Imaging Systems and Techniques, Thessaloniki, 1-2 July 2010

103. Banasiak, R., Wajman, R., Betiuk, J. and Soleimani, M., *Feasibility study of dielectric permittivity inspection using a 3D capacitance CT method,* NDT and E International, 42(4), 2009, pp 316-322

104. Ravenscroft, C.D.F., Hill, R. and Buttle, D., *CHIME: A New Ultrasonic Method for Rapid Screening of Pipe Plate and Inaccessible Geometries,* in 7th *ECNDT-7*th *European Conference on Non-destructive Testing, Copenhagen, 26-29 May 1998*

105. Mahmound, A.M., Ngan, P., Crout, R. and Mukdadi, O.M., *High resolution 3D ultrasound jawbone surface imaging for diagnosis of periodontal bony defects: an in vitro study*, Annals of Biomedical Engineering, 38(11), 2010, pp 3409-3422

106. Munns, I.J. and Georgiou, G.A., *Ultrasonic and radiographic NDT of butt fusion welded polyethylene pipes,* NDT.net, 1999,
[Cited 03 Feb. 2015], Available from: http://www.ndt.net/article/twi/twi.htm

107. Bull, D.J., Helfen, L., Sinclair, I., Spearing, S.M. and Baumbach, T., *A comparison of multi-scale 3D X-ray tomographic inspection techniques for assessing carbon fibre composite impact damage*, Composites Science and Technology, 75, 2013, pp 55-61

108. Feldkamp, J.M., Schroer, C.G., Patommel, J., Lengeler, B., Gunzler, T. F., Schweitzer, M., Stenze, C., Dieckmann, M. and Schroeder, W.H., *Compact X-ray microtomography system for element mapping and absorption imaging*, Rev. Sci. Instrum., 78(7), 2007, pp 073702.

109. Gan, T.H., Hutchins, D.A., Billson, D.R. and Schindel, D.W., *The use of broadband acoustic transducers and pulse-compression techniques for air-coupled ultrasonic imaging,* Ultrasonics, 39(3), 2001, pp 181-194

110. Yunus, M.A.M. and Mukhopadhyay, S.C., *Development of planar electromagnetic sensors for measurement and monitoring of environmental parameters,* Meas. Sci. Technol., 22(2), 2011, pp 025017

111. De Goeje, M.P. and Wapenaar, K.E.D., *Non-destructive inspection of carbon fibre-reinforced plastics using eddy current methods,* Composites, 23(3), 1992, pp 147-157

112. Yang, W.Q., *Design of electrical capacitance tomography sensors,* Meas. Sci. Technol., 21, 2010, pp 042001

113. Cui, Z, Wang, H., Chen, Z. and Yang, W.Q., *Image reconstruction for field-focusing capacitance imaging,* Meas. Sci. Technol., 22(3), 2011, pp 035501

114. Soleimani, M., *Numerical modeling and analysis of the forward and inverse problems in electrical capacitance tomography,* Int. J. Inf. Syst. Sci., 1(1), 2005, pp 193-207

115. Bonse, M.H.W., Mul, C. and Spronck, J.W., *Finite-Element Modeling as a Tool for Designing Capacitive Position Sensors,* Sensors and Actuators A: Physical, 46(1), 1995, pp 266-269

116. Soleimani, M., Stewart, V.J., and Budd, C.J., *Crack detection in dielectric objects using electrical capacitance tomography imaging,* Insight, 53(1), 2011, pp 21-24

117. Almashary, B., Qasim, S., Alshebeili, S. and Al-Masry, W., *Realization of linear back-peojection algorithm for capacitance tomography using FPGA,* 4th World Congress Industrial Process Tomography, Aizu, Japan, 2-5 Sept. 2005

118. Peng, L.H., Merkus, H., and Scarlett, B., *Using regularisation methods for image reconstruction of electrical capacitance tomography,* Particle and Particle Systems Characterization, 17(3), 2000, pp 96-104

119. Yang, W.Q., *Tomographic Imaging based on capacitance measurement and industrial applications,* IEEE International Workshop on Imaging Systems and Techniques, Krakow, Poland, 5 May 2007

120. Huang, S., Xie, C., Thorn, R., Snowden, D. and Beck, M., *Design of sensor electronics for electrical capacitance tomography*, IEE Proc.-G Circuits Devices and Systems, 139(1), 1992, pp 83-88

121. Chen, T.M. and Bowler, N., *Analysis of a capacitive sensor for the evaluation of circular cylinders with a conductive core,* Meas. Sci. Technol., 23(4), 2012, pp 045102

122. Shi, T.M., Xie, C.G., Huang, S.M., Williams, R.A. and Beck, M.S., *Capacitance-based instrumentation for multi-interface level measurement,* Meas. Sci. Technol., 2(10), 1991, pp 923-933

123. Shull, P.J., Clark, A.V., Heyliger, P.R., Moulder, J.C. and Auld, B.A., *Characterization of capacitive array for NDE applications,* Research in Non-Destructive Evaluation, 2(1), 1990, pp 11-27

124. Yin, X., Chen, G., Li, W. and Hunthchins, D.A., *Design and characterization of planar capacitive imaging probe based on the measurement sensitivity distribution*, In AIP Conf. Proc., Denver, Colorado, USA, 15-20 July 2012.

125. Nassr, A.A., Ahmed, W.H., and El-Dakhakhni, W.W., *Coplanar capacitance sensors for detecting water intrusion in composite structures,* Meas. Sci. Technol., 19(7), 2008, pp 075702

126. Tan K.T., Watanabe N. and Iwahori Y., *X-ray radiography and micro-computed tomography examination of damage characteristics in stitched composites subjected to impact loading*, Composites Part B: Engineering, 42(4), 2011, pp 874-884

127. Kaipio, J. and Somersalo, E., *Statistical inverse problems: Discretization, model reduction and inverse crimes*, Journal of Computational and Applied Mathematics, 198, 2007, pp 493-504

128. Soleimani, M., Vauhkonen, M., Yang, W.Q., Peyton, A., Kim, B.S. and Ma, X., *Dynamic imaging in electrical capacitance tomography and electromagnetic induction tomography using a Kalman filte*r, Meas. Sci. Technol., 18, 2007, pp 3287-3294

129. Heikkinen, L.M., Vauhkonen, M., Savolainen, T. and Kaipio, J.P., *Modelling of internal structures and electrodes in electrical process tomography*, Meas. Sci. Technol., 12(8), 2001, pp 1012-1019

130. Li, Y. and Soleimani, M., *Imaging conductive materials with high frequency electrical capacitance tomography*, Measurement, 46(9), 2013, pp 3355-3361

131. Zhang, M., Ma, L., Ye, Z., Yang, C.L., Wei, H.Y., Banasiak, R. and Soleimani, M.*, Near subsurface 3D imaging using planar array: EIT, ECT, MIT,* 7th World Congress in Industrial Process Tomography, *Krakow*, Poland, 2-5 *Se*p 2013

132. Peng, L., Ye, J., Lu, G. and Yang, W.Q., *Evaluation of effect of number of electrodes in electrical capacitance tomography sensors on image quality*, IEEE Sensors J., 14, 2011, pp 1554-1565

133. Gamio, J.C., *A comparative analysis of single- and multiple-electrode excitation methods in electrical capacitance tomography,* Meas. Sci. Technol., 13, 2002, pp 1799-1809

134. Qiu, C., Hoyle, B.S. and Podd, F.J.W., *Engineering and application of a dual-modality process tomography system*, Flow Meas. Instrum., 18, 2007, pp 247-254

135. Saarenketo, T., *Electrical properties of water in clay and salty soils*, J. Appl. Grophys., 40, 1998, pp 73-88

136. Banasiak, R. and Soleimani, M., *Shape based reconstruction of experimental data in 3D electrical capacitance tomography,* NDT and E International, 43(3), 2010, pp 241-249

137. Wu. D. and Busse, G., *NDT of materials using lock-in thermography,* NDT.net, 1997, [Cited 03 Feb. 2015], Available from: http://www.ndt.net/article/dresd97/wu/wu.htm

138. Ng, H.F., *Automatic thresholding for defect detection,* Pattern Recognition Letters, 27(14), 2006, pp 1644-1649

139. Yang, W.Q., Stott, A.L., and Beck, M.S., *High-Frequency and High-Resolution Capacitance Measuring Circuit for Process Tomography,* IEE Proc.-Circuits Devices and Systems, 141(3), 1994, pp 215-219

140. Gao, Y.L. and Zhang, Y.G., *Key Issues in Designing High-speed Hardware for Electrical Capacitance Tomography System,* Computer Science Technology and Applications, 1, 2009, pp 332-335

141. Gao, Y.L., Xu, Q., and Zhou, F., *Research on factors of influencing ECT image reconstruction,* 2nd IEEE Conference on Industrial Electronics and Applications, Harbin, China, 23-25 May 2007, 1, pp 1627-1630

142. Huang, Z.Y., Wang, B.L., and Li, H.Q., *Application of electrical capacitance tomography to the void fraction measurement of two-phase flow,* IEEE Trans. on Inst. and Meas., 52(1), 2003, pp 7-12

143. Cao, Z., Xu, L., Fan, W. and Wang, H., *Electrical capacitance tomography for sensors of square cross sections using Calderon's method,* IEEE Trans. on Inst. and Meas., 60(3), 2011, pp 900-907

144. Chen, T. and Bowler, N., *Analysis of a concentric coplanar capacitive sensor for non-destructive evaluation of multi-layered dielectric structures,* IEEE Trans. on Dielectr. Elect. Insul., 17(4), 2010, pp 1307-1318

145. Kriesz, H., *Radiographic NDT-a review,* NDT International, 12, 1979, pp 270-273.

146. Wei, H.Y. and Soleimani, M., *Theoretical and Experimental Evaluation of Rotational Magnetic Induction Tomography,* IEEE Trans. on Inst. and Meas., 61(12), 2012, pp 3324-3331

147. Kabanikhin, S.I., *Definitions and examples of inverse and ill-posed problems*, J. Inv. Ill-Posed Problems, 16, 2008, pp 317-357